The Pilot-Wave Dynamics of Walking Droplets in Confinement

by

Daniel Martin Harris

Submitted to the Department of Mathematics
in partial fulfillment of the requirements for the degree of

Doctor of Philosophy

at the

MASSACHUSETTS INSTITUTE OF TECHNOLOGY

June 2015

Signature redacted

Author .....
Department of Mathematics
May 1, 2015

Signature redacted

Certified by .....
John W. M. Bush
Professor of Applied Mathematics
Thesis Supervisor

Signature redacted

Accepted by .....
Peter Shor
Chairman, Department Committee on Graduate Theses

The Pilot-Wave Dynamics of Walking Droplets in Confinement

by

Daniel Martin Harris

Submitted to the Department of Mathematics
on May 1, 2015, in partial fulfillment of the
requirements for the degree of
Doctor of Philosophy

Abstract

A decade ago, Yves Couder and coworkers discovered that millimetric droplets can walk on a vibrated fluid bath, and that these walking droplets or "walkers" display several features reminiscent of quantum particles. We first describe our experimental advances, that have allowed for a quantitative characterization of the system behavior, and guided the development of our accompanying theoretical models. We then detail our explorations of this rich dynamical system in several settings where the walker is confined, either by boundaries or an external force. Three particular cases are examined: a walker in a corral geometry, a walker in a rotating frame, and a walker passing through an aperture in a submerged barrier. In each setting, as the vibrational forcing is increased, progressively more complex trajectories arise. The manner in which multimodal statistics may emerge from the walker's chaotic dynamics is elucidated.

Thesis Supervisor: John W. M. Bush
Title: Professor of Applied Mathematics

Acknowledgments

I would like to thank John Bush for introducing me to the stimulating problem that serves as the subject of my thesis. This work would not have been possible without his guidance and enthusiasm. I am incredibly grateful for all of his advice and support during my PhD, on matters both academic and beyond.

I'd also like to thank Anand Oza, both as a colleague and a friend. The experiment and theory benefitted immensely from our fruitful collaboration. Thanks also goes to Giuseppe Pucci for his assistance with the diffraction experiments and to Lucas Tambasco for his help with the droplet generator, and to both of them for their friendship. I'd also like to acknowledge Yves Couder, whose imagination inspired this exciting field of research, for his encouragement. I also thank Ruben Rosales for many engaging discussions.

I thank Jessica Popescu for her unwavering love and support. Without her encouragement, I would not have been able to complete the program. I also thank my parents and family for their love and encouragement.

I would finally like to acknowledge the National Science Foundation for financial support throughout much of my PhD.

Contents

List of Figures

List of Tables

Chapter 1

Introduction

In an article on the relationship of statistics, probability, and chaos [6], Mark Berliner poses an insightful challenge to the reader:

> *"...can you come up with a physical model or a real statistics problem that results in randomness that does not stem from some deterministic uncertainty?"*

However, he then adds a single exemption:

> *"The only 'rule' in this mind game is that you cannot resort to quantum mechanics."*

Probability and statistics are powerful tools used in nearly all scientific fields to describe the outcomes of complex processes that result in some distribution of outcomes. For example, in fluid mechanics, statistics readily describe the size of droplets formed from the breakup of a fluid jet [103] or the scale of vortices in a turbulent flow [99], while the outcomes of individual events remain unpredictable. The need to describe the outcome of a deterministic physical process probabilistically is typically rooted in the sensitivity of the underlying dynamical process to initial conditions and external disturbances that are beyond what can be measured or controlled. In this thesis, we explore a macroscopic wave-particle system, and demonstrate that a form of pilot-wave dynamics can lead to unpredictable behavior, from which a coherent multimodal

statistical pattern may emerge. Could a complex dynamics, yet to be resolved, similarly underlie the successful statistical description provided by quantum mechanics? Although this work does not seek to address this question directly, our hope is that it will open the mind of the reader to the possibility that quantum mechanics may not be an exception after all.

When a liquid bath of density ρ, viscosity ν, surface tension σ, and depth H undergoes vertical vibration with acceleration $a(t) = \gamma\cos(2\pi ft)$, its free surface becomes unstable to a standing field of Faraday waves [50] above a critical acceleration amplitude, $\gamma > \gamma_F$, corresponding to the Faraday threshold (figure 1-1(a)). The linear stability of the free surface was first analyzed by Benjamin & Ursell, who demonstrated that the wave amplitude was governed by a Mathieu equation [5]. The most unstable Faraday wave mode is typically subharmonic, with the free surface oscillating once every two driving periods with a wavelength (λ_F) determined by the standard water wave dispersion relation [74]. For low viscosity fluids and large aspect ratio containers, the unstable free surface tends to arrange into a square pattern comprised of two perpendicular standing waves [80, 73]. For smaller containers, the boundaries determine the final form of the wave pattern [41, 65]. More extensive details on the Faraday instability can be found in the review by Miles & Henderson [79].

When a drop of diameter D is gently deposited onto a fluid bath, it will reside there until the intervening air layer has had time to drain to a critical thickness at which van der Waals forces initiate either complete or partial coalescence [71]. However, coalescence can be avoided if the fluid bath is vibrated vertically [104, 24, 57] so that the drop rebounds from the surface before the onset of coalescence (figure 1-1(b)). Multiple droplets bouncing on the surface of the bath may interact through their wave fields, forming stable lattice arrangements [43, 42] (figure 2-19). Pairs of droplets of unequal size may move spontaneously across the surface due to the asymmetry of the wave field generated [47].

The vertical dynamics of these bouncing droplets is highly sensitive to their radius, the driving frequency and amplitude, as well as the fluid parameters [24, 91, 57, 81,

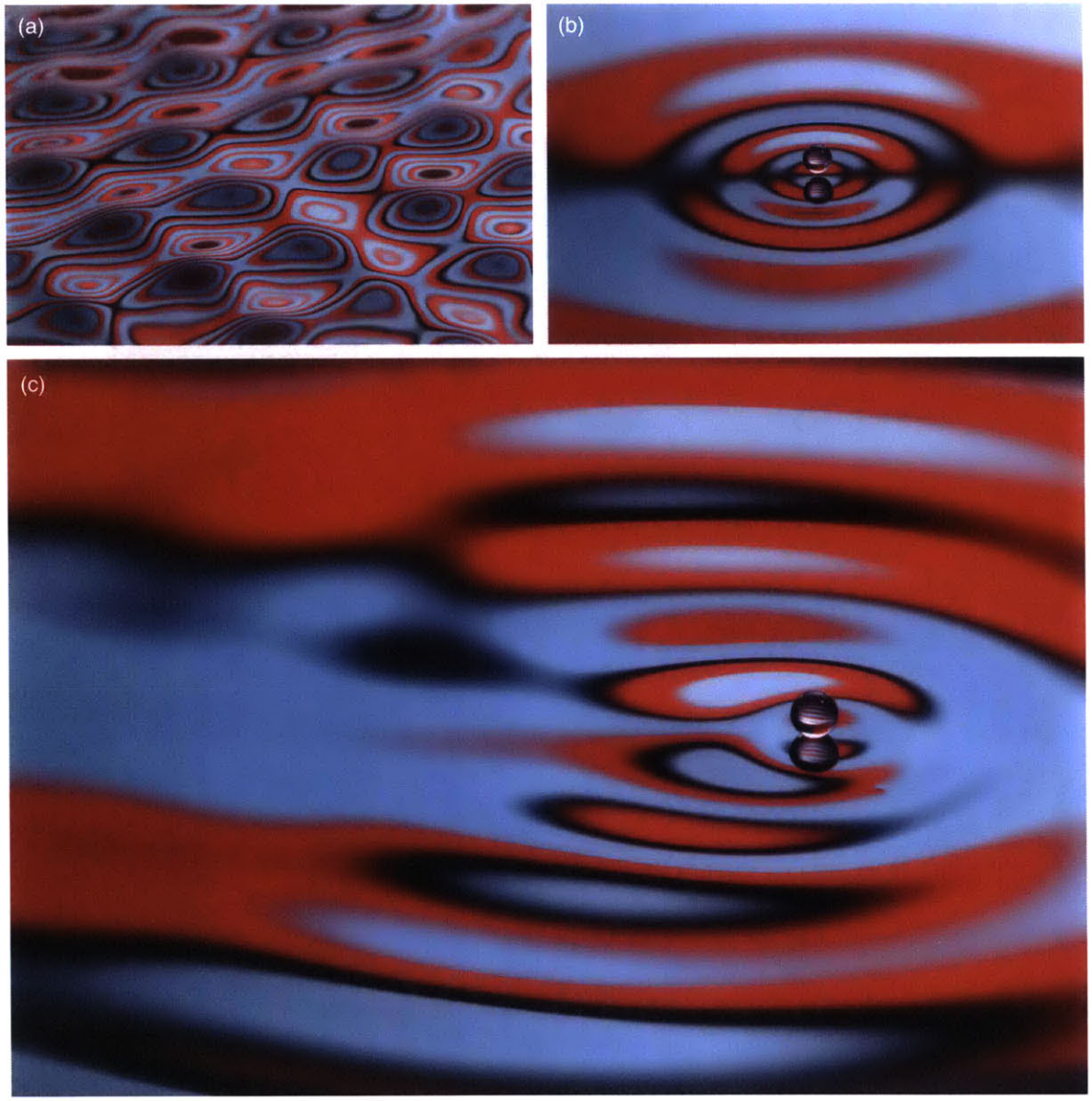

Figure 1-1: (a) Faraday waves form on the free surface when the acceleration amplitude exceeds a critical threshold. (b) Below this threshold, a droplet bounces periodically on the surface of a vibrated fluid bath. (c) As the forcing amplitude is increased towards the Faraday threshold, the droplet begins to walk across the surface due to the interaction with its wave field.

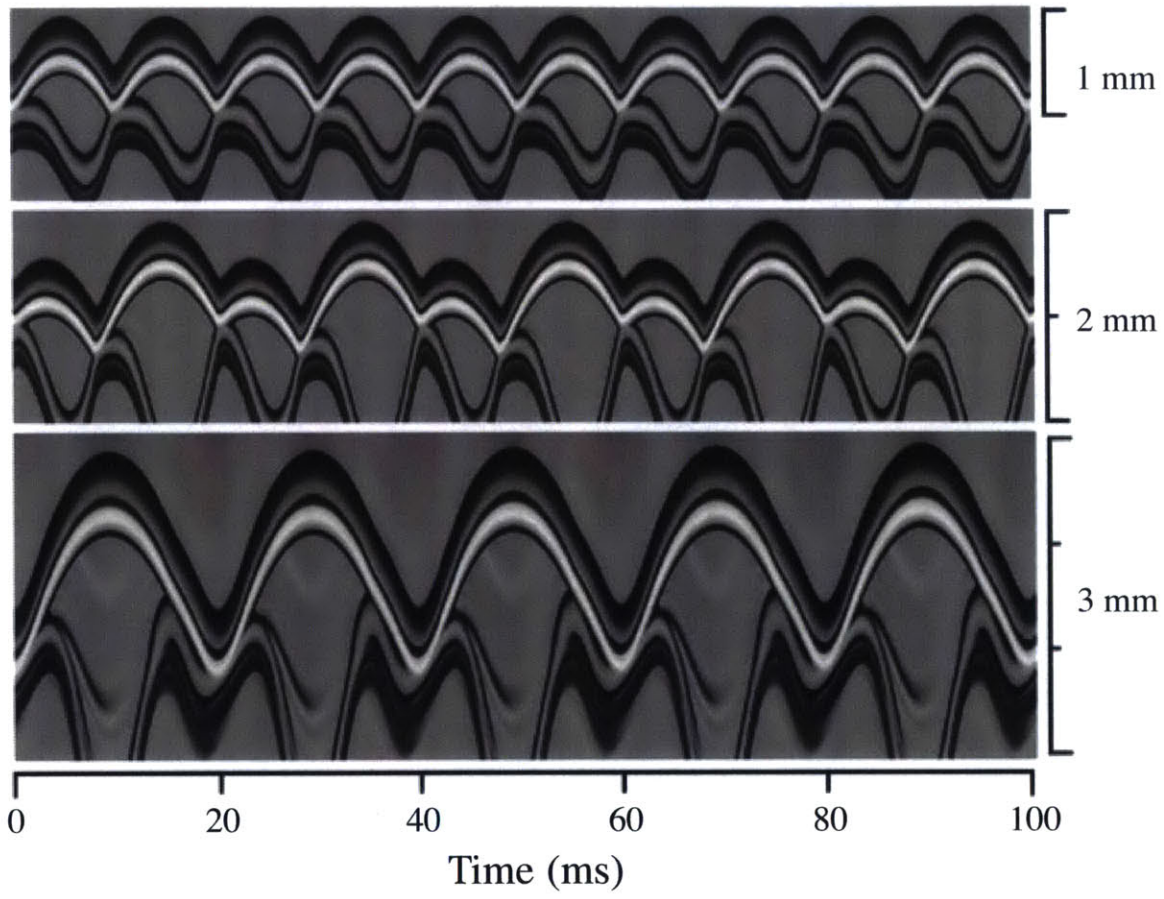

Figure 1-2: Spatiotemporal diagrams of the vertical motion of a droplet bouncing on a vibrating fluid bath. Images represent superpositions of a single-pixel slice through the center of the droplet. As the forcing acceleration is increased (from top to bottom), the drop undergoes a period doubling event whereby it transitions from impacting the bath once every vibration cycle to once every two vibration cycles. Its bouncing is then synchronized with its Faraday wave field. Figure adapted from [81].

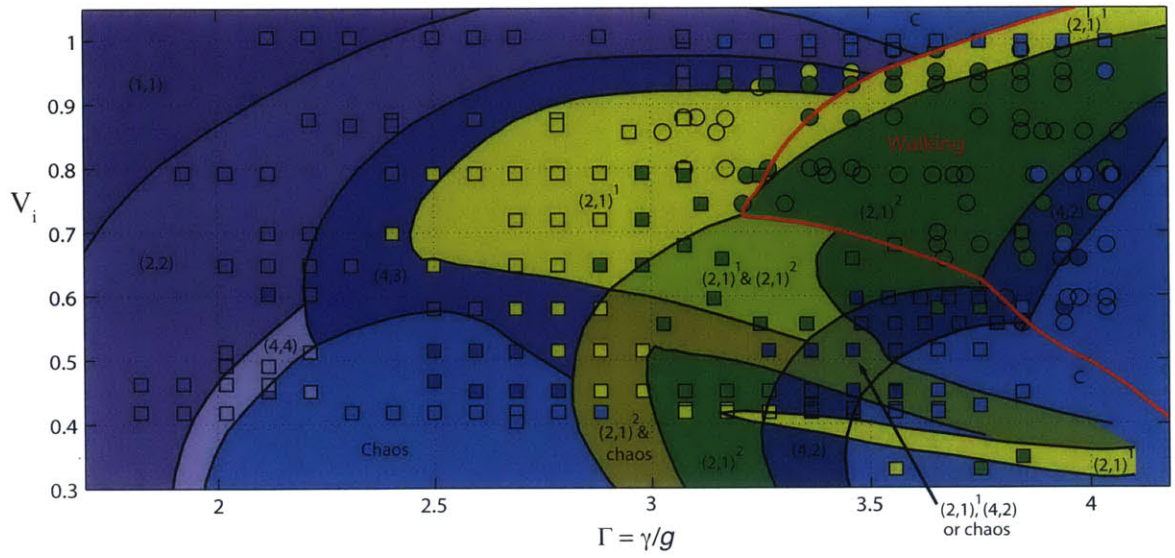

Figure 1-3: Vertical dynamics as a function of the forcing amplitude γ/g and the vibration number $V_i = 2\pi f\sqrt{\rho D^3/8\sigma}$ for a forcing frequency of f = 80 Hz and oil viscosity ν = 20 cSt. Regions are labeled by (m, n), as indicates the different predicted bouncing dynamics. In the (m, n) mode, the drop bounces n times in m driving periods. The shaded regions correspond to the theoretical predictions, with the red line denoting the predicted walking threshold. The markers represent experimental data, colored according to the observed bouncing mode. The square markers represent stationary bouncing states whereas the round marker represent walking states. Figure adapted from [105].

105]. As the vibration amplitude is increased, the droplet may undergo a period-doubling transition in its vertical dynamics (figure 1-2), similar to that observed for an elastic ball bouncing on vibrated plate [68] or for a droplet bouncing on a vibrated soap film [54, 56]. In the period-doubled regime, the droplet impacts the bath once every two vibration cycles, thus forcing the free surface at the frequency of the most unstable Faraday wave, leading to the excitation of a localized field of damped Faraday waves centered on the droplet. Once this resonance has been achieved, the bouncing state may become unstable to a walking state, in which the droplet is pushed along by the Faraday waves it has generated at prior impacts [25, 91, 82] (figure 1-1(c)). In addition to the simple period-doubled walkers, droplets with more exotic bouncing dynamics, including complex periodic and chaotic vertical motions, have also been shown to walk [105] (figure 1-3).

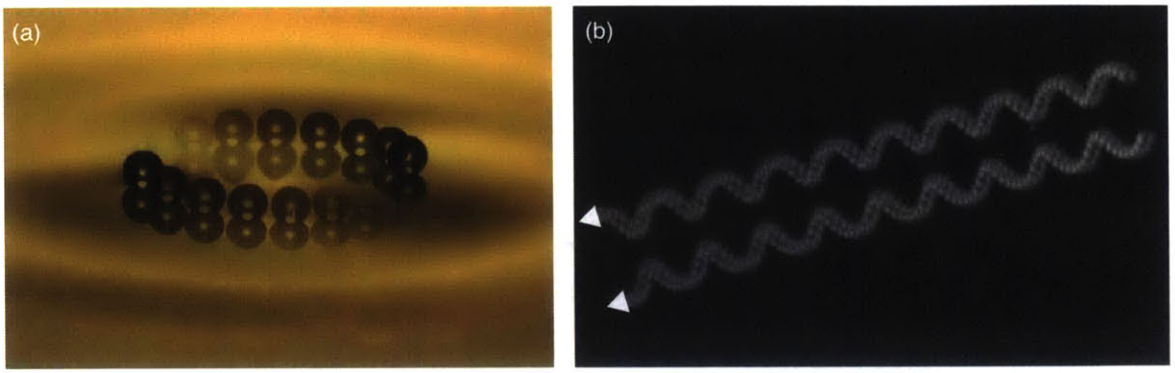

Figure 1-4: (a) Oblique view of a pair of walkers locked in orbit. (b) Top view of a pair of walkers advancing in a "promenade" mode. Images of the droplets taken at the moment of impact are superposed.

In the absence of barriers or external forces, these walking droplets, or "walkers", move along rectilinear trajectories, typically at a constant speed [75, 18]. The walking droplets are stable to perturbations in the direction of motion but neutrally stable to lateral perturbations: their direction of motion can thus be readily altered [85]. A walker is a spatially extended object comprising both droplet and wave. The droplet would not self-propel without the presence of the waves, and the waves would be absent without the presence of the droplet. Pairs of walkers can interact through their shared wave field; as they approach one another, they may scatter, lock into orbit, or walk nearly parallel in a "promenade" mode [91, 45, 14] (figure 1-4). The stable spacings between walkers in bound states are discrete, and depend on the Faraday wavelength.

An important feature of the walking droplet system is path-memory [46]. Since the wave field at any given time is the result of the droplet's previous impacts, the instantaneous force acting on the droplet depends on the positions of these impacts. The wave generated at each impact decays exponentially with a characteristic time scale $T_M = M_e T_F = \frac{T_d}{(1-\gamma/\gamma_F)}$ where T_D is the decay time of the waves in the absence of vibrational forcing, and T_F is the period of the Faraday waves [46, 82]. M_e is the memory parameter and gives an indication of the number of previous impacts that contribute to the walker's wave field. Note that the memory time increases as γ/γ_F increases, and diverges as $\gamma/\gamma_F \to 1$. The non-dimensional vibrational forcing

amplitude γ/γ_F will be our principal control parameter in all of the studies presented.

The walking droplet system is remarkably similar to an early version of quantum dynamics envisaged by Louis de Broglie [31, 32]. He imagined that internal oscillations of quantum particles at the Compton frequency generate a monochromatic wave centered at the particle, which then propels or 'pilots' the particle. It was asserted but not proven that pilot-wave dynamics of this form, a vibrating particle moving in resonance with its guiding wave field, could give rise to trajectories consistent with the statistical predictions of quantum mechanics. While his theory was not satisfactorily completed, the physical picture of an oscillating particle being guided by a self-excited wave field has now been realized by the walking droplet system, but at a macroscopic scale. The relationship between the walker system and de Broglie's mechanics and its modern extensions is discussed in the recent review of Bush [17].

The walking droplets have been shown to exhibit several features reminiscent of quantum particles [16, 17]. The first quantum-analogue experiments performed in this system were those demonstrating single-particle diffraction and interference [22]. In these experiments, individual walkers were directed towards single- and double-slit configurations. After passing through the opening, the trajectory of the walker was diverted due to the distortion of its guiding wave field. They repeated the experiment many times, measuring the deflection angle of each passage, which was independent of its approach to the slit. Preferred deflection angles emerged in the statistical pattern, which was similar in form to the amplitude of a diffracted plane wave with wavelength λ_F impinging on the slit. The statistical results reported have yet to be reproduced, and the effect of memory was not explored. We review and revisit the single-slit experiment in Chapter 5.

A form of tunneling was also demonstrated in this hydrodynamic pilot-wave system. Eddi *et al.* [44] directed a walking droplet towards a shallow region of finite extent and tracked the probability of its crossing this obstacle. While individual crossing events were unpredictable, the crossing probability was observed to decay exponentially with the barrier width, and increase with the walker's speed. Recent investigations on tunneling in this system has revealed new possible trajectories, such

as trapping above the barrier [20].

Orbital quantization was first observed in the walker system when the walker moves on a rotating fluid bath [52]. In the absence of wave effects, one would expect a particle moving at a constant speed on a rotating parabolic dish to execute a circular orbit, whose radius depends continuously on the rotation rate. In the walker system, at low memory, this is indeed the case; however, when the memory is increased, the walker begins to interact with its own wake, and preferred radii emerge. Fort *et al.* [52] noted that the form of the Coriolis force is analogous to the Lorentz force acting on a charged particle in a uniform magnetic field, and thus drew an analogy with Landau levels. The quantization of orbital radius has recently been rationalized in terms of the linear stability of the circular orbits [84]. We revisit the rotating system in Chapter 4. Eddi *et al.* considered pairs of walkers in a rotating bath and showed that their orbital radii can be modulated by the rotation of the bath, with the radii increasing or decreasing according to whether the orbiting pair is co- or counter-rotating relative to the bath [45]. This effect is reminiscent of the Zeeman effect, whereby spectral lines are split in the presence of a magnetic field [108].

An external force can also be applied to a walker by applying a non-uniform magnetic field to a droplet containing a small amount of ferrofluid [90]. Depending on the strength of the field and the walker speed, different periodic or quasiperiodic trajectories were observed, including circular orbits, trefoils, and lemniscates. Both the mean radius and angular momentum of each of the trajectories were observed to take only discrete values, resulting in doubly-quantized orbits. This double quantization was rationalized through considering the influence of the global wave mode excited by each path [76]. At high memory, chaotic switching between trajectories was observed [89].

In this thesis, we explore several settings where a walking droplet is confined by barriers or an external force. We give particular attention to the influence of memory in each configuration, and the transitions arising as the Faraday threshold is approached. The dynamical and statistical behavior of the walkers in each scenario are characterized and discussed. In chapter 2, we review our experimental advances and

refinements, which have allowed for careful control of the experimental parameters, and improved flow visualization. In chapter 3, we confine the walker to circular and rectangular cavites, in order to explore a hydrodynamic analogue of the quantum corral experiments [26]. In chapter 4, we revisit the experiments of a walker in a rotating container first conducted by Fort *et al.* [52], and extend their investigation to higher memory. We also explore the rotating system numerically and characterize the transition from stable circular orbits to chaotic trajectories arising as the memory is increased. Finally in chapter 5, we revisit the single-slit experiment, first explored by Couder & Fort [22]. While different statistical results are recovered, a number of interesting new questions are raised. We conclude in chapter 6 with a discussion of our results, their implications, and potentially fruitful future directions.

Chapter 2

Experimental methods

2.1 Generating uniaxial vibration

Electrodynamic shakers are widely used in experimental investigations of vibrated fluids and granular materials. However, they are plagued by undesirable internal resonances that can significantly impact the quality of vibration. In this section, we measure the performance of a typical shaker and characterize the influence that a payload has on its performance. We present the details of an improved vibration system based on a concept developed by Goldman [58] which consists of a typical electrodynamic shaker with an external linear air bearing to more effectively constrain the vibration to a single axis. The principal components and design criteria for such a system are discussed. Measurements characterizing the performance of the system demonstrate considerable improvement over the unmodified test shaker. In particular, the maximum inhomogeneity of the vertical vibration amplitude is reduced from approximately 10% to 0.1%; moreover, transverse vibrations were effectively eliminated.

The overall design of standard electrodynamic shakers is not dissimilar to that of a loudspeaker [77, 78]. Their primary feature is an armature assembly driven by a coil

This section appears as published in: D. M. Harris and J. W. M. Bush. Generating uniaxial vibration with an electrodynamic shaker and external air bearing. *Journal of Sound and Vibration*, 334:255-269, 2015 [62].

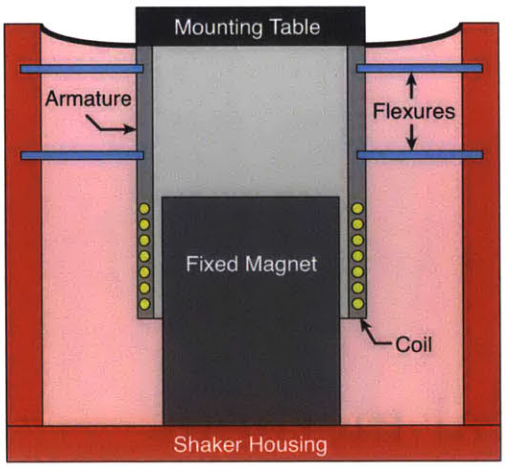

Figure 2-1: Simplified schematic of cross-section of a typical electrodynamic flexure-suspension shaker.

of wire subject to a radial magnetic field. The armature is mechanically supported and positioned within the shaker housing by a flexure plate with low axial stiffness. A schematic of the cross-section of a typical electrodynamic shaker is shown in figure 2-1. While such traditional electrodynamic shakers are relatively robust and can generate a high level of force output, they often introduce undesirable transverse or rocking motions as a result of internal resonances [94]. This non-axial motion is of particular concern for calibrating accelerometers [13]. International standards for accelerometer calibration include guidelines as to the level of acceptable transverse motion [70]. Below 1000 Hz, transverse motion below 10% of the axial vibration amplitude is considered acceptable by these standards, however these limits are readily exceeded by typical flexure-based shakers [13].

One method to minimize transverse motion of the armature is by incorporating an air bearing slide in place of the flexures [38, 40]. This provides a high degree of lateral stiffness while maintaining nearly frictionless motion along axis. Several manufactures have begun to offer air-bearing shakers (e.g. The Modal Shop K394B30/B31), marketed primarily for accelerometer calibration applications. The payload capacity for such devices is generally quite low (less than 0.5 kg), severely limiting their range of utility for other applications. When both higher force capacity and uniaxial motion

are required, other options must be pursued.

One option, the focus of this section, is using a standard electrodynamic shaker with a flexure suspension and an external air bearing. Similar systems have been used in the past, primarily to study the behavior of vibrated granular media [58, 33, 93, 29, 36, 37, 106, 34, 35, 60] and also in studies of vibrated thin plates [15]. The frequencies of interest for these experiments generally range from 10 to 150 Hz. Non-axial vibration can be particularly detrimental to studies of vibrated granular materials, which can result in heaping [102, 87] as well as bulk rotation [58, 3]. The recent work of Aranson *et al.* [3] suggested that observations of large scale swirling motions of quasi-horizontal vibrated granular rods [83] may be due to unintended in-plane vibrations of the substrate. In particular, their experiments with an unmodified shaker and theoretical modeling suggest that the swirling motion is highly sensitive to the relative phase of the horizontal and vertical vibrations, which changes most rapidly near an internal resonant frequency of the shaker. They also noticed a significant shift in the shaker resonant frequency when switching from a monolayer of rice to steel rods, corresponding to an increase of only 0.18 kg in the mass of the payload. This is a striking example of an experiment where ignoring non-axial motions of the driver may lead to spurious conclusions.

Similar vibration systems incorporating an external air bearing have also been used to study Faraday waves [59, 95, 69, 39]. Above a critical value of the forcing amplitude known as the Faraday threshold, waves form spontaneously on the free surface [50, 79]. In studies of Faraday waves, spatial inhomogeneities of the forcing amplitude can lead to the formation of asymmetric surface wave patterns [7]. One option to attempt to compensate for nonuniform vibrational forcing amplitude is to dynamically balance the payload by positioning weights along the periphery of the fluid container until the Faraday waves appear to be uniformly excited at threshold [4]. However, an unbalanced payload could be potentially damaging to the shaker; furthermore, this process is time consuming and heuristic, and must be repeated with any change in the payload or driving. It is also unclear what impact this method has on the transverse motions of the shaker.

In the present experiments, the analogue quantum behavior emerges just below the Faraday threshold where in the absence of the droplet, the surface remains flat. Typical studies of this system use vibration frequencies ranging from 20 to 150 Hz [92], but most commonly in the intermediate range of 50 to 80 Hz. Typical acceleration amplitudes are below $5g$, where g is the acceleration due to gravity. Driver payloads are typically on the order of a few kilograms.

Despite the numerous applications of electrodynamic shaker systems, details about their design and quantification of their performance benefits are extremely rare. Providing these details for our the system is the focus of the present work, which we hope will prove useful to those interested in the experimental modeling of hydrodynamic quantum analogues. In Section 4.1.1, we describe the details of the shaker as well as our measurement techniques. In Section 2.1.2, we present baseline measurements of our unmodified test shaker, which motivates the need for an improved design. In Section 2.1.3, we outline the details of the improved system and specify key design criteria. In Section 2.1.4, we present the test results of the improved system. Finally in Section 2.1.5, we summarize our conclusions and offer perspectives for future applications.

2.1.1 Experimental details

Throughout this work we use a Data Physics V55 electrodynamic shaker and PA300E amplifier as our driver, which is rated for a maximum sine force of 310 N and 12.7 mm peak-to-peak travel. It has a 76.2 mm diameter mounting table atop the armature with 9 threaded mounting holes. This shaker will be identified throughout as our "test shaker." While the construction of our test shaker is typical of most standard shakers with flexure-plate suspensions, the precise characteristics and internal resonances will of course vary between manufacturers and models. Regrettably, data on transverse motion and spatial homogeneity of vibration is not readily available when purchasing a shaker. One specification that is commonly provided in the manufacturer's literature is the armature resonance frequency, which refers to the frequency at which flexural resonances of the metal armature are excited. For our test shaker this frequency

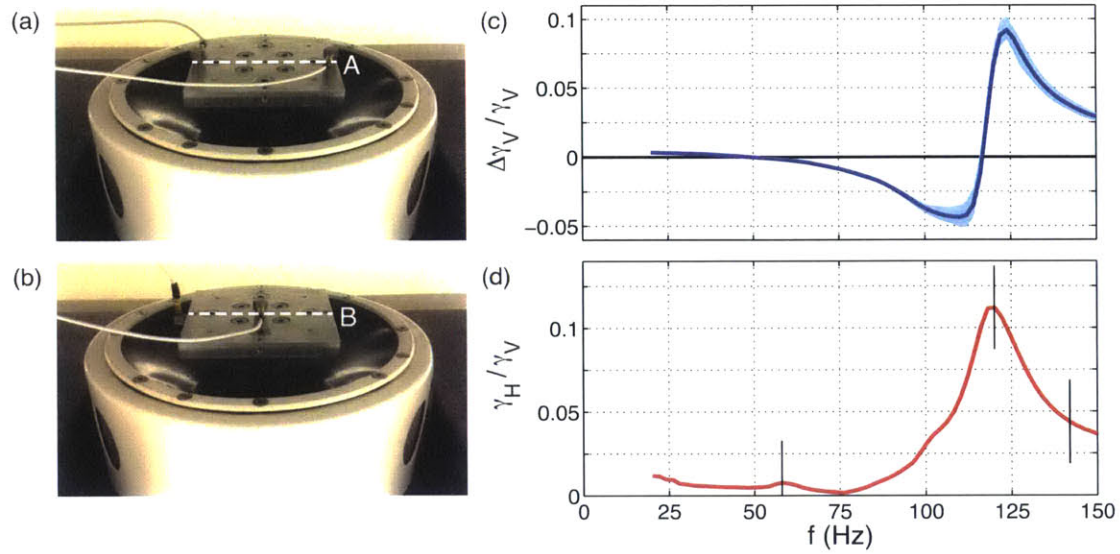

Figure 2-2: Performance of test shaker with payload of $m = 0.23$ kg, as shown in (a) and (b). The dashed lines labeled A and B indicate the horizontal line over which all measurements were taken. (c) Normalized difference in vertical acceleration amplitude measured in two diametrically opposed locations on accelerometer mounting plate as shown in (a). The solid line is the mean of five frequency sweeps, while the the shaded region indicates the complete range of measurements. (d) Acceleration amplitude of horizontal vibration, measured as shown in (b). Characteristic error bars corresponding to the transverse sensitivities are shown.

is listed as 7000 Hz ±5%, well above the typical operational frequencies for studies of granular media, Faraday waves, and bouncing droplets (< 150 Hz). One might thus naturally but mistakenly assume that such a shaker would provide high-quality driving for our experiments.

The shaker housing (43 kg) is bolted directly to a massive steel platform (54 kg) which can be leveled. An additional mass of 110 kg of granite blocks is added to the platform to further attenuate the vibration of the support structure. The leveling legs rest on rubber vibration-damping pads which reduce transmission of vibration to the floor.

In this study we measure accelerations using two miniature piezoelectric accelerometers (PCB, 352C65) weighing 2.0 grams each and with sensitivities of approximately 100 mV/g, where g is the acceleration due to gravity. For measurements of the homogeneity of vertical vibration, we stud mount the two accelerometers on diametrically

opposed positions atop a precision ground aluminum plate, as shown in figure 2-2a. The hole for the stud is drilled and tapped normal to the mounting surface with an error of less than 1°. The mounting surface is cleaned before each installation and coated with a thin film of oil which fills any small voids in the surface, improving the vibration transmission to the sensor. The nominal calibration uncertainty for the sensors is ±1.5% for frequencies in the range of 10-99 Hz and ±1.0% for the frequencies in the range of 100-1999 Hz. The influence of these uncertainties on our assessment of vertical vibration homogeneity can be mitigated via a cross check of the accelerometer measurements. Specifically, we repeat each measurement twice, swapping the positions of the accelerometers on the second trial, and averaging the results. This mitigates any differences introduced exclusively by different calibration errors of the two accelerometers. Some measurement error naturally persists, which we refer to as "random error." Random error can be caused by environmental factors, transverse sensitivities of the accelerometers, and even differences in accelerometer cable routing and mounting torque [70]. We minimize measurement errors introduced by the accelerometer cable by routing the cable so that it does not contact the payload during operation. We also adjust the stationary cable routing point in order to avoid any transverse standing waves that can arise along the cable length. Furthermore, the shaker typically warms over hours of use [106], and the mechanical properties of its suspension may subsequently drift, leading to minor differences in performance between experiments. To assess the relative influence of random errors, we repeated the aforementioned measurement procedure many times for our primary data sets with and without the external air bearing (five times for figure 2-2c and thirteen times for figure 2-8b), each time sweeping the full frequency range of interest and dismounting and remounting both the accelerometers and their mounting plate following each measurement. Well below the shaker resonant frequency, the random errors were typically no greater than ±0.1%.

In addition to measuring the homogeneity of the vertical acceleration, we measure the horizontal (transverse) vibration along the same horizontal line over which we measured the differences in vertical vibration. For these experiments we use the same

two accelerometers, now mounting one at the center of the vibrating platform as reference and the other to the side of the accelerometer mounting platform (normal to the upper face of the platform) with its measurement axis passing through the central axis of the shaker. An example of this measurement setup is show in figure 2-2b. The nominal transverse sensitivity of the accelerometers is ±2.5%, which is consistent with our observed variability in the measured amplitude of horizontal vibration. As a result, measurements of horizontal vibration amplitude are only to be considered significant if they exceed 2.5% of the concurrent vertical vibration amplitude. Similarly, quantitative comparisons between any two measurements of horizontal vibration are not made with any finer resolution.

The horizontal line on the shaker's mounting platform over which we performed all of the measurements in this work was chosen arbitrarily, but the same for all measurements (eg. see figures 2-2a, 2-2b, and 2-12). The results would be very similar had we selected any other line.

We use a National Instruments data acquisition system (NI USB-6343) to acquire data and to generate the driving signal which feeds into the shaker's amplifier. Acquisition and generation was performed at 32 kHz, several orders of magnitude higher than the highest frequency investigated in the present work. The data acquisition system interfaces with a PC using custom Labview software with PI (proportional-integral) feedback control that maintains the vertical vibration amplitude to within $0.002g$ of the specified target value. This accounts for any slow drift in acceleration amplitude that may occur, often a result of the considerable heat generated by the shaker during operation which affects its efficiency [106]. To measure the acceleration amplitude from the accelerometer data, we extract the amplitude of the highest peak in the frequency spectrum, which was always within 0.02% of the input frequency f. Furthermore, to assess the tonal purity of the vibration, we monitored the total harmonic distortion (THD). The THD was compute as the ratio of square root of the sum of the squares of the amplitudes of the harmonics to the amplitude of the fundamental tone. The THD was always less than 0.02 in the present experiments, unless otherwise stated. Note that the THD is a highly non-linear measurement,

in particular it increases with increased vibration amplitude. The total root mean square (RMS) amplitude of broad-spectrum noise in our acceleration measurements was less than $0.005g$ for our base test shaker measurements and less than $0.05g$ for our air bearing setup when compressed air was supplied to the linear air bearing. The increase in broad-spectrum noise was due to minor fluctuations in the air supply pressure. However, the increased noise occurred predominantly at high frequencies ($> 10^3$ Hz), resulting in no noticeably increased noise in the amplitude measurements at our test frequencies (20-150 Hz).

The data for this work was collected using a stepwise increase in frequency, with a step size of 2 Hz, over a range of 20 to 150 Hz. After each change in the frequency, we waited for the acceleration amplitude to converge to within $0.02g$ of the target value before collecting data. For measurements of vertical vibration homogeneity, the feedback controller was set to hold the mean acceleration amplitude to a fixed value of $\gamma_V = 4g$. For horizontal vibration measurements, the reference (vertical) accelerometer was set to maintain a fixed amplitude of $4g$. For all payloads, the static load offsets the equilibrium position of the armature, effectively reducing the maximum achievable peak-to-peak amplitude of the shaker. Thus for heavy payloads, at the lowest frequencies, we necessarily reduced the acceleration amplitude to avoid damaging the shaker. An alternative option would have been to attach an external suspension to the armature or payload, as in [106], which would restore the armature to its unloaded equilibrium position, and the factory specified peak-to-peak range. For the purpose of the present testing, we decided against this option, as this may have introduced further undesirable resonances to the base system, that are no longer directly attributable to the test shaker.

In the next section we proceed by measuring the quality of the vibration of our test shaker in the absence of external modifications.

2.1.2 Baseline performance of test shaker

Test procedure

To perform our baseline performance measurement of the test shaker, we mount a square precision ground aluminum mounting plate (88.9 mm L x 88.9 mm W x 9.5 mm thick) directly to the armature platform. The vertical mounting holes for the accelerometers are spaced 40.4 mm from the center of the platform. To study the influence of the payload weight on the shaker performance, we add an optional number of steel plates (each 152.4 mm L x 152.4 mm W x 6.4 mm thick) beneath the accelerometer mounting plate and atop a second precision aluminum plate (with identical dimensions to the upper plate). Up to four steel plates were added, which corresponded to a total payload of 5.0 kg. The plates (and bolted assembly) were designed to have fundamental frequencies greater than 10^3 Hz, well above our frequency range of interest (20-150 Hz). This ensures that our results are not contaminated by resonances of the payload.

Results

The first test performed was with a minimal payload (only the mounting plate and accelerometers installed, total payload mass m = 0.23 kg), to evaluate the performance of the bare shaker. In figure 2-2c, we present measurements of differences in the vertical acceleration at two diametrically opposed locations on the mounting plate. For low frequencies ($f \leq 76$ Hz), the forcing is relatively uniform, with differences no greater than 1.0%. However, as the frequency is increased we see that an acceleration bias steadily grows and then rapidly changes orientation, with the difference peaking at $9.2 \pm 1.0\%$ at 124 Hz. From here up to 150 Hz, the magnitude of the difference diminishes.

The shaded region in figure 2-2c represents the extent of the results of several repeated trials. Following each trial, the mounting plate was rotated 90 degrees and the accelerometers remounted so they continue to measure vertical accelerations along the same line (eg. see figure 2-2a), relative to the shaker. As can be seen, small

discrepancies exists between runs; these are the random errors discussed in section 4.1.1. The magnitude of random error was not independent of the test parameters, but was higher near frequencies with significant vibration inhomogeneities, with a maximum of about ±1%.

Comparing this data to the corresponding measurement of horizontal vibration presented in figure 2-2d, we see that the strongest inhomogeneities in the vertical vibration coincide with greatly amplified horizontal vibration. The peak of horizontal vibration occurs at 120 Hz and is 11.2 ± 2.5% of the vertical vibration amplitude. Since the armature, payload, and support structure have natural frequencies much greater than our test frequency range, we suspect that a resonance of the armature's suspension (internal to the shaker) is excited at these frequencies, which results in the observed non-axial motion.

We remeasure the shaker vertical performance with a heavier payload (m = 3.9 kg) as shown in figure 2-3a and present the results in figure 2-3b. The performance characteristics have changed dramatically. In particular, appreciable inhomogeneities in the vertical forcing amplitude appear at much lower frequencies than previously. As was the case with a minimal payload, we see that the onset of uneven vertical forcing coincides with strong horizontal vibration, as evidenced in figure 2-3c. In fact, a single distinct and dominant peak in the horizontal vibration appears for all payloads considered, and is always associated with the onset of inhomogeneities in the vertical vibration. We tested several different payloads, and for each we identified the frequency (f_H) within our range that corresponds to the peak horizontal vibration amplitude, which we refer to as the transverse resonant frequency. The results are plotted in figure 2-4. A clear monotonic relationship exists: the transverse resonant frequency decreases with the mass of payload, a result one might expect for a simple mechanical resonance. In fact, the data is very well described by a relationship of the form

$$f_H = \frac{1}{2\pi}\sqrt{\frac{k_H}{m}} \tag{2.1}$$

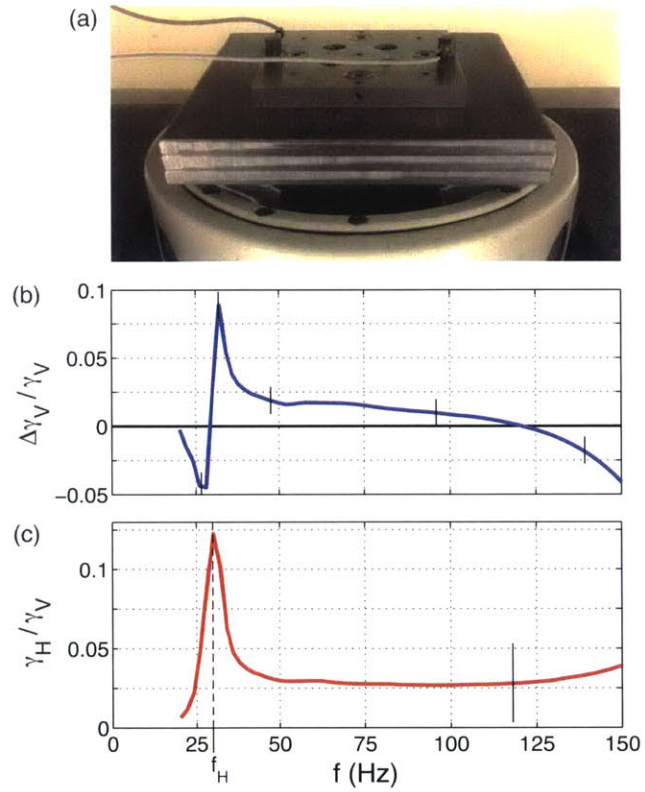

Figure 2-3: Performance of test shaker with payload of m = 3.9 kg, as shown in (a). (b) Normalized difference in vertical acceleration amplitude measured in two diametrically opposed locations on mounting plate. Characteristic error bars corresponding to estimated random errors are shown. (c) Acceleration amplitude of horizontal vibration. The peak of lateral acceleration amplitude in the frequency range of interest is identified as f_H, here at 30 Hz.

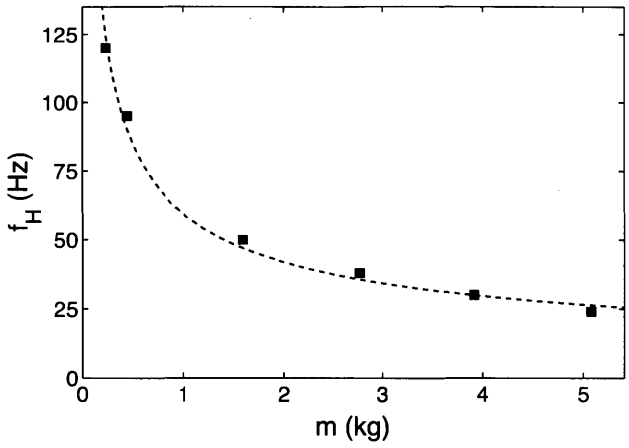

Figure 2-4: The dependence of f_H on payload mass m. The experimental data (■) is well described by a curve (dashed line) of the form given by equation (2.1) with k_H = 0.14 N/μm.

which is simply the undamped natural frequency of a mass m fixed to a linear spring with stiffness k_H. We find an excellent fit to the data taking k_H = 0.14 N/μm, which serves as a rough estimate of the lateral stiffness of the shaker suspension, and allows for the prediction of the first undesirable internal resonance for an arbitrary payload. The excellent agreement provides evidence that the non-axial motion is, as postulated, linked to mechanical resonances internal to the shaker. Moreover, the relative phase of the horizontal and vertical vibration changes most rapidly near the transverse resonant frequency. This effective lateral stiffness is an order of magnitude greater than the axial stiffness of the flexure plates (k_V = 0.0176 N/μm, manufacturer specification). Regrettably, there is no measurement of the lateral stiffness provided by the manufacturer with which to compare our estimate.

One seemingly reasonable solution might be to continue to load the shaker (assuming sufficient shaker capacity) to shift the transverse resonant frequency completely below the frequency range of interest. However, it is clear from the results in figure 2-3b that the performance is not satisfactory even well beyond this principal transverse resonant frequency. Moreover, as the shaker is loaded further, other higher internal resonances are shifted within our frequency range of interest. For our test shaker, in the absence of modifications, the first undesirable internal resonance, as characterized

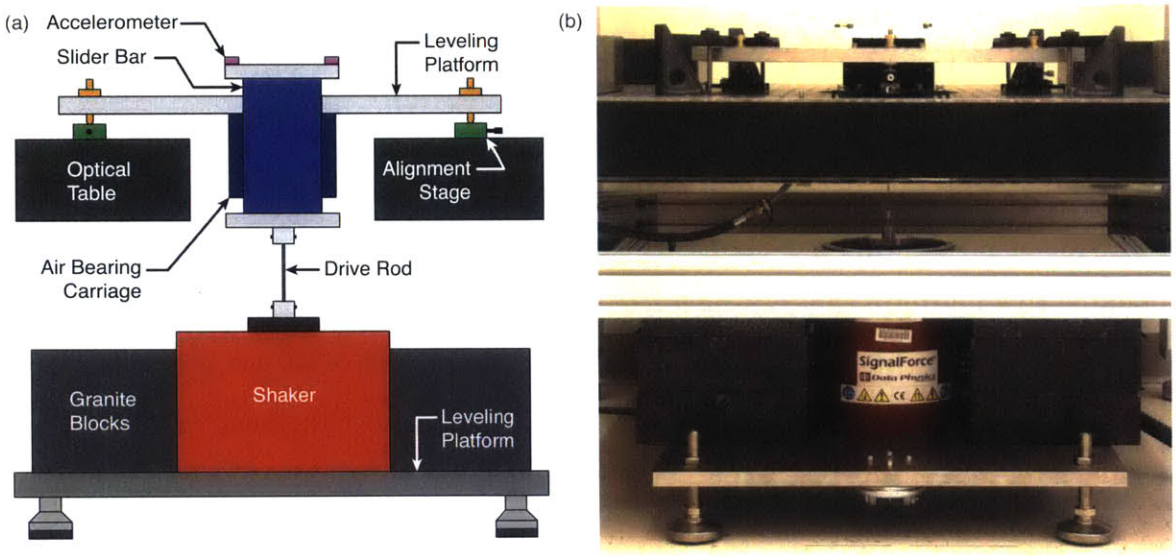

Figure 2-5: (a) Schematic and (b) image of the improved setup with external air bearing.

by equation (2.1), defines a frequency above which the motion is generally irregular.

The results presented in this section should appear troubling to anyone interested in careful forced vibration experiments. Minor changes in frequency or payload can result in potentially drastic changes in vibration performance. One point that cannot be overstressed is that despite the care in which one designs the payload to avoid resonance, significant discrepancies in the vertical vibration amplitude may still appear systemically due to the poor vibration quality provided by the source, the electrodynamic shaker. We also emphasize that the general issues presented here are not peculiar to this particular shaker, or this brand of shakers. Indeed, while the precise characteristics of the internal resonances will differ between models, undesirable performance arising at frequencies well below the armature resonant frequency is common to all flexure-based electrodynamic shakers [13]. The goal of the remainder of this paper is to present a method that will enable us to use the same electrodynamic shaker as a reliable and robust source of uniaxial vibration.

2.1.3 Improved design

We present a schematic and image of our improved setup in figure 2-5. The shaker is fixed to the same leveling platform as described in section 4.1.1. The key new feature is the linear air bearing (to be discussed in section 2.1.3), the carriage of which is mounted to a platform that can be leveled by way of three locking micrometer screws (100 threads per inch), spaced 254 mm from the central axis of the air bearing. These screws are fixed to linear translation stages which allow for adjustment of the lateral alignment of the central axis of the air bearing carriage with the shaker. This assembly is mounted to an optical breadboard with a centered through-hole which in turn rests on four passive air mounts (Barry Controls, SLM-1A). These isolators have a very low natural frequency ($\sim 3-4$ Hz) which help to isolate the table and carriage from any floor vibrations. The slider bar of the air bearing is connected to the shaker via a thin drive rod that is stiff in the direction of driving but relatively compliant in all other directions (to be discussed in section 2.1.3 and shown in figure 2-6a). On both ends, the rod is inserted into a reamed hole of at least 13 mm depth and set to length before being clamped in place by two diametrically opposed set screws on each end.

Accelerations are measured in a similar manner as before, atop a precision ground aluminum platform (127 mm L x 127 mm W x 12.7 mm thick), now mounted to the top of the air bearing slider bar. The vertical mounting holes for the accelerometers are spaced 54.0 mm from the center of the platform.

Bearing selection

To constrain the motion of the vibrating platform to a single axis we opted for an air bearing, many advantages of which are described by Slocum [96]. First, they are the smoothest operating of all bearings: the air layer eliminates the influence of any small surface defects. Second, they are unaffected by wear or loss of contact typical of slider or roller bearings. Third, they have no static friction and negligible dynamic friction for our expected operating speeds. Contact bearings have been used in other variations of this experimental setup [102]; however, it was noted that a small

amount of position dependent friction resulted in increased harmonic distortion. The gap thickness of an air bearing is generally less than that of hydrostatic bearings, making air bearings preferable for high precision equipment.

We selected a linear air bearing with a square cross section, as this geometry offers impedance to both twisting and lateral motions. To minimize non-axial motion, we would like to maximize the lateral stiffness of the air bearing. The lateral stiffness of a linear air bearing can be estimated as [96]

$$k_{AB} = \frac{0.6(L-a)Wp_s}{h_o}, \tag{2.2}$$

where L and W are the height and width of the bearing surface, a is the distance from the row of orifices to the outlet of the bearing, p_s is the supply pressure, and h_o is the unloaded gap thickness. From equation 2.2 it is evident that we would like a large bearing surface, high supply pressure, and small bearing gap. Thus we expect the best results for the largest possible bearing operating at the highest allowable input pressure. We selected a square air bearing composed of anodized aluminum (Nelson Air Corp.) with L = 102 mm, W = 100 mm, a = 20 mm, and h_o = 15 μm. At a supply pressure of p_s = 414 kPa (60 psi), we estimate the bearing stiffness using equation (2.2) to be k_{AB} = 136 N/μm which is close to the manufacturer specified value of 105 N/μm. We operate the bearing at its maximal supply pressure of p_s = 520 MPa (75 psi), above which we observe instability due to the pneumatic hammer effect. The lateral stiffness of the air bearing exceeds that of the shaker by several orders of magnitude.

Drive rod selection

The introduction of a thin coupling rod is a common technique used in modal testing of mechanical structures [49]. The thin rods that couple the shaker to the test structure are commonly referred to as "push rods" or "stingers." Stingers are used in modal testing to allow for efficient transmission of axial forces to the test structure while minimizing lateral constraint forces and moments at the point of attachment. In

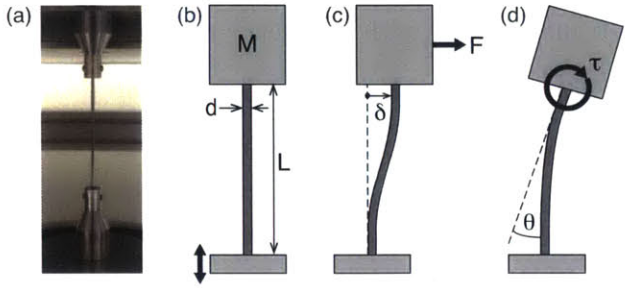

Figure 2-6: (a) Close-up image and (b) schematic of drive rod. Diagrams defining the (c) lateral stiffness, $k = F/\delta$, and (d) moment stiffness, $\kappa = \tau/\theta$, of the drive rod.

Symbol	Meaning	Value
E	Young's modulus	205 GPa
ρ	Density	7830 kg m^{-3}
σ_e	Endurance limit	515 MPa
d	Diameter	1.6 mm
L	Length	60 mm
A	$= \pi d^2/4$, Cross-sectional area	2.0 mm^2
I	$= \pi d^4/64$, Area moment of inertia	0.32 mm^4
k	$= 12EI/L^3$, Lateral stiffness	3.7 N/mm
κ	$= 4EI/L$, Moment stiffness	0.077 N-m/deg
M	Mass of payload supported by rod	3.0 kg
m	Mass of entire payload	3.2 kg
f_m	Maximum test frequency	150 Hz
γ_m	Acceleration amplitude	$4g$

Table 2.1: Symbols, definitions, and design parameters used in the present experiments for a drive rod with uniform circular cross-section.

general, the non-axial stiffnesses of the stinger should be significantly less than those of the test structure in order to avoid serious influences to the measured frequency response function (FRF) [21]. Furthermore, resonances of the stinger should also be avoided or highly damped, as these can readily contaminate the measured FRF [2, 49].

The primary design objectives for a drive rod in our system are similar to those for the stinger used in modal testing. Specifically, we would prefer high axial stiffness (for pure transmission of forces in the axial direction), low lateral and moment stiffnesses (relative to those of the shaker and air bearing), and no stinger resonances. The use of a flexible drive rod in the present system reduces the need for excessive alignment of the air bearing housing with the shaker's primary drive axis [58, 93, 36, 35]. As the internal gaps of an air bearing are typically on the order of 10 μm [96], in the absence of a flexible drive rod, micron-resolution in the lateral and angular alignment would be necessary in order to avoid excessive mechanical stresses on the shaker and air bearing assembly. One further advantage of using a flexible drive rod is that it acts as a mechanical fuse between the shaker and payload so that an accidental over forcing of the system will simply lead to the failure of the inexpensive drive rod, rapidly decoupling the shaker from the payload [88].

In what follows, we summarize our principal criteria for the system's drive rod. Note that many of the design principles are naturally transferrable from optimal stinger design [66, 2]. For simplicity and their wide range of availability, we choose to use a solid drive rod with uniform circular cross-section.

We first consider the possibility of axial failure under periodic loading. The amplitude of the cyclical force experience by the rod is simply the product of the mass M of the payload supported by the rod and the peak driving acceleration γ_m. To ensure longevity of the driving rod, we require that the maximum axial stress remains less than the endurance limit σ_e of the selected material. This gives us a minimum rod diameter, d:

$$d > \sqrt{\frac{4M\gamma_m}{\pi\sigma_e}} = d_e. \tag{2.3}$$

Note that in non-corrosive environments, the value of σ_e is generally independent of loading frequencies below 200 Hz, and independent of size for diameters less than 10 mm [97].

We next consider the possibility of axial or longitudinal resonance. A uniform rod deforms like a linear spring in response to an axial load, with spring constant [9]

$$k_a = \frac{EA}{L}, \tag{2.4}$$

where E is the rod's Young's modulus, $A = \pi d^2/4$ is its cross-sectional area, and L its length. The drive rod supports a mass M, and is driven from below, as depicted in figure 2-6b. Provided that the mass, M, of the supported load has a much greater mass than that of the drive rod, this mass-spring system has a natural frequency f_a given by

$$f_a = \frac{1}{2\pi}\sqrt{\frac{\pi E d^2}{4LM}}, \tag{2.5}$$

where d is the diameter of the drive rod. Beyond the crossover frequency ($f > \sqrt{2} f_a$), the payload will begin to become isolated from the driver, and the transmission of vibration from the shaker to the air bearing slider will be attenuated. It thus becomes increasingly difficult to drive the payload to the desired amplitude [49]. Furthermore, near the axial resonant frequency, we typically measured increased harmonic distortion, possibly due to excitation of the drive rod. To avoid these complications, we require that the axial resonant frequency be greater than the highest frequency in our test range ($f_a > f_m$). We can thus rearrange equation (2.5) to deduce a restriction on the length of the drive rod:

$$L < \frac{Ed^2}{16\pi M f_m^2} = L_a. \tag{2.6}$$

Given that we aim to drive a relatively heavy load (several kilograms) with a flexible beam, we also need to consider buckling of the drive rod. We design the beam such that it will withstand the maximum axial compressive force expected in our experiments, $|P_m|$. For sinusoidal vibration we can estimate this quantity from

Newton's second law,

$$|P_m| = M\,(\gamma_m + g)\ , \tag{2.7}$$

where γ_m is our maximum driving acceleration. Treating the drive rod as a clamped-clamped beam, we can express the buckling load ($|P_b|$) in terms of the rod parameters [9],

$$|P_b| = \frac{4\pi^2 EI}{L^2}\ , \tag{2.8}$$

where $I = \pi d^4/64$ is the area moment of inertia of the rod. To avoid buckling, we require that $|P_b| > |P_m|$. Equivalently, we write a restriction on the length of the drive rod:

$$L < \frac{d^2}{4}\sqrt{\frac{\pi^3 E}{M\,(\gamma_m + g)}} = L_b. \tag{2.9}$$

Finally, we would like to avoid transverse vibrational modes of the drive rod. Near a transverse resonance, any transverse vibrations (introduced by shaker or misalignment of drive rod) could be amplified [8], resulting in large lateral forces or moments applied to the air bearing slider. We thus use an expression for the fundamental transverse frequency of an unloaded uniform beam [9]:

$$f_{l,0} = \frac{\lambda_1^2}{2\pi L^2}\sqrt{\frac{EI}{\rho A}}\ , \tag{2.10}$$

where ρ is the density of the drive rod material and λ_1^2 is a coefficient that depends on the boundary conditions of the beam, and is approximately 22.4 for a clamped-clamped beam. The natural frequency will be altered by the presence of a constant axial load, as is the case in the present experiments resulting from the static force due to gravity. One can approximate the fundamental transverse frequency of a loaded beam as [12]:

$$f_l = f_{l,0}\sqrt{1 + \frac{P_s}{|P_b|}}\ , \tag{2.11}$$

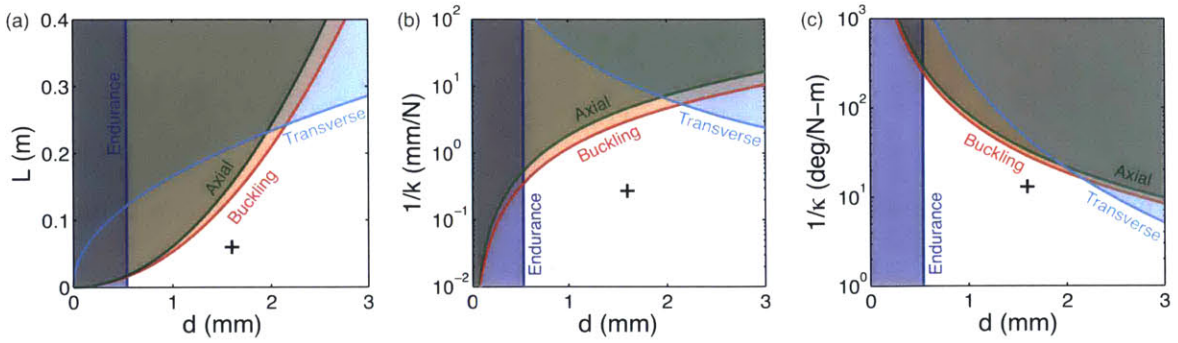

Figure 2-7: (a) Design region for drive rod, (b) lateral compliances of design region, and (c) moment compliances of design region. The curves represent bounds based on the avoidance of endurance-induced failure (2.3), axial resonance (2.6), buckling (2.9), and transverse resonance (2.13) as labeled, using the quantities from table 1. The shaded regions are forbidden or inaccessible due to at least one of these criteria. The marker identifies the location of the selected drive rod for the present application.

where P_s is the constant axial load (negative for compression, positive for tension). Note that for compressive loads, the natural frequency is reduced. Assuming we have adhered to our buckling condition ($|P_b| > |P_m|$), we can thus set a lower bound on the transverse frequency of the loaded beam:

$$f_l > f_{l,0}\sqrt{1 - \frac{g}{\gamma_m + g}} = \beta f_{l,0} \ , \tag{2.12}$$

where we have taken $P_s = -Mg$. Our correction factor to the unloaded natural frequency is $\beta = \sqrt{1 - \frac{g}{\gamma_m + g}}$ which is less than unity. Thus, finally we require that the maximum driving frequency be less than the loaded transverse frequency ($f_m < f_l$). Rearranging yields a condition on the length of the beam:

$$L < \sqrt{\frac{\beta \lambda_1^2 d}{8\pi f_m}} \left(\frac{E}{\rho}\right)^{\frac{1}{4}} = L_l. \tag{2.13}$$

If transverse resonances cannot be avoided, surrounding the drive rod in a damping material such as a soft polyurethane foam may improve results by dampening the resonant behavior of the drive rod, a technique demonstrated to be effective for resonant stingers [2].

We have thus arrived at four criteria for drive rod selection: namely the avoidance

of fatigue-induced failure (2.3), buckling (2.9), axial resonance (2.6) and transverse resonance (2.13). For our selected material (W1 tool steel) and the design parameters summarized in Table 1, we can thus isolate our possible design space in the L-d plane, shown as the unshaded region in figure 2-7a. We immediately see that the maximum length of thin rods is limited by the buckling condition, whereas for thick rods the length is limited by the threat of transverse resonance. Given that the buckling length (L_b) and the length necessary to avoid axial resonance (L_a) both scale with the diameter of the rod squared ($L \sim d^2$), the more restrictive criteria for a particular application will thus be determined by the relative magnitudes of their pre-factors.

Ideally, we would like to select a rod that minimizes both the lateral stiffness (k) and the moment stiffness (κ), described schematically in figures 2-6c and 2-6d, respectively. For the present geometry, the lateral stiffness of the rod may be expressed as [66]

$$k = \frac{F}{\delta} = \frac{12EI}{L^3} = \frac{3\pi E d^4}{16L^3}, \tag{2.14}$$

and the moment stiffness of the rod as

$$\kappa = \frac{\tau}{\theta} = \frac{4EI}{L} = \frac{\pi E d^4}{16L}. \tag{2.15}$$

We can then replot our design region to show the possible lateral compliances ($1/k$) in figure 2-7b and moment compliances ($1/\kappa$) in figure 2-7c, both of which we would ideally like to maximize for our present application. It is clear from these figures that both compliances cannot be maximized simultaneously. However, we can identify a diameter (d_m, here about 2.2 mm) above which both the maximum possible lateral and moment compliances decrease if the rod size is further increased. This maximum diameter occurs here at the crossing point of the buckling and transverse resonance length criteria. This suggests a finite range of possible diameters to select from, $d_e < d < d_m$. In this range it is apparent that the smaller diameters give better moment compliance, while the larger diameters give better lateral compliance. In fact, the maximum product of the compliances, $1/(k\kappa)$, is constant in this region,

suggesting the direct trade-off between the two. This can be easily understood, as the product of the compliances will be constant if the length of the rod increases as d^2, which is the same relationship ($L \sim d^2$) as both the buckling and axial resonance restrictions. We compromise by selecting a rod with a diameter near the middle of this region at approximately 50% of its maximum allowable length as a safety factor. Taking such a safety factory will also allow us a small amount of leeway should we later decide to adjust the experimental parameters (e.g. increasing the payload), without having to necessarily change the rod. For our selected rod parameters (d = 1.6 mm, L = 60 mm), we compute a lateral stiffness of 3.7 N/mm, which is several orders of magnitude less than the lateral stiffnesses of both the shaker and of the air bearing. For all of the results in the following section, we will use this drive rod unless otherwise stated.

Finally, we note that had we also considered maximizing the twisting compliance of the rod, the ultimate conclusion would be the same as that for maximizing the moment compliance of the rod (figure 2-7c). Specifically, we would like the rod be as thin as possible, with the maximum length set by either the buckling or axial resonance condition.

2.1.4 Testing of improved design

In figure 2-8a, we show the accelerometers mounted to the test platform in the configuration for testing the homogeneity of the vertical vibration. These results are presented in figure 2-8b. The solid line represents the average of thirteen frequency sweeps, while the shaded region indicates the complete range of measurements. As before, following each trial, the mounting plate was rotated 90 degrees and the accelerometers were remounted to assess the influence of random errors. The maximum vertical vibration inhomogeneity has been significantly reduced over the unmodified test shaker (figure 2-2c) by a factor of approximately 100. There is also an appreciable reduction of random errors over the baseline measurements, with a maximum now of about ±0.3% for the highest frequencies considered, but less than ±0.15% for frequencies below 100 Hz. We also tested the performance after adding an additional

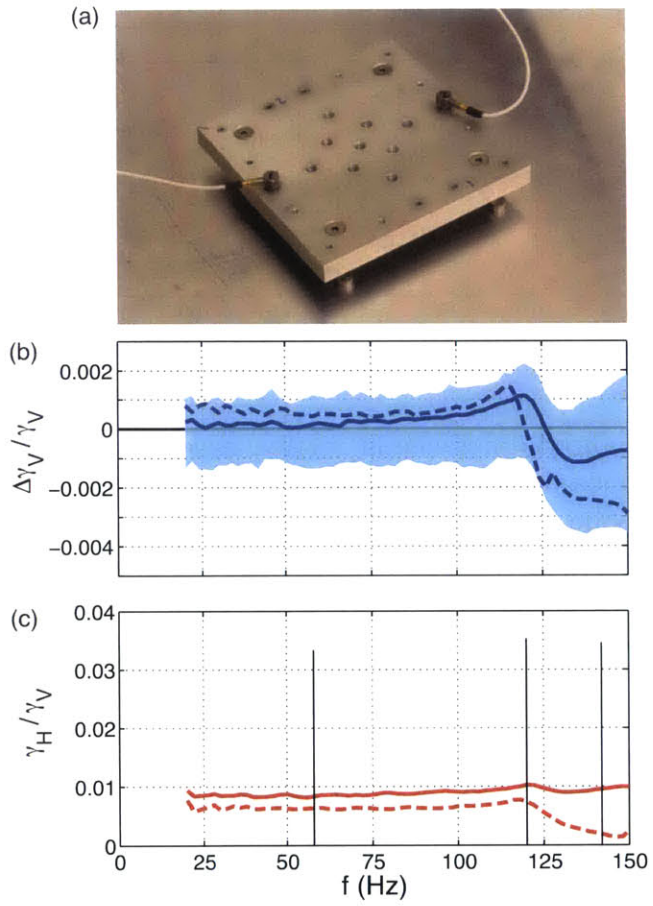

Figure 2-8: (b) Normalized difference in vertical acceleration amplitude measured in two diametrically opposed locations atop the air bearing slider as shown in (a). The solid line is the mean of thirteen frequency sweeps with a total shaker payload of m = 3.2 kg, while the shaded region indicates the complete range of measurements. The dashed line represents a measurement with an additional 2.8 kg mounted atop the slider bar. (c) Acceleration amplitude of horizontal vibration, with a base payload (m = 3.2 kg, solid line) and a heavy payload (m = 6.0 kg, dashed line).

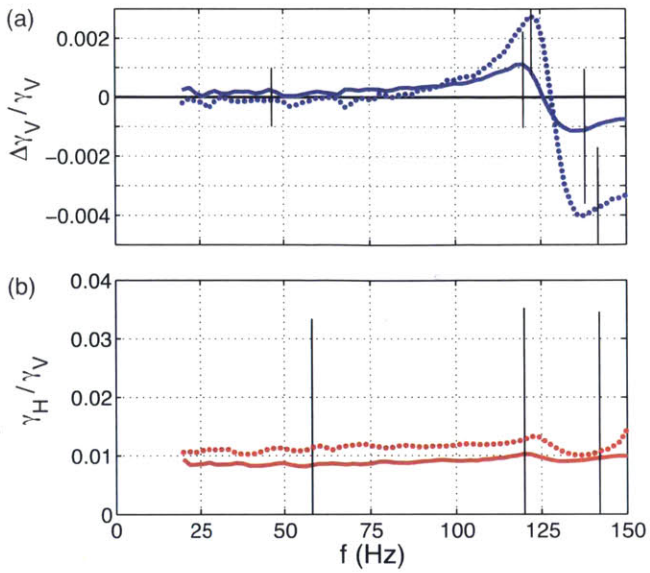

Figure 2-9: (a) Normalized difference in vertical acceleration amplitude measured in two diametrically opposed locations atop the air bearing slider with base payload (m = 3.2 kg). The solid line is the result for the drive rod of length L = 60 mm. The dotted line is the result for the drive rod of length L = 40 mm, with the same diameter. Characteristic error bars corresponding to estimated random errors are shown. (b) Acceleration amplitude of the corresponding horizontal vibrations.

2.8 kg of payload to the mounting plate, the same steel plates used for the baseline testing. The result is given by the dashed line in figure 2-8. We see that there is no significant difference between the results, indicating that the response is no longer highly sensitive to the payload mass as was the case for the bare shaker. The slight deviations from uniformity appearing in both cases at high frequencies again coincide with an internal resonance of the shaker. We also measured the amplitude of horizontal motion for both the base and heavy payload in figure 2-8c. In both cases, the maximum horizontal motion is significantly reduced, always measured to be less than the transverse sensitivity of the accelerometers. However, we did measure an increase in the total harmonic distortion at high frequencies for the heavy payload (exceeding 2%). We suspect that this increase was due to the reduction of the drive rod's axial resonant frequency (f_a = 173 Hz) to a value just above our maximum test frequency.

We also explored the effect of decreasing the rod length from L = 60 mm to L = 40 mm while maintaining the same rod diameter, decreasing both the lateral and moment

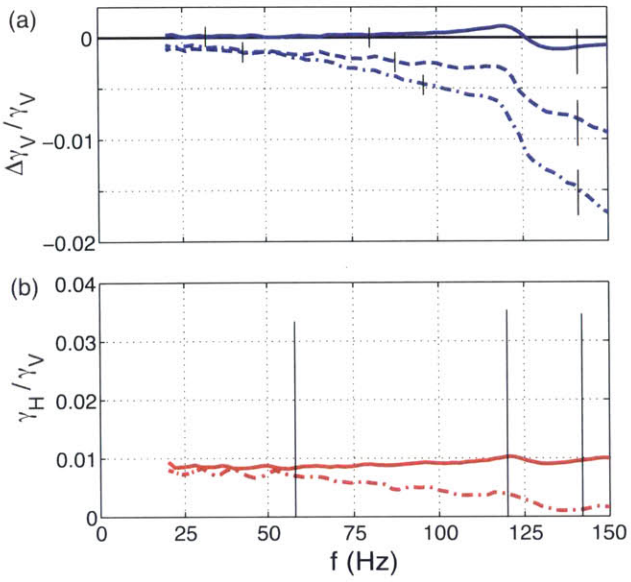

Figure 2-10: (a) Normalized difference in vertical acceleration amplitude and (b) acceleration amplitude of horizontal vibration atop the air bearing slider with different amounts of lateral misalignment along test axis between air bearing housing and shaker (solid line, δ = 0.0 mm; dashed line, δ = 0.4 mm; dash-dot line, δ = 0.8 mm).

compliances. In figure 2-9a, we observe an increased amplitude in the deviations from uniform vibration, suggesting that minimizing rod stiffnesses assists in reducing transmission of non-axial motion near a shaker resonance. Again, our measurements of horizontal vibration of the two rods were both less than the transverse sensitivity of the accelerometers, as shown in figure 2-9b.

Returning to the original L = 60 mm rod, we next investigated the influence of an intentional lateral misalignment on the performance. For these experiments we translated the air bearing leveling plate horizontally along the direction of the measurement axis, measuring the distance moved with a digital probe indicator. In figure 2-10a, we demonstrate that the intentional misalignment introduces an increase in the inhomogeneity of the vertical vibration. The vertical acceleration amplitude is greater on the side of the payload opposite to the direction we move the air bearing carriage. However, the amount by which the inhomogeneity increases is sensitive to the vibration frequency. Once again, our measurements of horizontal vibration of the two rods were always less than the transverse sensitivity of the accelerometers, as

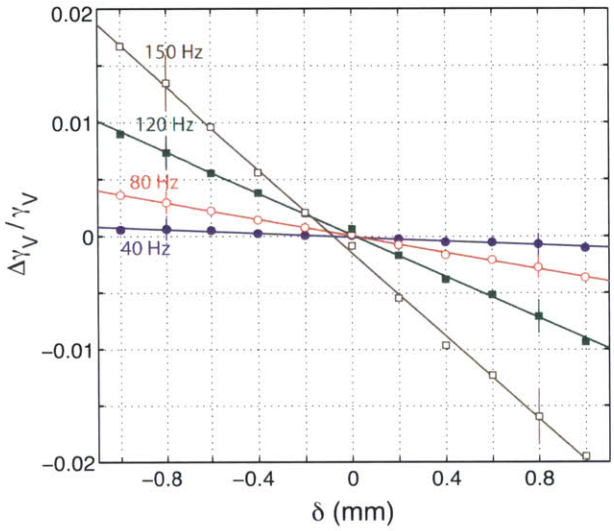

Figure 2-11: Normalized difference in vertical acceleration as a function of lateral misalignment (δ) along the test axis between air bearing housing and shaker for four different test frequencies. The lines are linear fits to the respective data sets. Characteristic error bars corresponding to estimated random errors are shown.

shown in figure 2-10b.

For four frequencies in our test range, we collected additional data to further characterize the effect of misalignment on the vertical vibration homogeneity. The results are presented in figure 2-11. For each frequency, we find a clear linear relationship between the misalignment distance δ and the difference in vertical vibration amplitudes on opposite sides of the plate, $\Delta\gamma_V$. One might notice that the curves do not all pass precisely through the origin. The shift (most apparent for 150 Hz) is due to internal shaker resonance of which we have seen that a small amount of inhomogeneity persists even for good alignment (recall figure 2-8b). Overall, these results suggest a straightforward method to calibrate alignment. At a given frequency, several measurements of inhomogeneity can be taken as a function of the lateral translation of either the bearing or shaker, from which the ideal alignment can be easily extrapolated. Additionally, as was also evident in figure 2-10a, this sensitivity to misalignment increases as the frequency is increased. Despite this shortcoming, one should not lose sight of the fact that the performance is still *significantly* improved over the baseline shaker (figure 2-2c), even with relatively severe misalignment. We also observed a globally

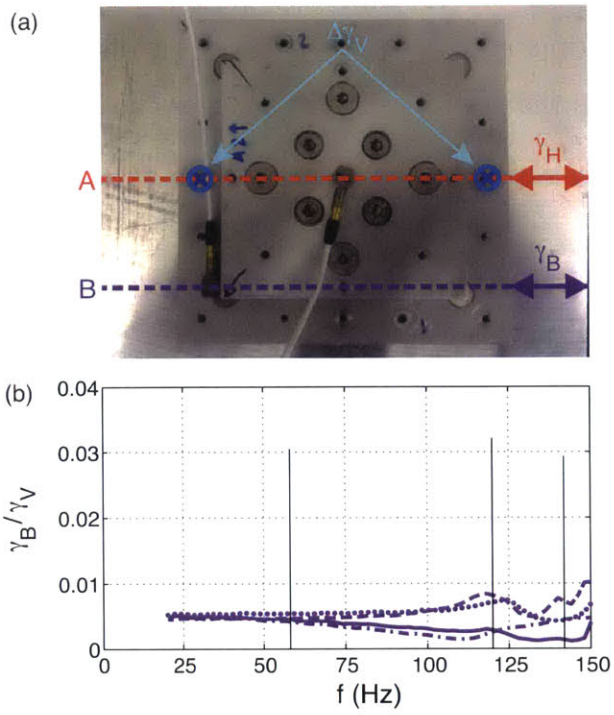

Figure 2-12: (a) Image of the accelerometer mounting plate for the air bearing setup. To assess the possibility of twisting motions, we also measure the horizontal vibration amplitude along line B (γ_B), which is 40.4 mm off of the central axis of the shaker. The measurements of the horizontal vibration amplitude, γ_H, were taken along line A. (b) Acceleration amplitude of horizontal vibration (γ_B). The solid line is the result with a drive rod of length L = 60 mm, total payload m = 3.2 kg, and lateral misalignment δ = 0.0 mm; the dashed line is with L = 60 mm, m = 6.0 kg, δ = 0.0 mm; the dotted line is with L = 40 mm, m = 3.2 kg, δ = 0.0 mm; and the dash-dot line is with L = 60 mm, m = 3.2 kg, δ = 0.8 mm.

increased sensitivity to misalignment when testing the shorter rod L = 40 mm, as might be expected. We suspect that there will be a similar performance sensitivity to angular misalignment, although this dependence was not systematically investigated.

Also, by measuring horizontal motion off axis, we found no significant twisting motion in any of the prior test cases, as evidenced in figure 2-12.

The only performance measurements of a similar system that could be found were reported by Deseigne *et al.* [35]. Their data suggests that above a frequency of about 60 Hz, the maximum difference of vertical vibration amplitude on the platform was never less than approximately 10%. The reason for this relatively large inhomogene-

ity is not clear. Unfortunately, they do not report the distance from the central axis at which they measure the vertical accelerations, as the measured differences in acceleration due to non-axial, rigid body motion should be linearly dependent on this distance. Furthermore, they use a large polystyrene cone to lift the plate above the air bearing, which places the center of mass of the payload much higher than the point of support, making the payload more susceptible to rocking motions. The selected frequency for their experiments (f = 115 Hz) lies between two apparent yet uninvestigated resonances in the system, easily identified by pronounced localized deviations from homogeneity.

To ensure high-quality vibration, even with the use of an external air bearing and properly designed drive rod, one must also carefully design the payload and the support structure for the air bearing to avoid resonances. For example, a resonance of the air bearing leveling plate will readily contaminate the results, as the carriage itself may no longer be rigidly fixed along a single axis. Throughout our development of the final design, aberrations in performance that were localized in frequency were always underlaid by some mechanical resonance in the system. Once identified, the component could be redesigned and the performance substantially improved. In general, we noticed that the improved system discussed herein was remarkably robust at low frequencies; however, more careful alignment and component design became necessary at higher frequencies.

The potential influence of drive rod resonances can easily be checked by varying the rod length and assessing whether the spurious resonant frequencies shift. If not, it is likely that the aberrations are caused by the resonance of some other component in the system.

2.1.5 Conclusions

We have demonstrated the efficacy of introducing a linear air bearing to rectify the non-axial motions typical of flexure-based electrodynamic shakers. We tested a standard shaker and observed a distinct mechanical resonance of the armature's suspension leading to non-axial motion of the payload. We have also demonstrated that

the performance of the unmodified shaker is sensitive to the details of the payload, including its mass. This resonance introduces large inhomogeneities in the vertical vibration amplitude as well as significant transverse vibrations of the armature. The frequencies considered are well below the resonant frequency of either the armature itself or the payload, and are typical of experimental investigations of vibrated granular materials, Faraday waves, and walking droplets.

We have presented the details of an improved design that incorporates an external air bearing to eliminate torsional motion and more effectively constrain the vibration to a single axis. We have provided general criteria for selection of a drive rod that couples the shaker to the air bearing slider. We have also presented our test results, which demonstrated a significant improvement of the vibration quality of the payload for our entire frequency range of interest (20-150 Hz). In particular, our design reduced the maximum inhomogeneity of the vertical vibration amplitude from approximately 10% to 0.1%. The details of our results have allowed us to arrive at several important conclusions concerning our new design. First, the performance is relatively insensitive to the mass of the payload, in stark contrast to the baseline shaker results. Second, minimizing the non-axial stiffnesses of the drive rod reduces the transmission of non-axial motions to the drive platform. Finally, we reported a linear dependence of the inhomogeneity of vertical vibration on the lateral alignment of the air bearing with the shaker. In all tests performed with the improved setup, the horizontal vibration and any potential twisting motions of the platform were too small to be detected by the accelerometers.

While the mild sensitivity to alignment might be seen as a shortcoming, it could also prove useful for certain investigations. In particular, intentional misalignment seems to be a controllable way to introduce imhomogeneous vibration into the system. One might thus investigate the influence of mildly inhomogeneous vibration on pattern formation in Faraday waves or on the trajectories of walking droplets.

Later in this thesis, we demonstrate that just below the Faraday threshold, the dynamical and statistical behavior of the droplets is extremely sensitive to the driving amplitude. Reliable results thus require the highly uniform driving and precise control

Symbol	Meaning	Value
ν	Kinematic viscosity	20.9 ± 0.1 cSt
ρ	Density	950 kg m^{-3}
σ	Surface tension	20.6 mN/m

Table 2.2: Fluid properties of Clearco Products pure 20 cSt silicone oil.

of the forcing amplitude made possible by our improved vibration system.

2.2 Droplet generation

The dynamical properties of bouncing and walking droplets are extremely sensitive to their size [91, 81, 82, 105]. Thus, a reliable method to generate droplets of a repeatable size is required for reproducible experiments. The fluid used for both the bath and droplets in all experiments throughout this thesis is Clearco Products pure 20 cSt silicone oil. Relevant fluid properties are included in table 2.2.

One common method to generate droplets of uniform size is by gravitational detachment from a needle, as shown in figure 2-13. When the mass of the suspended droplet exceeds the vertical force of surface tension, the droplet will detach from the tip and fall. If we assume that the fluid fully wets the outer surface of the needle (as in the case of silicone oil), we predict the radius of the droplet at detachment as

$$R = \left(\frac{3d\sigma}{4\rho g}\right)^{1/3} \tag{2.16}$$

where d is the outer diameter of the needle. Note that the droplet radius will scale with the diameter to the one-third power ($R \sim d^{\frac{1}{3}}$) meaning that in order to reduce the droplet diameter by one-half, the needle diameter must be reduced by a factor of eight. For the present oil, we predict that for a 32-gauge needle (d = 0.25 mm) the droplet generated at detachment will have a spherical radius of R = 0.75 mm, which

Portions of this section appear as published in: D. M. Harris, T. Liu, and J. W. M. Bush. Generating uniaxial vibration with an electrodynamic shaker and external air bearing. *Experiments in Fluids*, 56:83,2015 [63].

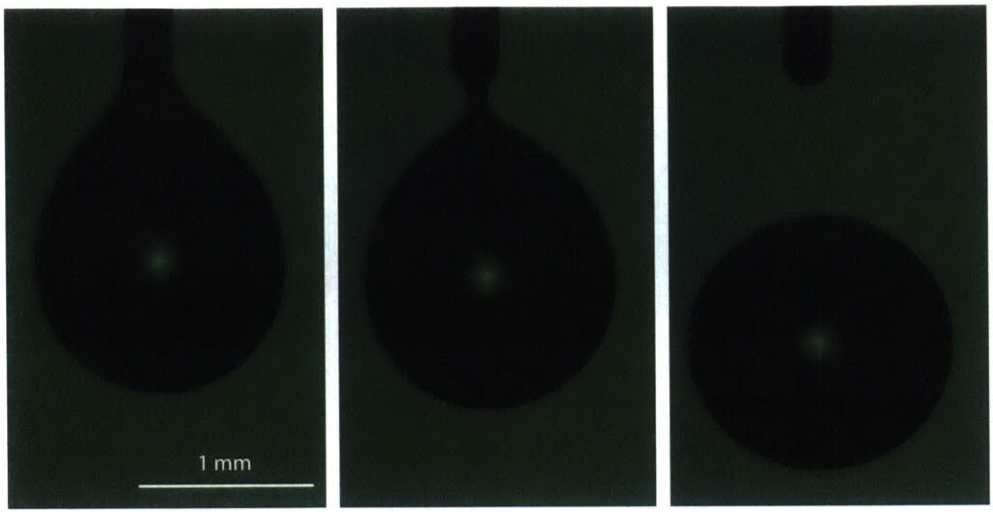

Figure 2-13: Pendant drop (R = 0.75 mm) detaching from a 32-gauge needle (d = 0.25 mm).

is precisely the value measured in the experiment shown in figure 2-13. In order to generate a droplet of radius 0.3 mm, a useful size for studies of bouncing and walking droplets, a needle with outer diameter of 16 μm would be required, smaller than the diameter of a human hair. This is clearly impractical, so we must use an alternate method to generate droplets for the present experiments. In the early experiments on bouncing and walking droplets, drops were generated by rapidly extracting a partially submerged needle from the fluid bath [91]. While this is an effective method for generating small droplets, it is difficult to create them of a repeatable size. In the following section, we describe our design of a piezoelectric droplet generator designed to produce droplets in the size range useful for the present experiments.

2.2.1 Piezoelectric droplet generator

The present design is inspired by the original design of Yang *et al.* [107] and a later design by Terwagne [100, 101]. A schematic of the droplet generator is shown in figure 2-14. The principal component of the droplet generator system is the fluid chamber, which is an aluminum block bored out and filled with silicone oil. On the base of the block is a threaded hole in which an interchangeable stainless-steel nozzle with specified outlet diameter can be connected. Sealed to the top of the fluid chamber

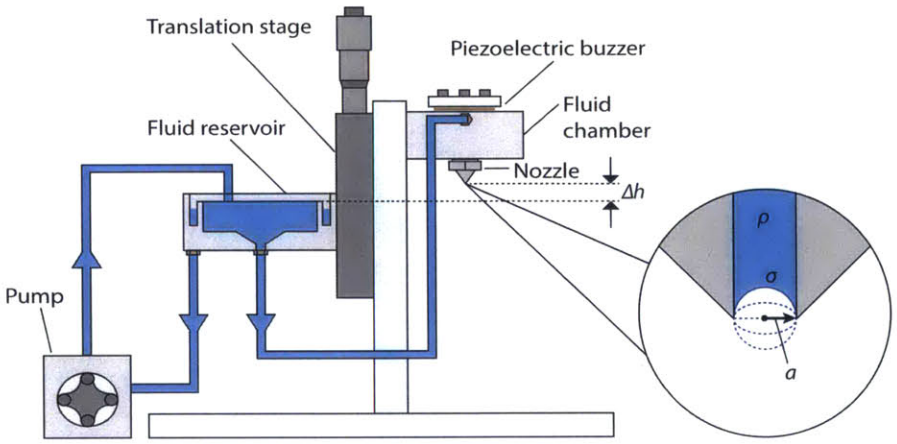

Figure 2-14: Schematic of droplet generator. Inset: the form of the static meniscus at the nozzle outlet depends on Δh, the difference between the reservoir and nozzle heights. As Δh increases, the fluid recedes into the nozzle. Stable static menisci arise for $|\Delta h| \leq 2\sigma/\rho g a$.

is a circular piezoelectric disc which flexes in response to an applied voltage. All air must be removed from the fluid chamber prior to experiments to ensure repeatable operation.

The fluid chamber is supplied by an external fluid reservoir. The fluid reservoir consists of two concentric cylinders, the inner of which overflows into the outer. The inner cylinder is continuously filled by a peristaltic pump, maintaining a constant pressure in the fluid chamber. The fluid reservoir is mounted on vertically oriented traverse, which can be used to adjust the pressure at the nozzle plane. All components can be machined on standard mill and lathe equipment.

The electrical system consists of an Aruduino Uno, H-bridge circuit, and an adjustable DC power supply. This electrical system allows for the generation of a square pulse with tunable amplitude and duration (pulse width). When a drop is to be generated, a square electrical pulse is sent to the piezoelectric disc which responds by expanding and contracting in sequence, generating a pressure pulse in the chamber. If the pulse is tuned to an appropriate amplitude and duration, a single droplet can be expelled. The droplet diameter is measured optically using an edge-detection algorithm in MATLAB.

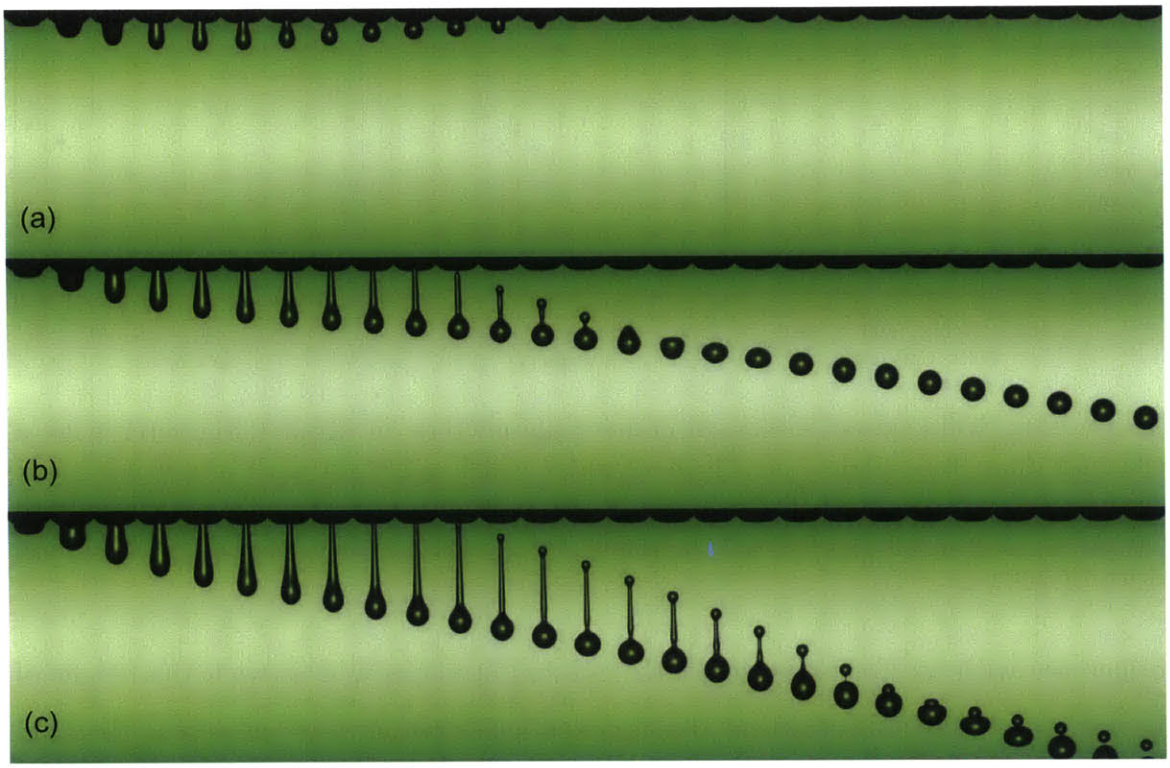

Figure 2-15: Dependence of droplet generation on pulse width for the same nozzle diameter (1.40 mm) and applied voltage (30 V). (a) No droplet is generated with a 460 μs pulse width. (b) A single droplet is generated with a 660 μs pulse width. (c) Multiple droplets are generated with a 850 μs pulse width. Neighboring images are separated by 1 ms.

Results

We first fix the nozzle diameter and pulse amplitude, and vary only the pulse width. As can be seen in figure 2-15, three distinct regimes are observed. Below a lower threshold in pulse width, a small amount of fluid is extruded but then rapidly retracts back into the nozzle, and no droplet is released. Above an upper threshold in pulse width, a primary droplet is expelled as well as a satellite droplet. However, for a finite range of pulse widths in between these bounds, a single droplet is generated. This range of desirable pulse widths varies with both the nozzle diameter and the pulse voltage amplitude.

For this single droplet regime, we explore the effect of varying the system parameters on the size of the ejected droplet (figure 2-16). The droplet diameter tends

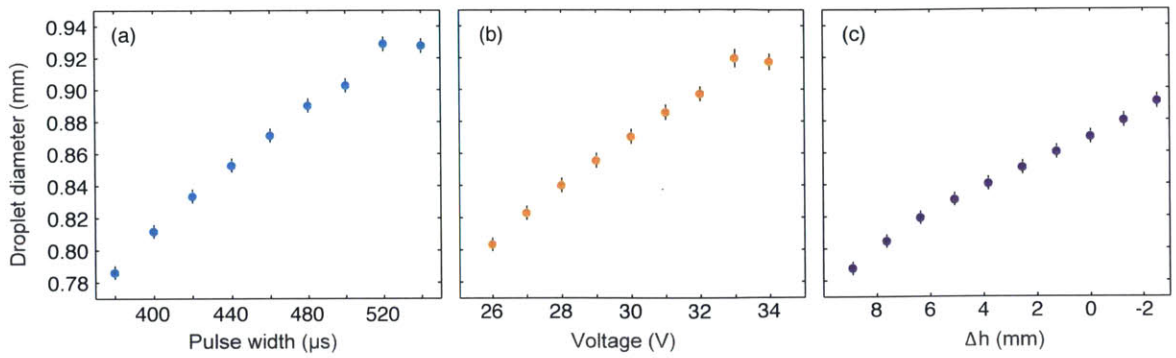

Figure 2-16: Influence of electrical control parameters on droplet diameter with a 0.90 mm diameter nozzle. (a) Effect of pulse width variation with amplitude 30 V and reservoir height $\Delta h = 0$. (b) Effect of voltage amplitude with 460 μs pulse width and $\Delta h = 0$. (c) Effect of reservoir height with pulse amplitude of 30 V and pulse width of 460 μs.

to increase with increasing pulse width and amplitude as well as with the height of the reservoir. This indicates that the electrical pulse parameters, as well as the fluid pressure at the nozzle plane can be used to control the droplet size, even with a fixed nozzle outlet diameter.

To extend the range of realizable droplet diameters, the nozzle can be interchanged with one of a different outlet diameter. We demonstrate in figure 2-18a that the range of pulse widths in which a single droplet is ejected varies with the nozzle diameter. Furthermore, in figure 2-18b, it is shown that the size of the droplet scales nearly linearly with the nozzle diameter, with a range for each nozzle achieved by variation of the pulse width. The overall variation in droplet size for fixed parameters is less than 1%.

To avoid coalescence in depositing the droplets onto the vibrating bath, we direct the droplets down a curved surface pre-wetted by a thin layer of silicone oil applied with a brush [55] as shown in figure 2-18. The drops thus impact the bath surface at an acute angle, thereby skipping and rolling before settling into a stable bouncing or walking state. Multiple bouncing droplets created in this fashion can self-organize into stable lattice arrangements [43] as demonstrated in Fig. 2-19.

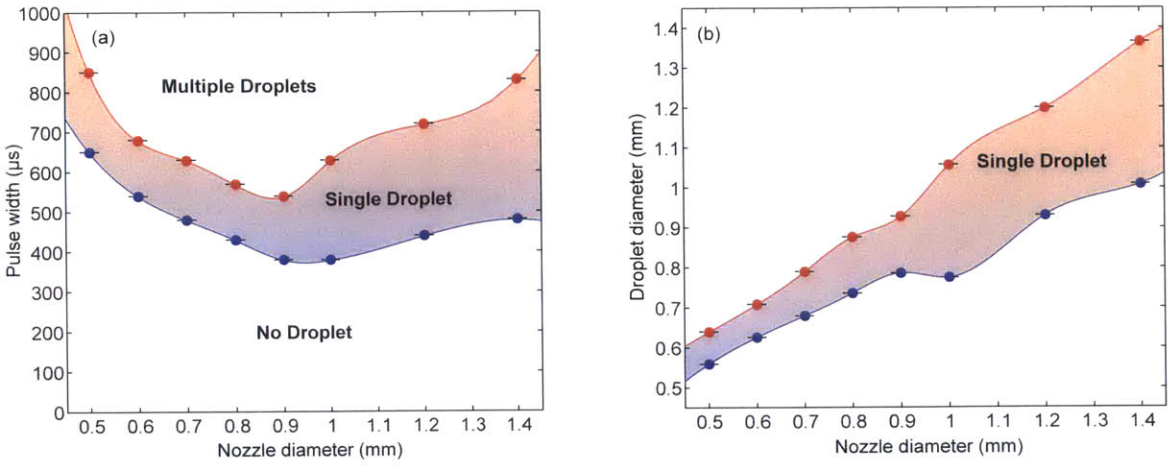

Figure 2-17: (a) Upper and lower curves represent the upper and lower pulse width limits for single droplet generation from nozzles with different diameters with a fixed voltage (30 V) and reservoir height ($\Delta h = 0$). (b) Droplet diameters for each nozzle evaluated at upper and lower pulse width limits.

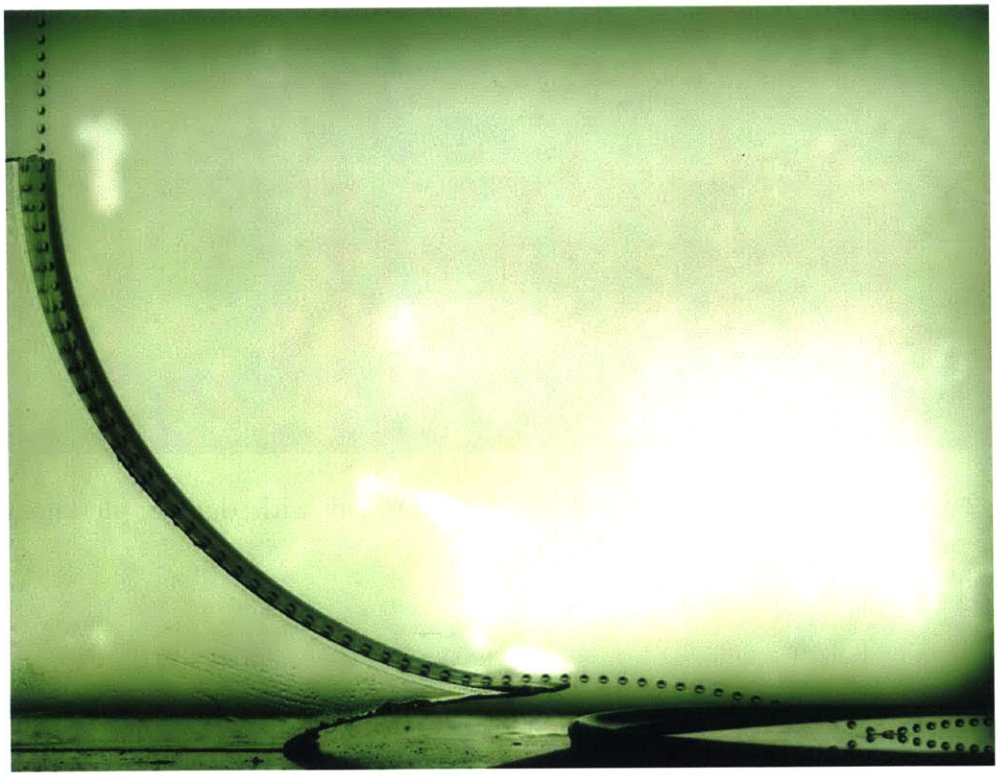

Figure 2-18: To deposit the droplets onto the fluid bath, they are directed down a curved surface wetted with a thin layer of silicone oil.

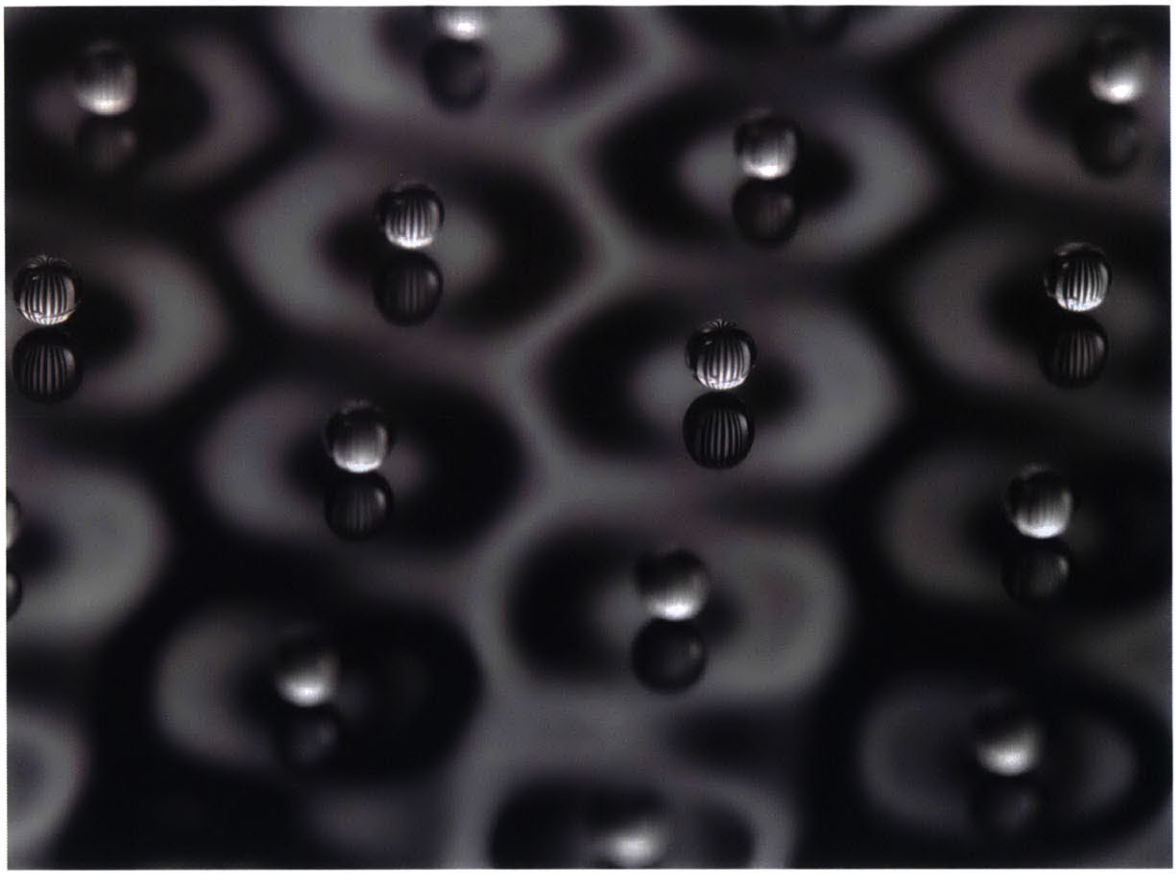

Figure 2-19: A stable lattice of oil droplets, formed with our droplet generator, bounces on the surface of a vibrated oil bath.

2.3 Visualization technique

We have developed a visualization technique that captures the aesthetic appeal of Faraday waves and bouncing droplets. An image of the setup is shown in Figure 2-20. A function generator drives a small speaker at approximately 70 Hz, upon which a petri-dish filled with silicone oil is fixed. The base of the dish is painted black in order to minimize light scattered from beneath the surface. The camera is positioned so as to view the reflection of a simple background pattern of colors behind the speaker. The external flash is placed ahead of the subject and illuminates the background pattern, the reflection of which can then be captured by the camera. Any distortion of the fluid interface results in an apparent distortion of the background image. Droplets can act as miniature lenses, bringing the overall background into focus. The camera used in this setup is a Canon Rebel T1i which was equipped with a 60 mm Macro lens and a Macro Twin Lite MT-24EX flash. This visualization technique is currently being adapted for use with color high-speed video.

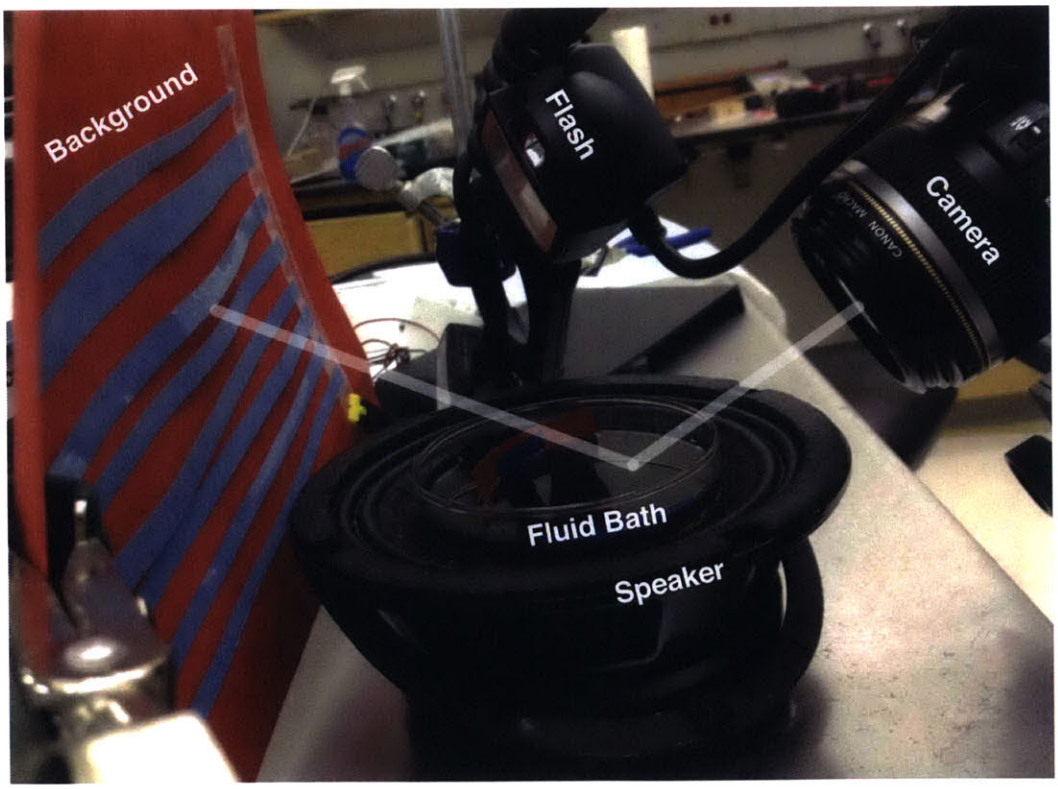

Figure 2-20: Setup for visualizing Faraday waves and bouncing droplets.

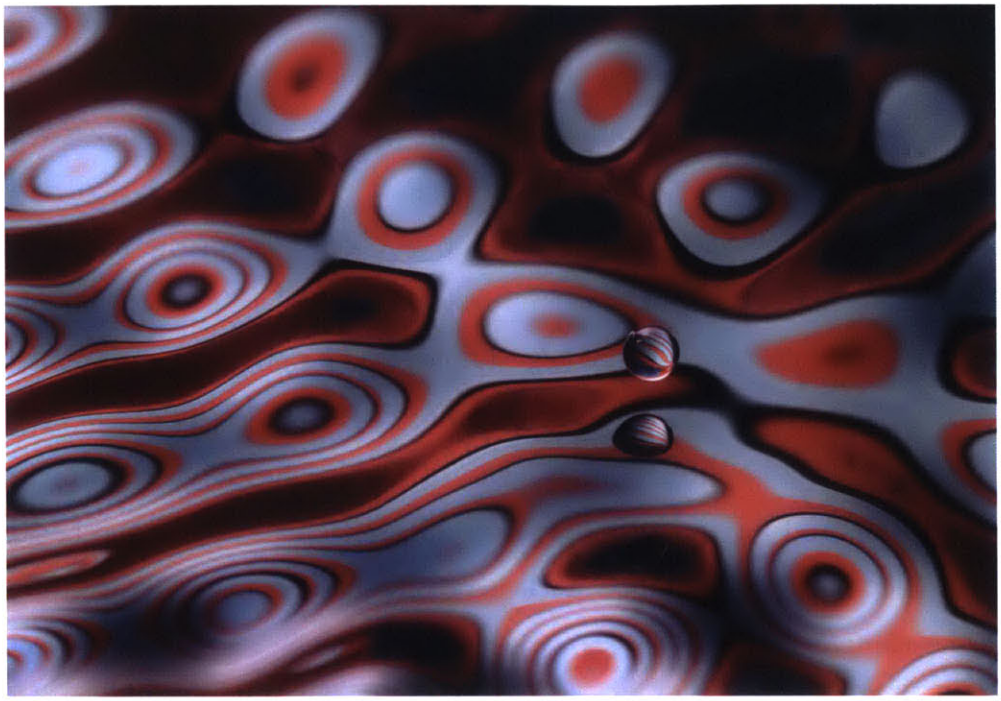

Figure 2-21: *Sinuous Separation.* A single droplet bounces in a field of Faraday waves. This image was captured using the setup shown in Figure 2-20 with a shutter speed of 1/3200 s, an aperture size of f/16, and an ISO setting of 1600.

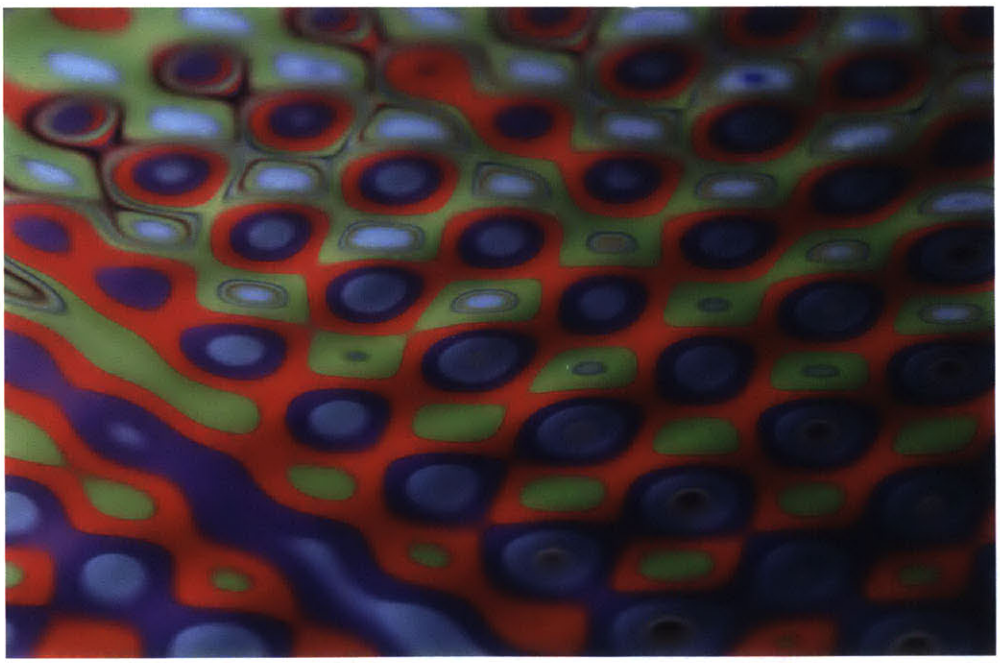

Figure 2-22: *Parametric Resonance.* A field of Faraday waves forms above a critical threshold.

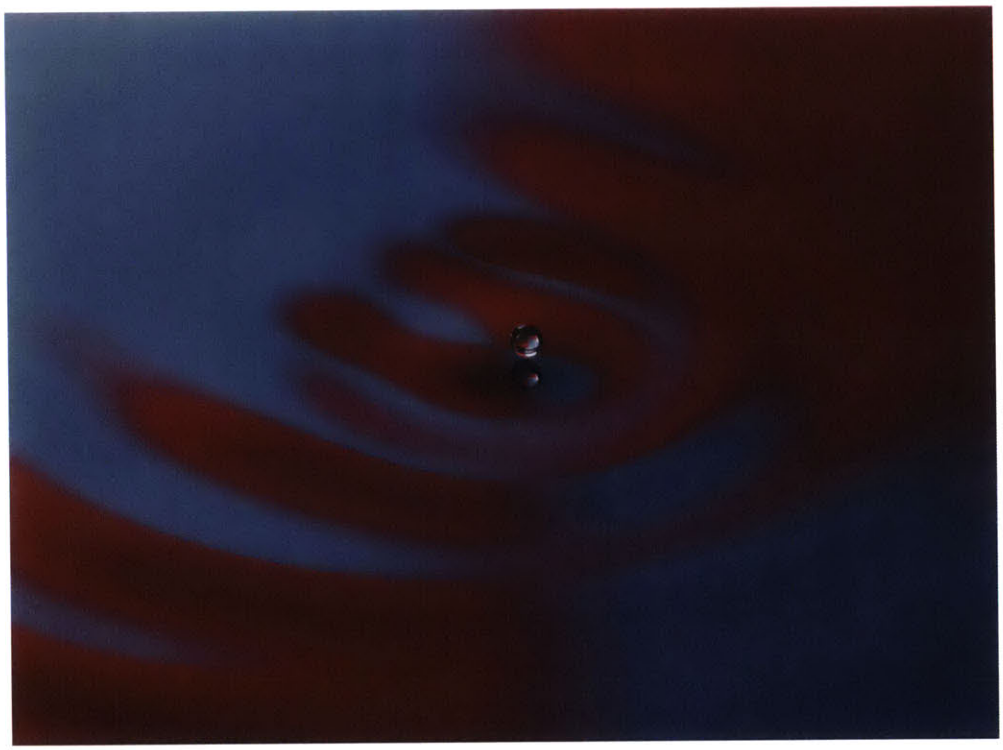

Figure 2-23: *Walking in Color.* A droplet walks across the surface of a vibrated fluid bath, propelled by its Faraday wave field.

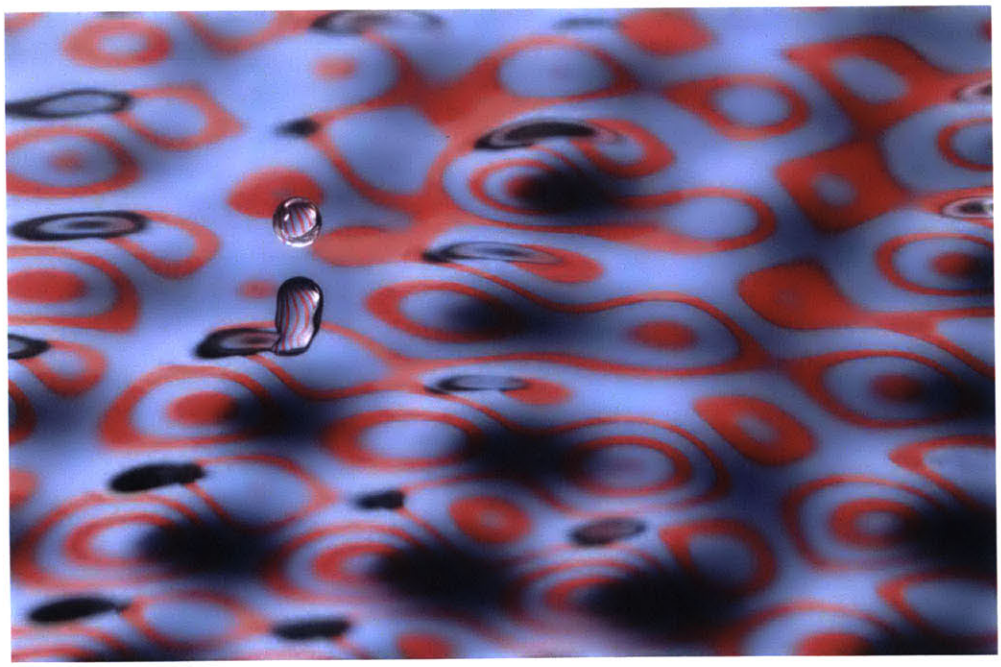

Figure 2-24: *Isolated Reflection on Duality.* A single droplet bounces in a field of Faraday waves.

Figure 2-25: *Emergent.* A droplet is expelled from the droplet generator.

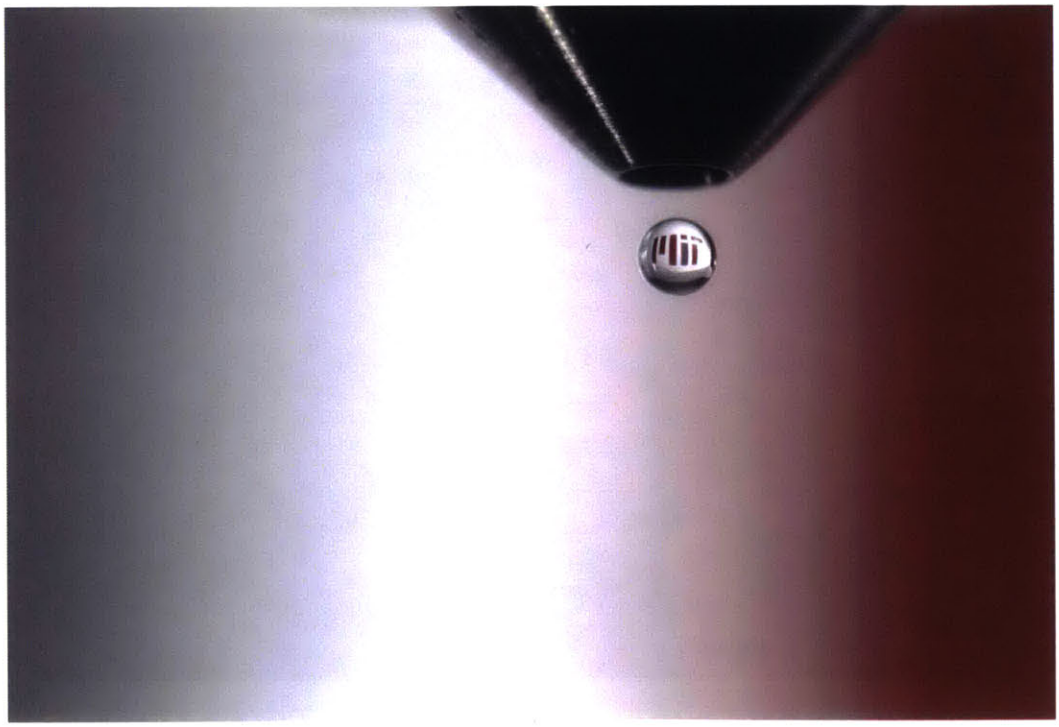

Figure 2-26: *Refocus.* A droplet brings a familiar logo into focus.

Chapter 3

Confinement to a corral geometry

We here examine the dynamics and statistics of droplets walking in confined geometries (see figure 3-1a). The bath consists of a relatively deep layer surrounded by a shallow layer of depth h_1 = 0.6 mm, the depths chosen to ensure that the droplet can only walk in the deep central 'corral' region. The walker is thus confined to the corral, while its guiding wave field is influenced by reflections off the corral edges. For our walker experiments, the forcing amplitude is always below the Faraday threshold, so the free surface would remain flat in the absence of the droplet.

3.1 Circular corral

Figure 3-1b illustrates the cavity mode just above the Faraday threshold at the driving frequency considered. We proceed by describing the dependence of the walker dynamics on the proximity to the Faraday threshold, which can be characterized by the dimensionless parameter γ/γ_F. As γ/γ_F approaches one, the path memory increases.

Figure 3-1c illustrates the circular trajectory of a walker with short path memory in a circular cavity. As the path memory is increased progressively, this circular orbit

This section appears as published in: D. M. Harris, J. Moukhtar, E. Fort, Y. Couder, and J. W. M. Bush. Wavelike statistics from pilot-wave dynamics in a circular corral. *Physical Review E*, 88: 011001, 2013 [64].

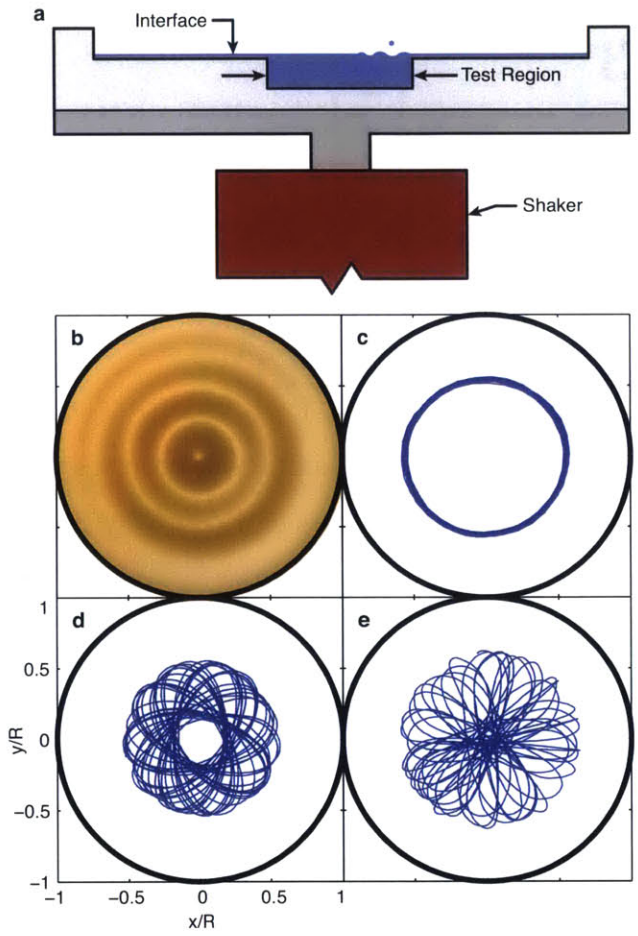

Figure 3-1: (a) A schematic illustration of the experimental apparatus, a fluid bath driven vertically in a sinusoidal manner with amplitude A_0 and frequency f. (b) The Faraday mode in a circular corral of radius $R = 10.1$ mm and depth $h_0 = 5$ mm, driven at $f = 80$ Hz, for which $\gamma_F = 4.6$, and the Faraday wavelength is $\lambda_F = 4.75$ mm. The frequency was selected to ensure that the wave field just above the Faraday threshold was stationary. Note that the bright rings correspond to areas of small surface slope, indicating local extrema of wave amplitude. (c-e) Typical trajectories of a walker with diameter $D = 0.8$ mm and mean velocity $\bar{v} = 11$ mm/s in the same circular corral at: (c) low memory $\gamma/\gamma_F = 0.82$, and intermediate memories (d) $\gamma/\gamma_F = 0.9$ and (e) $\gamma/\gamma_F = 0.94$.

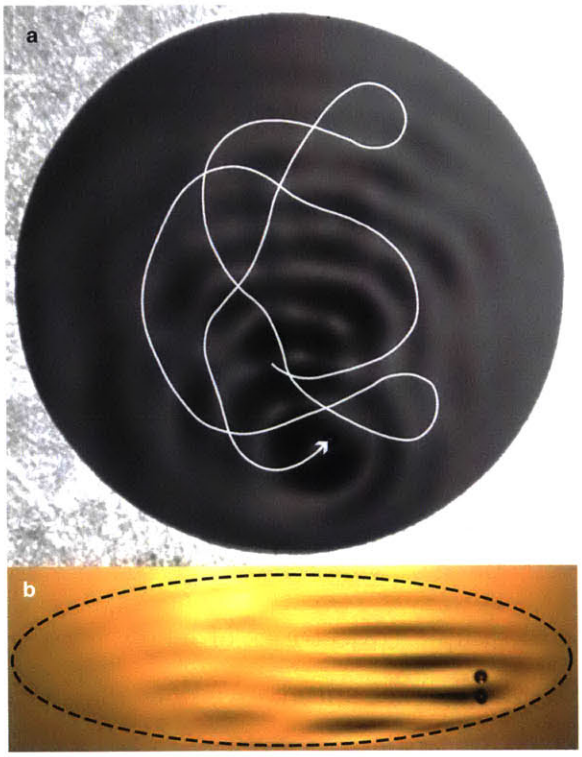

Figure 3-2: (a) Top view of a walker exploring a circular corral in the long-path-memory limit. Its complex pilot-wave field is apparent; its trajectory is indicated in white. (b) Oblique view of a walker exploring a circular corral. The dashed line indicates the edge of the corral.

becomes unstable, giving way to a epicycloidal trajectories with increasing deviations from the unstable circle (figure 3-1de). Figure 3-2 illustrates sample images of a walker and its guiding wave field in the long-path-memory limit. The walker's pilot-wave field is continuously evolving: while its peak amplitude is generally near the point of the droplet's last impact, its detailed form depends on the droplet's past trajectory. At any instant, the wave field is complex, the result of a superposition of waves created by the droplet's previous bounces: in general, it bears no resemblance to the resonant wave mode of the cavity. The dynamics in the long-path-memory limit thus cannot be simply rationalized in terms of stochastic motion modulated by the wave mode of the cavity. On the contrary, this pilot-wave dynamics has certain distinct features. Specifically, the monochromatic guiding wave field constrains the radius of curvature, which rarely takes values less than half the Faraday wavelength. The complex guiding wave field in this long-memory limit thus renders the walker's trajectory relatively smooth, but its dynamics chaotic. We note that this smooth pilot-wave dynamics is markedly different from that observed when the system is driven above the Faraday threshold, when the trajectory is relatively erratic and marked by sharp changes in direction.

Figure 3-3a illustrates sample trajectories of increasing length, which have been color-coded according to the droplet speed. We note that in the absence of boundaries, the walker speed would remain constant and its motion rectilinear. In this long-memory limit, the walker's trajectory is complex, owing to the interaction of its extended pilot-wave field with the boundaries; moreover, the walker speed varies significantly from its mean ($\bar{v}$ = 8.66 mm/s) along its path. In the long-time limit, a pattern emerges in the velocity fluctuations, a pattern that is echoed in the droplet statistics. The probability distribution presented in figure 3-3b indicates the emergence of a coherent wave-like statistical behaviour for the walking droplet.

The axially symmetrized histogram is shown in figure 3-4a along with the amplitude of the cavity mode, $|J_0(k_F r)|$, with the Faraday wavelength $\lambda_F = 2\pi/k_F$, as predicted by linear theory [5]. The correspondence between the two indicates that, as in quantum mechanics, the statistics of a confined particle can be prescribed by a

wave function satisfying a linear wave equation. If one fits the data to a linear superposition of cavity eigenmodes with wavelength closest to λ_F, the fit can be slightly improved and the zeros in the predicted probability amplitude disappear. However, this requires the introduction of additional fitting parameters, namely the amplitude ratio of each mode, so for simplicity we compare only to a single mode. Doing so indicates that the walker's probability distribution is well approximated by the amplitude of the linear Faraday wave mode of the corral.

There are several features of this pilot-wave dynamics that contribute to the emergence of the coherent wave-like statistical pattern. In figure 3-4b, we demonstrate that fluctuations in the walker's speed are correlated with its radial position, as was suggested by the color-coded trajectories presented in figure 3-3a. In general, the walker's speed is lowest at the locations of maximum amplitude of the fundamental cavity mode, augmenting the probability amplitude at these radii. The spatial distribution of the normalized radial velocity is presented in figure 3-4c, where we again observe a spatial periodicity, with the locations of the peaks corresponding roughly to the zeros in the amplitude of the cavity mode. This correlation may be rationalized in terms of the walkers' tendency to move azimuthally about preferred radii and radially in between, as is exemplified in sample trajectories reported in figure 3-4d. We can thus understand the probability distribution as being a manifestation of the characteristics of the underlying trajectories. In the confined circular geometry, the pilot-wave dynamics tends to drive the walker along circular orbits with radii corresponding to maxima of the cavity mode amplitude. Instead of being trapped on these orbits as in the low-path-memory limit (figure 3-1c), the walker wobbles around them and drifts between them; nevertheless, these unstable orbits leave their mark on the probability distribution.

We have examined the hydrodynamic analogue of a quantum particle in a circular domain, demonstrating the emergence of a coherent statistical behavior in the long-memory limit. Our results indicate that the statistical behavior is rooted in the wave-induced spatial dependence of the walking speed, and the tendency for the walker to trace out the unstable orbital states of the cavity. The experiments reported

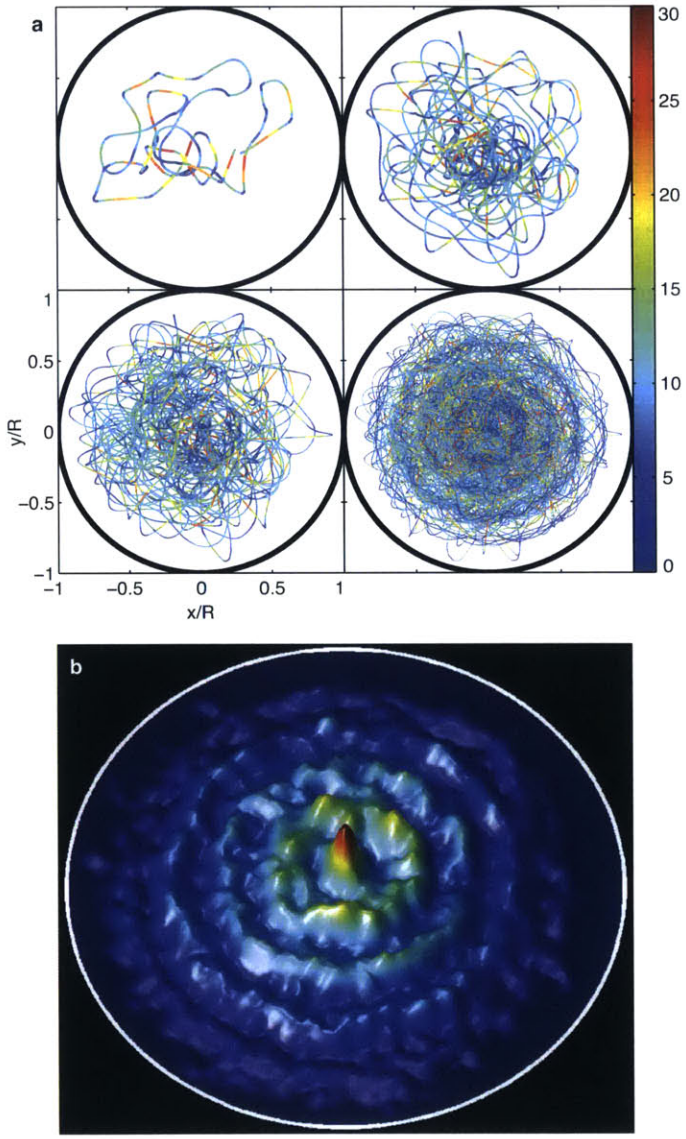

Figure 3-3: (a) Trajectories of a droplet of diameter D = 0.67 mm walking in a circular corral with radius R = 14.3 mm and depth h_0 = 6.6 mm, driven at f = 70 Hz, for which γ_F = 3.7. Trajectories of increasing length in the long path-memory limit (γ/γ_F = 0.989) are color-coded according to droplet speed (mm/s). (b) The probability distribution of the walking droplet's position.

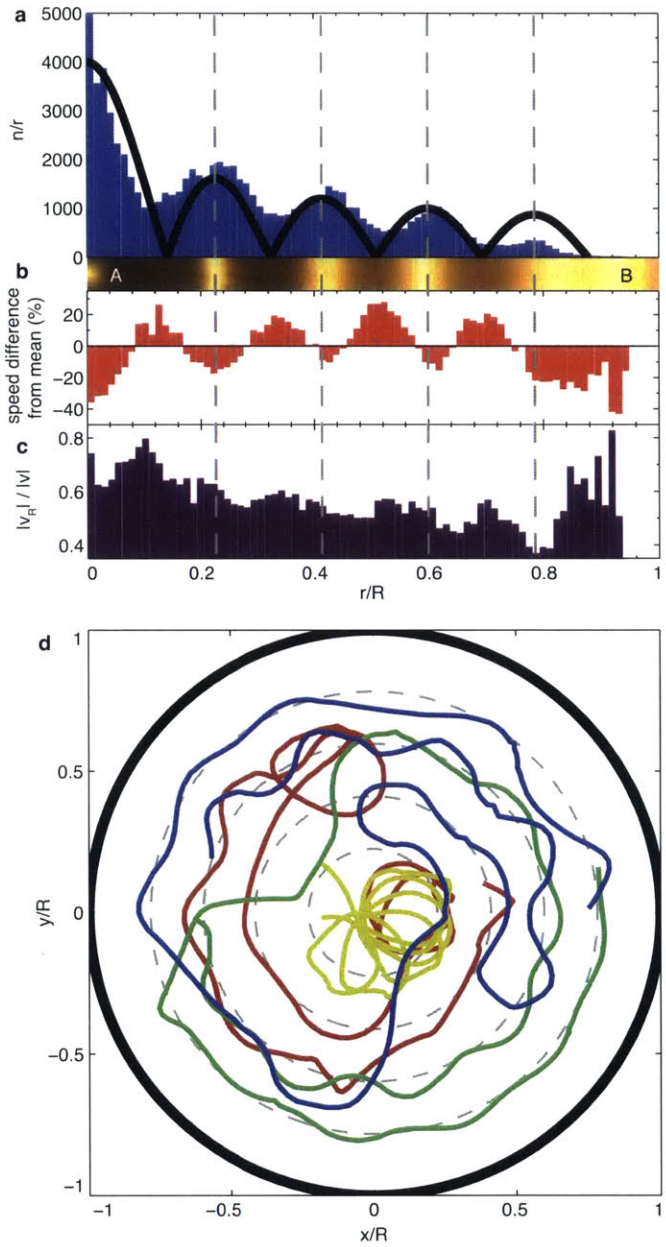

Figure 3-4: (a) Histogram of radial position, (b) velocity variation from the mean ($|\bar{v}|$ = 8.66 mm/s) and (c) radial dependence of the normalized radial velocity ($|v_R|/|v|$). In a), the minima in the probability amplitude approximately correspond to maxima in the walker velocity, maxima in the normalized radial velocity, and zeros in the amplitude of the fundamental cavity mode (upper curve). The section A-B represents a radial slice of the cavity's Faraday mode, with bright bands indicating local extrema. Averaging windows and bin widths are fixed at $0.012R$. In (c), values of 1 and 0 correspond to purely radial and azimuthal motion, respectively. (d) Four sample trajectories extracted from the complete trajectory indicate a tendency to orbital motion along particular radii. Different colors serve only to demarcate different trajectories. In all plots, the dashed lines represent maxima in the amplitude of the fundamental cavity mode.

herein indicate that in the long-memory limit, walkers in confined geometries, like quantum particles, have a coherent statistical behavior that may be characterized by a linear wave theory. Whether or not the statistical description provided by quantum mechanics represents a complete description of physical reality was the subject of the celebrated debate between Einstein [48] and Bohr [11]. Whatever the case may be in quantum mechanics, the linear statistics is clearly an incomplete description of our fluid system, and is underlaid by a complex, nonlinear, pilot-wave dynamics.

It is interesting to consider our results in light of quantum corral experiments, in which electrons are confined to a corral composed of iron adatoms on the surface of a copper substrate [27, 26, 51]. We note that the spacing between the adatoms results in considerable energy loss, as do the shallows surrounding our fluid corrals. The electron density in the quantum corral was measured with a scanning-electron microscope, and found to have a wave-like pattern with the de Broglie wavelength of the trapped electrons, λ_{dB}. The probability distribution presented in figure 3-3b is thus analogous to that in the circular quantum corral, with λ_F playing the role of λ_{dB}.

In our fluid system, we are able to observe not only an analogous statistical wave (figure 3-3b), but a real physical wave that guides the droplet (figure 3-2). While in unbounded geometries the pilot-wave field assumes a relatively simple form [42] and gives rise to rectilinear motion, in the corral geometry, its form is affected by reflections off the boundaries, and the resulting walker motion is irregular, with the degree of irregularity increasing with path memory. As was the case in the study of single-particle diffraction [22], in the long-path-memory limit, the statistical wave function is prescribed by the wavelength of the pilot wave and the system geometry. We note that similar results arise for a walker confined to walk along a line in a narrow rectangular geometry, where the wavelength of the probability distribution is again prescribed by that of the guiding wave. A discussion of the results obtained in this geometry will be presented elsewhere.

Our study indicates that this hydrodynamic system is closely related to the physical picture of quantum dynamics envisaged by de Broglie, in which rapid oscillations

originating in the particle give rise to a guiding wave field [31, 32]. The pilot-wave theories of de Broglie and Bohm [10] are often conflated [67]; however, it is valuable to distinguish between them here for the sake of comparison with our system. According to Bohm, the particle is guided by its statistical wave, its velocity being equivalent to the quantum velocity of probability. According to de Broglie's double-wave solution [31], the particle is guided by a real wave (of unspecified origins) in such a way as to execute a dynamics whose statistics is described by standard quantum theory. Figure 3-2a indicates the instantaneous surface wave field responsible for piloting the walker, whose complex form results in a complex trajectory. Figure 3-3b represents the relatively simple statistical wave field describing the probability distribution, whose form is prescribed by the eigenmode of the cavity. The simple form of the statistical wave conceals the complex underlying pilot-wave dynamics.

3.2 Linear corral

Figure 3-5a illustrates the trajectory of a walker confined within the rectangular cavity, again color-coded according to speed in the long-memory limit. Here, the walker tends to follow a relatively straight trajectory along the central axis of the rectangle. In restricting the walker's domain to a finite length, we induce fluctuations in walker speed that are strongly correlated with the walker's position. As in the circular corral, the periodic fluctuations in the walker's probability distribution (figure 3-5b) can be rationalized in terms of the wave-induced spatial dependence of the walking speed (figure 3-5c). The cavity mode for our driving frequency is shown in figure 3-5d. We observe that, as was the case in the circular corral, the wavelength of the probability distribution is approximately half the Faraday wavelength. We note, however, that in this rectangular geometry, the wavelength of the probability distribution increases with the average walker speed.

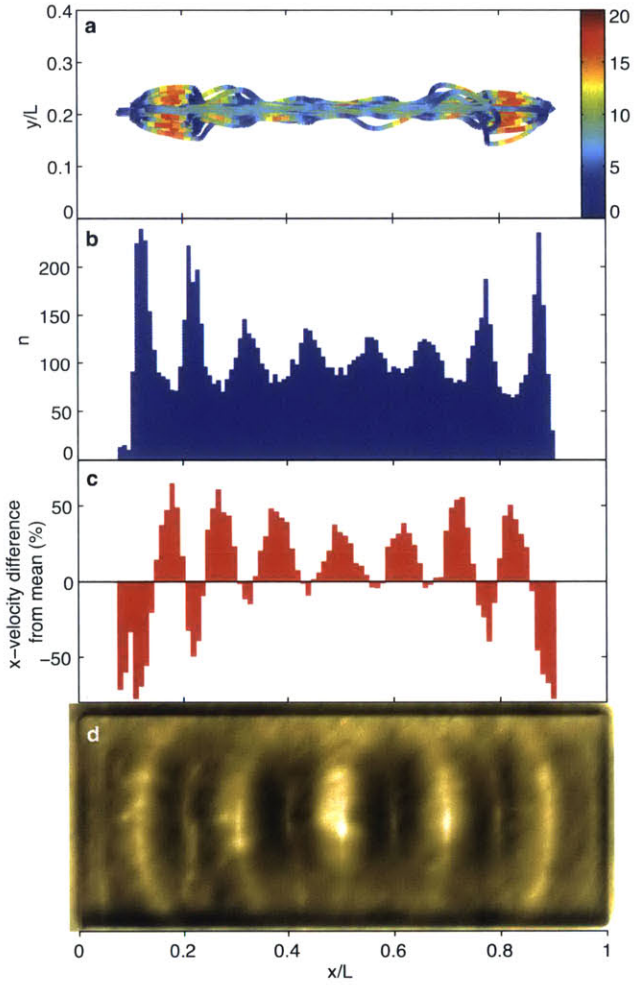

Figure 3-5: (a) Trajectories of a droplet of diameter D = 0.70 mm walking in a rectangular geometry, colour-coded according to droplet speed (mm/s). The corral is of length L = 26.4 mm, width w = 10.5 mm and depth h_0 = 6.6 mm, and is being driven at f = 74 Hz with γ/γ_F = 0.987 and γ_F = 4.0. (b) Histogram of longitudinal position. (c) Longitudinal velocity variation from the mean ($\bar{v}$ = 6.93 mm/s). (d) The Faraday mode in the rectangular corral at f = 74 Hz.

Chapter 4

Walking in a rotating frame

The motion of droplets walking on a rotating bath was first considered by Fort *et al.* [52]. One expects an object moving with constant speed u_0 in a rotating frame to follow circular orbits with a radius that varies continuously with the imposed rotation rate. Specifically, balancing the radially inwards Coriolis force $F_\Omega = 2m\Omega u_0$ and the inertial force $F_c = mu_0^2/r_0$ indicates an inertial orbit with radius $r_0 = u_0/2\Omega$ and frequency $\omega = u_0/r_0 = -2\Omega$. In what follows, we shall refer to an inertial orbit as a circular orbit in which the Coriolis and inertial forces balance. Fort *et al.* [52] demonstrated that, at low memory, the orbital radius of the walker indeed varies continuously with the rotation rate. However, at high memory, only discrete bands of possible orbital radii exist, the spacing between them being roughly equal to half the Faraday wavelength. They demonstrated that the observed orbital quantization results from the droplet's interaction with its own wave field. While they documented the transition from continuous to discrete orbits, they did not examine the system behavior in the high memory limit, where as we shall see here, the orbits become unstable. Moreover, they did not report the precise amplitudes of the vibrational forcing used, making quantitative comparison to the present study or our group's associated theoretical developments [84] impossible. As we shall see in what follows, the system behavior is extremely sensitive to the forcing amplitude in the long memory limit.

Owing to the analogous form of the Coriolis force acting on a mass in a rotating

frame and the Lorentz force acting on a charge in the presence of a uniform magnetic field, [52] were able to draw an analogy between their quantized orbits and Landau levels, with the Faraday wavelength playing the role of the de Broglie wavelength. Eddi *et al.* [45] demonstrated that the distance between a pair of orbiting walkers is likewise quantized, but can be modulated by rotating the bath. Specifically, the orbital radius increases or decreases continuously with the rotation rate, according to whether the orbiting pair is co- or counter-rotating relative to the bath. The same Coriolis-Lorentz analogy suggests that this orbital level splitting is analogous to the Zeeman effect whereby spectral lines are split in the presence of a magnetic field [45].

The present work builds upon the work of Fort *et al.* [52], but focuses on the system behavior in the high memory limit.

4.1 Experiments

We present the results of an experimental investigation of a droplet walking on the surface of a vibrating rotating fluid bath. Particular attention is given to demonstrating that the stable quantized orbits reported by Fort *et al.* [52] arise only for a finite range of vibrational forcing, above which complex trajectories with multimodal statistics arise. We first present a detailed characterization of the emergence of orbital quantization, and then examine the system behavior at higher driving amplitudes. As the vibrational forcing is increased progressively, stable circular orbits are succeeded by wobbling orbits with, in turn, stationary and drifting orbital centers. Subsequently, there is a transition to wobble-and-leap dynamics, in which wobbling of increasing amplitude about a stationary center is punctuated by the orbital center leaping approximately half a Faraday wavelength. Finally, in the limit of high vibrational forcing, irregular trajectories emerge, characterized by a multimodal probability distribution that reflects the persistent dynamic influence of the unstable

This section appears as published in: D. M. Harris and J. W. M. Bush. Droplets walking in a rotating frame: from quantized orbits to multimodal statistics. *Journal of Fluid Mechanics*, 739: 444-464, 2014 [61].

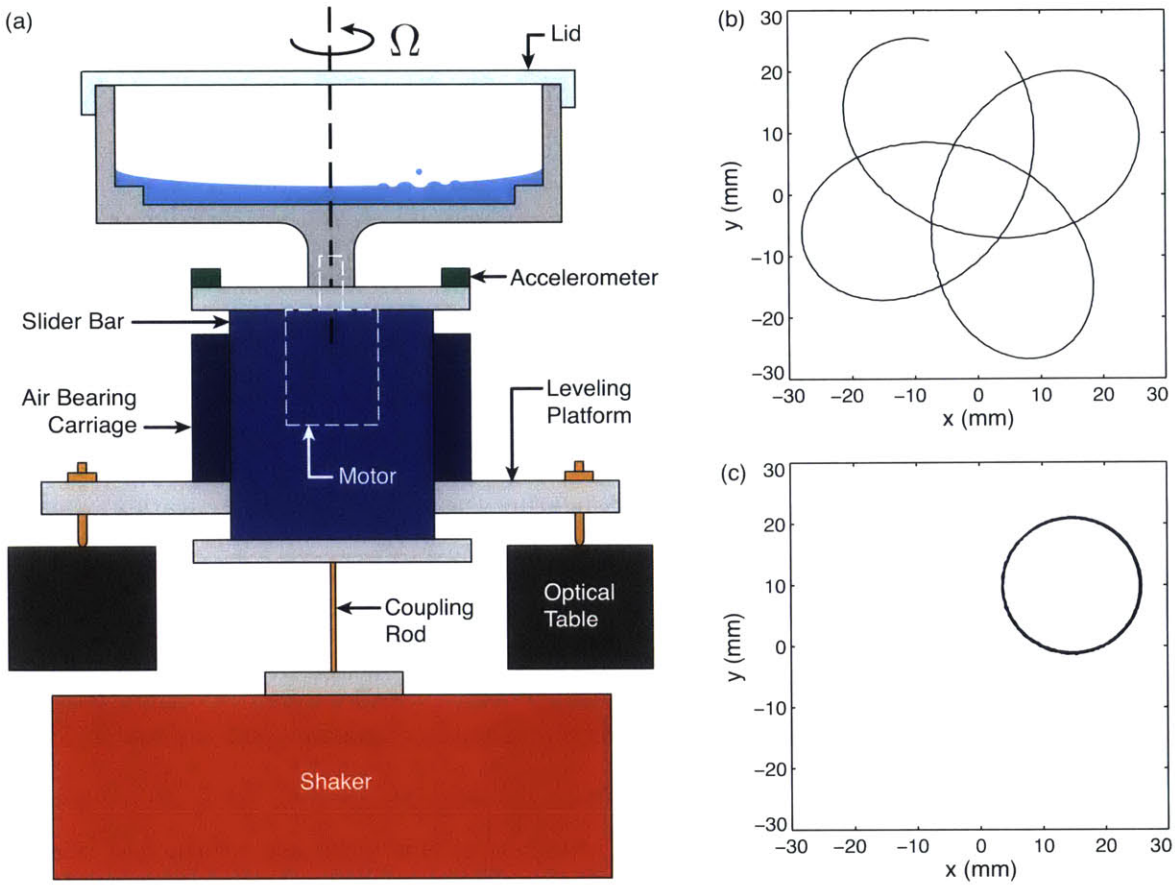

Figure 4-1: (a) Schematic of the experimental setup. An electromagnetic shaker drives a rotating fluid tray, interfaced by a thin coupling rod and linear air bearing. The shaker is mounted to a massive leveling platform (not shown). (b) Sample trajectory of a walker in the lab frame of reference with $\gamma/\gamma_F = 0.822 \pm 0.006$, $u_0 = 9.0$ mm/s, and $\Omega = 0.61$ rad/s. (c) Same trajectory in the rotating frame of reference. The origin ($x = 0$, $y = 0$) in plots (b) and (c) represents the bath's center of rotation.

orbital states. In the corral experiments, the wavelike probability distribution assumes a multimodal form, with the spacing of the peaks defined by the wavelength of the guiding wavefield. Here, we will discuss a further experimental configuration in which multimodal statistics emerge from walker dynamics in the high memory limit.

4.1.1 Methods

A schematic of the experimental setup is shown in figure 4-1(a). For the present experiments, we use a circular tray of inner diameter 146 mm and depth 38 mm filled to a depth of $H = 7.0$ mm with a silicone oil of density $\rho = 950$ kg/m^3, surface tension

σ = 0.0206 N/m, and kinematic viscosity $\nu = 20.9 \pm 0.1$ cS. The viscosity is highly sensitive to temperature and is estimated using fluid temperature measurements, made with an infrared thermometer, and an empirical relationship between temperature and viscosity provided by the oil manufacturer (Clearco). A shallow border of depth 1.0 mm and width 9.5 mm surrounds the deeper central part of the fluid bath which avoids complications that would otherwise arise from the meniscus at the tray's outer wall, a technique that has been employed in investigations of walking droplets [44, 64]. The fluid tray is vibrated sinusoidally at frequency f = 80 Hz with an acceleration amplitude γ. Above a critical acceleration amplitude γ_F, standing Faraday waves spontaneously form with frequency $f/2$ and wavelength λ_F = 4.75 mm. The Faraday threshold γ_F is measured to be 4.08 ± 0.07 g with the variation resulting from the high sensitivity of the Faraday threshold to temperature (here approximately 0.08 g/°C), as arises through the temperature dependence of surface tension and viscosity. The Faraday threshold and temperature were measured and recorded at the beginning and end of each experiment. All experiments reported in this work are conducted below the Faraday threshold; thus, in the absence of a droplet, the bath would remain flat.

In addition to continuously vibrating the fluid tray, we rotate the tray about a vertical axis with angular rate Ω using a stepper motor (Mercury Motors, SM-42BYG011) mounted in the vibrating frame, whose speed and sense are specifiable via software. The rotation rate Ω is varied from 0 to 5.5 rad/s in the current experiments. At the maximum rotation rate considered, the fluid surface assumes a parabolic shape with minimum depth at the center of the tray of 2.9 mm. Nevertheless, the Faraday and walking thresholds remain nearly unchanged, provided the depth exceeds 2.5 mm [44]. We also note that the radially outward centrifugal force resulting from the system rotation is precisely balanced by the inward interfacial force imparted during impact on the parabolic bath surface, so that a stationary bouncing droplet will remain stationary in the rotating frame [52, 84]. Our two principal control parameters are thus the relative forcing acceleration amplitude γ/γ_F and the rotation rate of the bath Ω.

We create droplets of radius R_d = 0.40–0.43 mm by rapidly extracting a submerged

needle from the fluid bath [91]. A transparent lid is placed on the tray to avoid the effects of ambient air currents. We then measure the walking speed u_0 of the droplet in the absence of rotation, which is found to be between 9.5 and 12.6 mm/s. The vertical motion of the walkers used in this study is completely period doubled and corresponds to the $(2,1)^2$ walking mode [82, 105]. Rotation is then applied and before data is collected, we wait at least one minute, which significantly exceeds both the spin-up time of the fluid ($h_0^2/\nu \sim 2.5$ s) and the characteristic decay time of the walker's wave field ($T_F M_e < 4$ s). The walker's motion is filmed from above at 20 frames per second by a CCD camera (AVT, Manta G-125) that has been leveled and aligned with the rotation axis of the tray. The trajectory of the walker in the laboratory frame is then determined using particle tracking software. In order to minimize spurious boundary effects, if the walker passed within $5.5\lambda_F$ (26.1 mm) of the submerged barrier, the data was discarded. Within this distance, the trajectory was noticeably influenced by the boundary at high memory; otherwise, the walker's motion and statistical behavior were independent of its proximity to the boundary. A marker on the outer edge of the tray is also tracked, allowing for determination of the angle of the tray in each image, and for the transformation of the trajectory into the rotating frame. An example of a walker trajectory in the lab frame is given in figure 4-1(b) with the corresponding trajectory in the rotating frame in figure 4-1(c).

We use an adaptive osculating circle technique to compute the local radius of curvature of the trajectory in the rotating frame. We denote the ith point along the trajectory as p_i. At each point p_i, we first connect that point with a straight line to its nearest neighbors p_{i-1} and p_{i+1}. We then compute the interior angle between segments, $\angle p_{i-1}p_ip_{i+1} = \theta_{i,1}$. Note that in the continuous limit, each of the segments approaches the local tangent line, so that $\theta_{i,1}$ approaches π. Next, we proceed to calculate the interior angle between segments $p_{i-2}p_i$ and p_ip_{i+2} which we define as $\theta_{i,2}$. We repeat this procedure by incrementally increasing the value of the second index until we find a $k = k_c$ such that $\pi - \theta_{i,k} > \alpha$, where α is some critical angle that we specify. We then fit a circle to the points $\{p_{i-k_c}, p_i, p_{i+k_c}\}$, and define the radius of this circle $r_{i,k}$, to be an approximation of the local radius of curvature at point p_i.

Additionally, we set a minimum value $k_c \geq 2$, which provides good resistance to noise for our data. In some sense this method is "adaptive" in that in general, k_c will be larger for regions of small curvature and smaller for regions of high curvature. We find that this adaptive osculating circle method provides a reasonable noise-resistant algorithm for calculating the radii of curvature in our experiments.

Orbital radii and the local radius of curvature are calculated using this method, with $\alpha = \pi/4$ for data presented in figures 4-3 to 4-8 and $\alpha = \pi/2$ for figures 4-9 to 4-11. Unless otherwise noted, error bars represent plus and minus one standard deviation of the measured quantity of interest.

4.1.2 The emergence of quantization

How does memory, specifically the proximity to the Faraday threshold, influence the dynamics of a walker in a rotating frame? Sample wave fields corresponding to an identical walker with increasing memory are shown in figures 5-4(a)-(d). At low memory (figure 5-4(a)) the wave field is nearly centered on the droplet, prescribed primarily by its most recent impact. As the memory is increased (figure 5-4(b)), the wave field is more persistent; consequently, in executing a circular orbit, the droplet interacts with its own wake. There is thus an influence of the walker's previous orbit on its present dynamics. At very high memory, as in figure 5-4(c) and (d), the wave field is considerably more complex, the form of which both reflects and perpetuates an irregular trajectory. The images in figures 5-4(c) and (d) are taken from a single experiment at very high memory, where the wave field is continuously evolving. In figures 5-4(a)-(c), note that the lateral extent of the wave field increases with memory. We proceed by considering walkers following regular circular trajectories.

In figure 4-3 we report the observed dependence of the orbital radii r_0 on the rotation rate Ω at four different values of memory. At low memory, we find that all orbital radii are accessible, and that the orbital radius r_0 decreases continuously and monotonically with increasing rotation rate Ω (figure 4-3(a)). As was reported by Fort *et al.* [52], there is an offset from the standard prediction for inertial orbits so

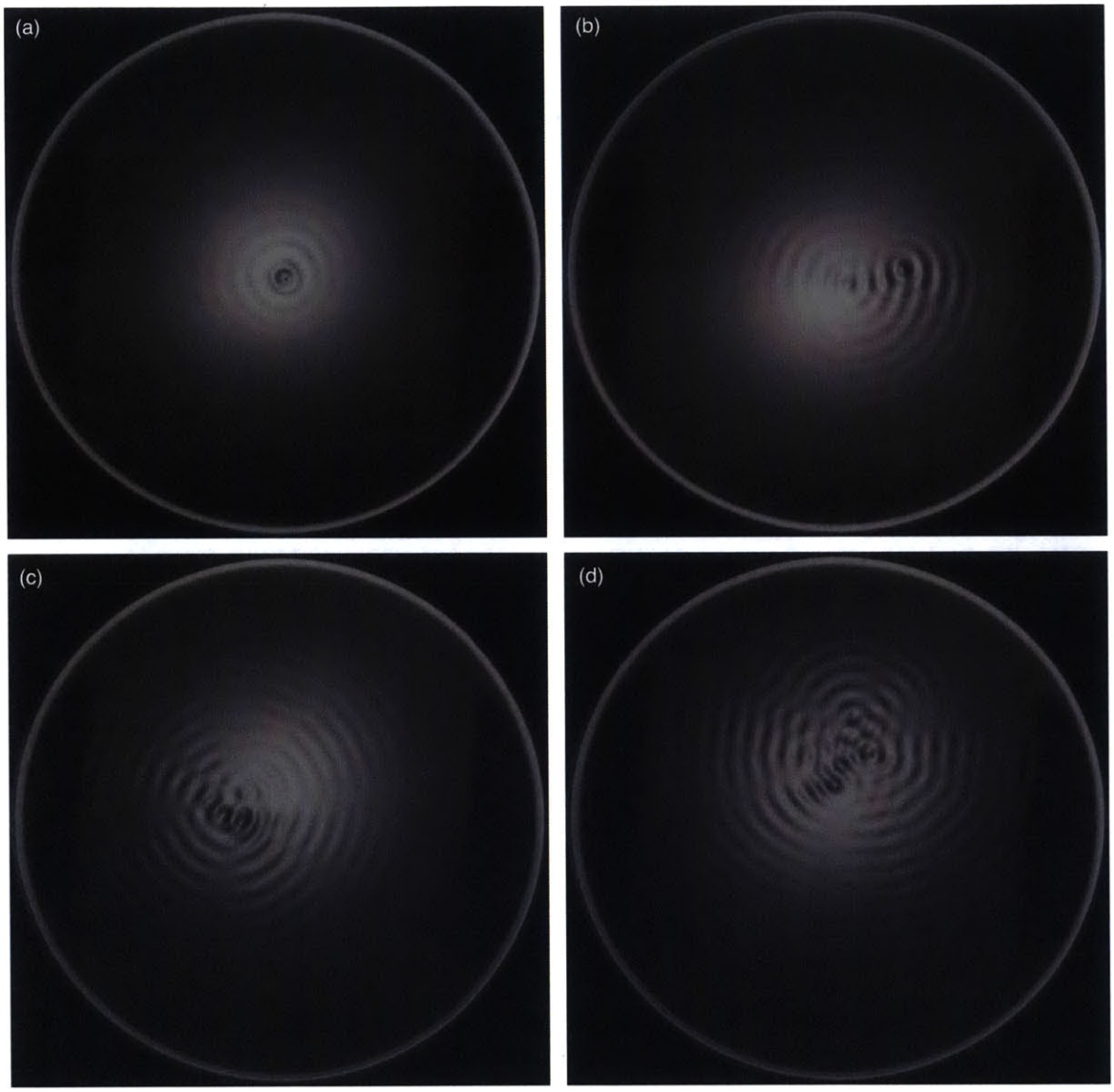

Figure 4-2: Wave fields generated by a walking droplet of radius R_d = 0.4 mm in a rotating frame (Ω = 0.79 rad/s) as the driving acceleration is increased: (a) γ/γ_F = 0.862 ± 0.006, (b) $\gamma/\gamma_F = 0.968 \pm 0.006$, (c) $\gamma/\gamma_F = 0.984 \pm 0.006$, (d) same conditions as (c), image taken 10.1 seconds later.

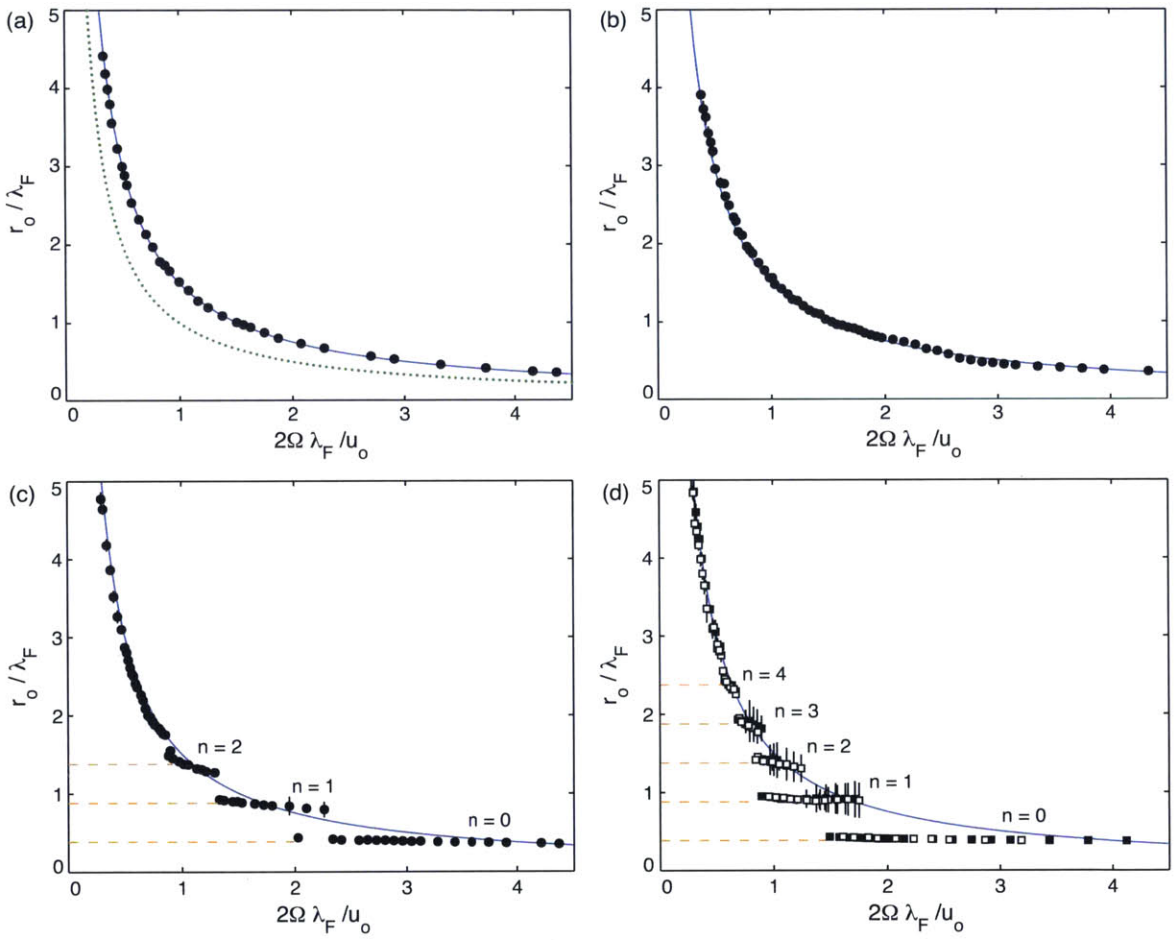

Figure 4-3: The observed dependence of the orbital radius r_0 on the rotation rate of the bath Ω. (a) $\gamma/\gamma_F = 0.822 \pm 0.006$ with $u_0 = 9.0$ mm/s, (b) $\gamma/\gamma_F = 0.922 \pm 0.004$ with $u_0 = 9.5$ mm/s, (c) $\gamma/\gamma_F = 0.954 \pm 0.006$ with $u_0 = 12.0$ mm/s, (d) $\gamma/\gamma_F = 0.971 \pm 0.004$ with $u_0 = 10.9$ mm/s (■) and 11.7 mm/s (□). The dotted line in (a) represents the standard prediction for inertial orbits, $r_0 = u_0/2\Omega$, while the solid line represents the modified relationship, $r_0 = au_0/2\Omega$, with a best fit value $a = 1.51$. The solid line is identical in all four panels and is shown for the sake of comparison with the low memory result. The horizontal dashed lines in (c)-(d) are the zeros of $J_0(k_F r)$, which correspond closely to the radii of the observed quantized orbital levels [84].

that

$$r_0 = a\frac{u_0}{2\Omega}. \tag{4.1}$$

The data in figure 4-3(a) is best fit with an offset value of $a = 1.51$, shown in the plot as a solid line, indicating that the orbits are larger than expected. This is consistent with the results of Fort *et al.* [52], who reported $1.2 \leq a \leq 1.5$ for all oil and forcing frequency combinations considered. This offset results from an outward radial wave force due to the influence of the waves generated by the most recent impacts. The dependence of the magnitude of this offset on the system parameters is rationalized in our theoretical treatment of the problem [84]. As the driving is increased further (figure 4-3(b)), a subtle deviation from the low-memory result begins to emerge at small radius (near $r_0/\lambda_F \approx 0.6$), although the curve remains continuous and all radii accessible. More dramatic changes are apparent at the next value of memory considered (figure 4-3(c)), where the curve is no longer continuous, and several bands of radii become inaccessible. This leads to the emergence of three discrete orbital levels, $n = 0$, 1, and 2. Moreover, there is an orbital degeneracy: multiple radii are possible for a given rotation rate. Increasing the memory further (figure 4-3(d)) results in the emergence of additional quantized levels and heightened orbital degeneracy. The quantized radii are centered on the zeros of $J_0(k_F r)$ (represented by the dashed horizontal lines), which are nearly half multiples of the Faraday wavelength, a result rationalized in our theoretical treatment of the problem [84].

From the results in figure 4-3, a clear picture of the origins of orbital quantization has now emerged. As the memory is increased the first variance from the low-memory result arises at the smallest radii, with the deviations propagating progressively upwards along the curve as the memory is increased. This progression is consistent with an intuitive understanding of the role of path memory. The smallest orbits have the smallest orbital period; thus, the walker's wake will have decayed the least after a single orbit. Consequently, walkers in the tightest orbits, as arise at higher rotation rates, will be most strongly affected by their past. The observed quantization is thus a direct result of memory. It also follows that for sufficiently large orbits at

any memory, the data should revert to the low-memory curve. This is precisely what is observed in our experiments; the data falls along the low memory curve beyond the highest quantized level observed (figures 4-3(c)-(d)). For large orbits, the orbital period is much greater than the characteristic decay time of the Faraday waves; thus, the walker's prior orbits do not influence its dynamics.

Another quantity readily measured is the walker's orbital frequency $\omega = u/r_0$. For standard inertial orbits, we recall $\omega = -2\Omega$. Assuming that the walker maintains a speed close to its free speed ($u \approx u_0$), we can rearrange the low memory result (4.1) to find

$$\omega = -\frac{2\Omega}{a}. \tag{4.2}$$

We note that the walking speed in orbit u differs slightly from its free speed u_0 by no more than 6% at the lowest memory considered ($\gamma/\gamma_F = 0.822$) and no more than 12% at the highest memory considered here ($\gamma/\gamma_F = 0.971$). Consequently, equation (4.2) should still provide a reasonable description of the orbital frequencies at low memory. In our experiments, we measure the speed and orbital radius from which we calculate the orbital frequency $\omega = u/r_0$. The dependence of the orbital frequency on rotation rate is presented in figure 4-4, each panel of which corresponds to its counterpart in figure 4-3. At low memory (figure 4-4(a)), the data follows a line well described by (4.2) using $a = 1.51$ as determined previously. The orbital frequencies are thus less than those expected for standard inertial orbits. At higher memory (figure 4-4(b)), the deviation from the low-memory result becomes apparent at high rotation rates (i.e. for small radii). A significant difference is apparent in figures 4-4(c) and 4-4(d), where the curves are no longer continuous, but discrete bands of possible orbital frequencies emerge. The quantization in orbital frequency is a consequence of that in orbital radius. We note that in all cases, for sufficiently low frequencies (large orbital radii), the data closely follows the linear relationship expected at low memory.

From what we have seen thus far, one might anticipate the emergence of further quantized levels at higher memory. We shall proceed by demonstrating that, conversely, the circular orbits become unstable at high memory. The increased size of

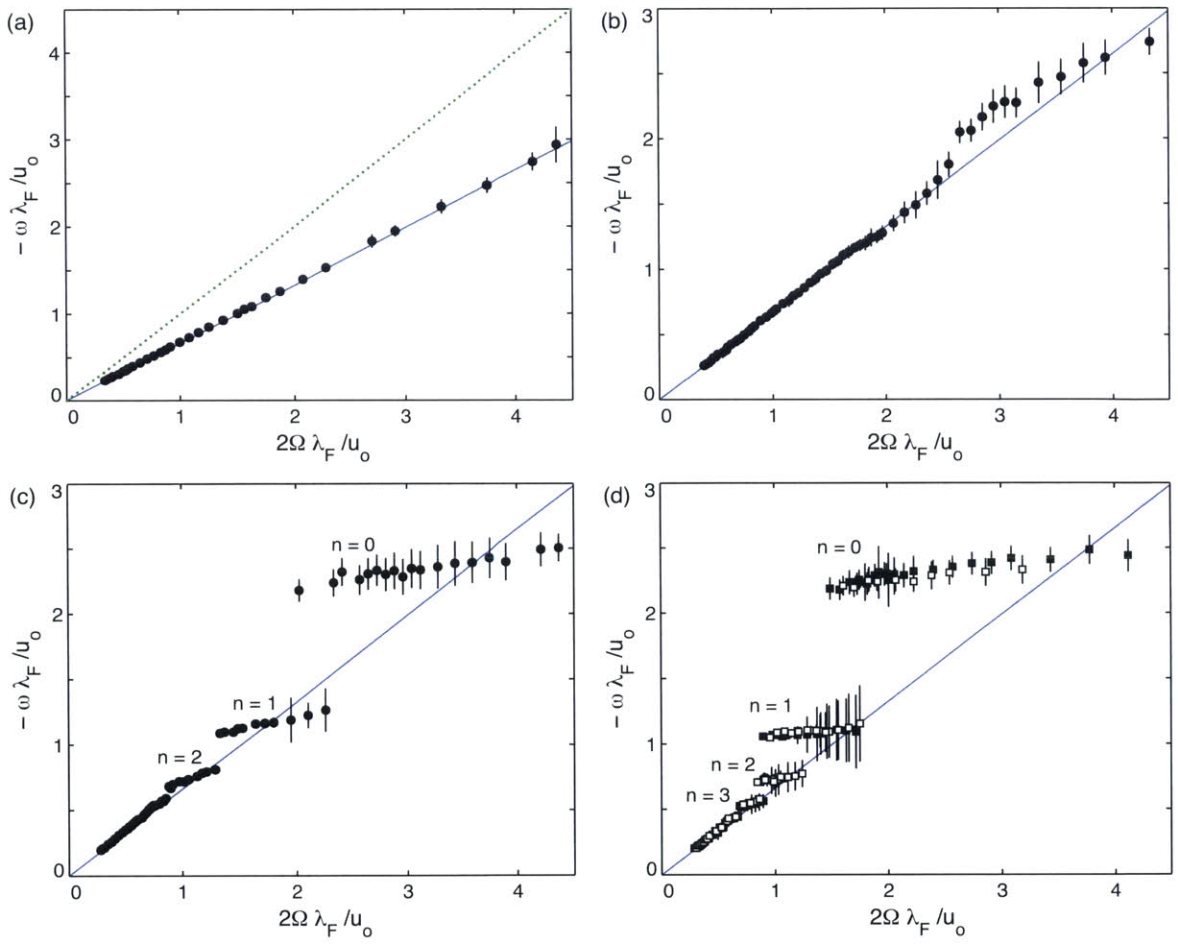

Figure 4-4: The observed dependence of the orbital frequency ω on the rotation rate of the bath Ω. (a) $\gamma/\gamma_F = 0.822 \pm 0.006$ with $u_0 = 9.0$ mm/s, (b) $\gamma/\gamma_F = 0.922 \pm 0.004$ with $u_0 = 9.5$ mm/s, (c) $\gamma/\gamma_F = 0.954 \pm 0.006$ with $u_0 = 12.0$ mm/s, (d) $\gamma/\gamma_F = 0.971 \pm 0.004$ with $u_0 = 10.9$ mm/s (■) and 11.7 mm/s (□). The dotted line in (a) represents the standard prediction for inertial orbits, $\omega = -2\Omega$, while the solid line (plotted in each panel) represents the modified relationship suggested by equation (4.2), $\omega = -2\Omega/a$, with $a = 1.51$.

the error bars at levels n = 1, 2, and 3 in figure 4-3(d) does not reflect an increased experimental error, but rather oscillations in the orbital radius, as arise for 'wobbling' orbits. This effect was not reported by Fort *et al.* [52], presumably due to lower forcing amplitudes considered in their study.

4.1.3 Wobbling orbits

We now turn our attention to wobbling orbits, as are characterized by an oscillation in both the radius and the radius of curvature R along the trajectory. We note that the possibility of wobbling orbits was originally suggested by the linear stability analysis in our theoretical treatment of the problem [84]. We will focus on wobbling orbits at the n = 1 orbital level, as a preliminary exploration suggested that they occur over the largest range of control parameters. We adopt the following procedure. At a fixed forcing amplitude ($\gamma/\gamma_F > 0.96$) we first increase the rotation rate gradually from zero until the walker enters the n = 1 orbital level, whose radius is near the second zero of $J_0(k_F r)$. The transition is marked by a sharp inward jump from the n = 2 orbital. We then increase the rotation rate in a stepwise manner, recording a 150 second trajectory at each rotation rate after waiting at least four minutes following each change. This process is repeated until the walker exits the n = 1 orbital by dropping down to the innermost n = 0 orbital.

Simple wobbling orbits

In figure 4-5, we characterize the n = 1 orbital level at a forcing amplitude γ/γ_F = 0.961. In figure 4-5(a), the dependence of the mean radius of curvature on the rotation rate is shown, with error bars reflecting the observed variation. For $2\Omega\lambda_F/u_0 < 1.7$, we observe stable circular orbits. However, as the rotation rate is increased through the range $1.7 < 2\Omega\lambda_F/u_0 < 2.2$, considerable growth and then decay in the variation of the radius of curvature is apparent. As evidenced by the trajectory in figure 4-5(b), this region of heightened variation is marked by nearly elliptical orbits. Plotting a sample time trace of the radius of curvature in figure 4-5(c) indicates a distinctive

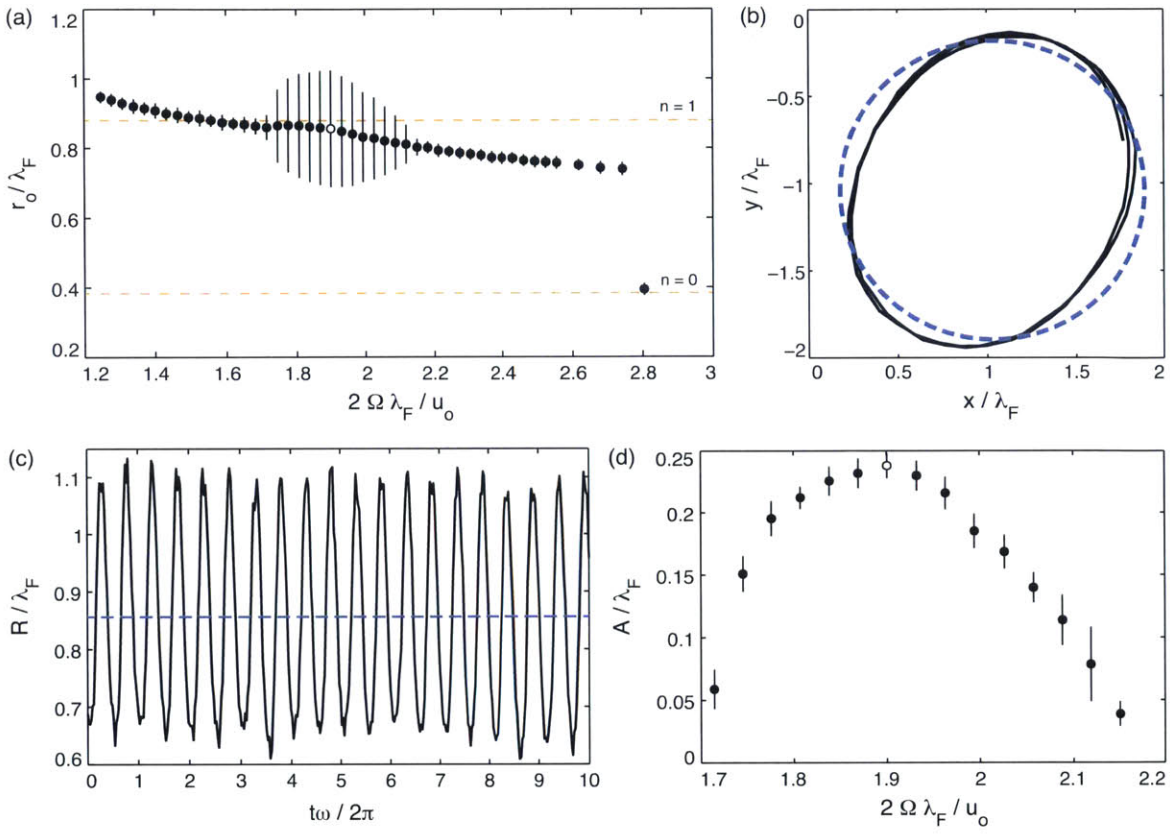

Figure 4-5: (a) Evolution of the observed mean radius of curvature r_0 of the $n = 1$ orbital as a function of rotation rate ($\gamma/\gamma_F = 0.961 \pm 0.002$, $u_0 = 12.0$ mm/s). The error bars extending from each point represent the average deviation from the mean observed radius over the course of a 150 second experiment at fixed Ω. The horizontal dashed lines represent the first two zeros of $J_0(k_F r)$ corresponding to the innermost orbital levels ($n = 0, 1$). The empty marker ($\bigcirc$) denotes the location of largest observed fluctuations in the radius of curvature. (b) A 5 second sample of the trajectory (solid curve) at the point of largest amplitude fluctuations, shown with a circle of equivalent mean radius (dashed). (c) Time trace of the instantaneous radius of curvature as it oscillates about a mean radius $R/\lambda_F = 0.86$. (d) Amplitude of wobbling motion (A/λ_F) as a function of the rotation rate (Ω) for the wobbling states apparent in part (a).

periodic oscillation. Note that this oscillation has approximately twice the frequency of the orbit ($\tilde{\omega} \approx 2\omega$), as is consistent with the nearly elliptical form of the trajectory. We will refer to these periodic orbits that wobble about a stationary orbital center as 'simple' wobbling orbits. For the time trace of each wobbling orbit identified in figure 4-5(a), we report the amplitude of the wobbling in figure 4-5(d), where error bars indicate the minimal variation in this wobbling amplitude at fixed Ω. At this forcing amplitude, a finite window of simple wobbling orbits exists at the $n = 1$ level, each with frequency of approximately 2ω.

What happens at even higher forcing amplitude? The dependence of wobbling amplitude on rotation rate at four different forcing amplitudes γ/γ_F is presented in figure 4-6(a). First we note that the onset of wobbling shifts to lower rotation rates as the forcing amplitude is increased. Second, at higher memory, the trajectories do not return to circular orbits before jumping down to the innermost $n = 0$ mode as Ω is increased. Third, the error bars on the wobbling amplitudes generally increase with memory, reflecting larger fluctuations in the wobbling amplitude. These variations are typically associated with a drifting of the orbital center, as will be discussed further in what follows.

We proceed by examining the wobbling frequency $\tilde{\omega}$ more closely. While the wobbling arose near a frequency of 2ω in all cases, there is a weak dependence on Ω. In figure 4-6(b), we plot the wobbling frequency as a function of the rotation rate Ω. Here we find a rather surprising result. The data nearly follows a single curve, independent of memory, with the relative wobbling frequency $\tilde{\omega}/\omega$ decreasing monotonically with Ω, a result rationalized by Oza *et al.* [86]. While a trend within a single data set might be expected, the overall collapse to a single curve is striking, indicating that the the wobbling frequency is prescribed by the rotation rate of the bath and relatively insensitive to the forcing amplitude. We note that wobbling orbits, each with wobbling frequency $\tilde{\omega} \approx 2\omega$, were also observed in the $n = 2$, 3, and 4 orbitals.

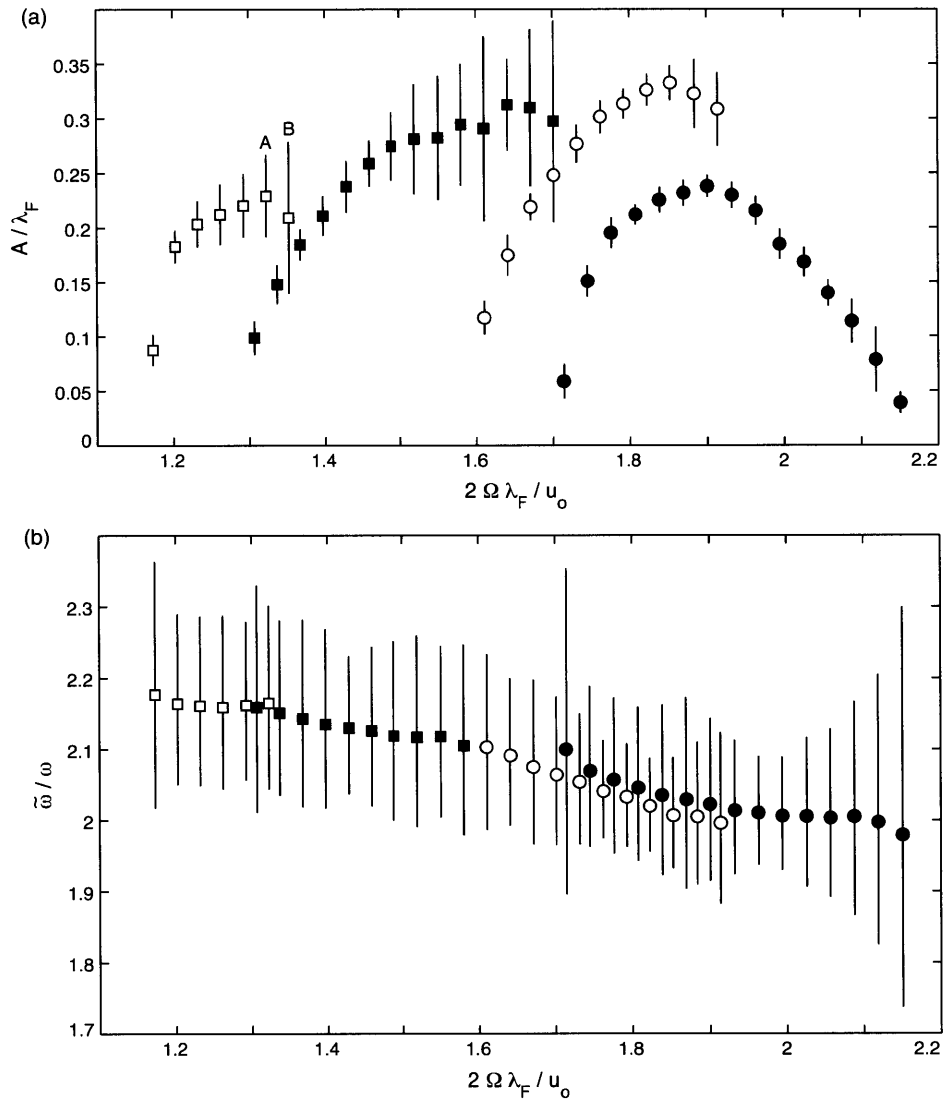

Figure 4-6: (a) The dependence of the wobbling amplitude A and (b) the wobbling frequency $\tilde{\omega}$ on the rotation rate of the bath Ω, for four different values of memory: $\gamma/\gamma_F = 0.978 \pm 0.003$ with $u_0 = 12.4$ mm/s (□), $\gamma/\gamma_F = 0.974 \pm 0.002$ with $u_0 = 12.3$ mm/s (■), $\gamma/\gamma_F = 0.969 \pm 0.005$ with $u_0 = 12.3$ mm/s (○), and $\gamma/\gamma_F = 0.961 \pm 0.002$ with $u_0 = 12.0$ mm/s (●, same as figure 4-5). Each point corresponds to a single 150 second experiment (3000 position measurements) with fixed parameters. The trajectories at the points labeled A and B in (a) are considered in figures 4-7 and 4-8, respectively.

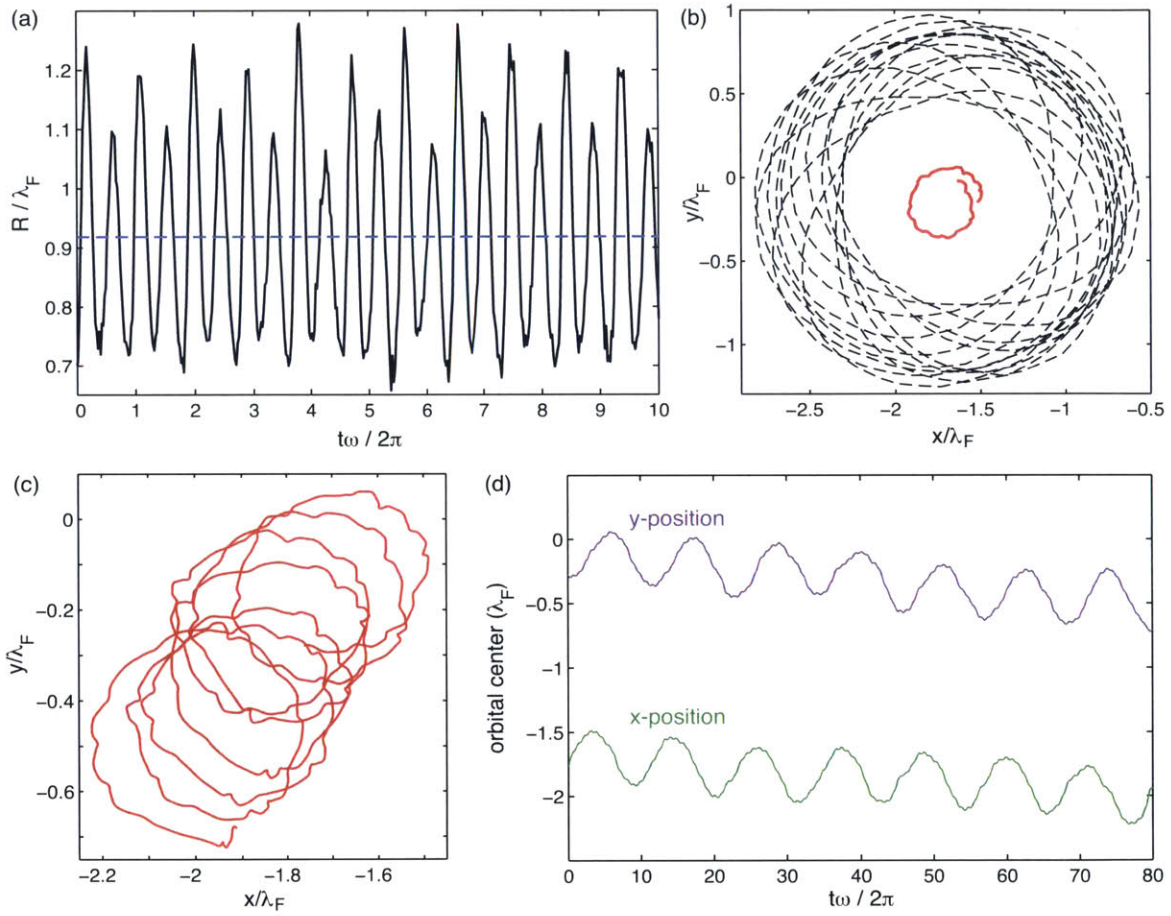

Figure 4-7: Drifting wobbling orbits observed for $\gamma/\gamma_F = 0.978 \pm 0.003$ and $2\Omega\lambda_F/u_0 = 1.32$ with $u_0 = 12.4$ mm/s (point A in figure 4-6(a)). (a) Time trace of the instantaneous radius of curvature which oscillates about a mean radius $R/\lambda_F = 0.92$. (b) Sample droplet trajectory (dashed curve) of 30 seconds duration, shown with the trajectory of the orbital center (solid curve). (c) Extended trajectory of the orbital center: a trace of 180 seconds is shown. (d) Time evolution of the (x,y) position of the orbital center, corresponding to the trajectory in (c). Data in (a)-(d) are from the same experiment.

Drifting wobbling orbits

In figure 4-6(a), significant variation in the wobbling amplitude is evident for certain fixed experimental parameters, particularly at high memory and high Ω. We now consider orbits with large wobbling amplitude corresponding to points A and B in figure 4-6(a). To better characterize the walker's motion, we track not only the trajectory's local radius of curvature, but the location of the orbital center as well. The orbital center at any point is computed by fitting a circle to a length of trajectory corresponding to one orbital period ($t = 2\pi/\omega$) using a least-squares method. The center of the fitted circle is defined as the orbital center for that portion of the trajectory. For example, using this method for a simple wobbling orbit such as that in figure 4-5(b) indicates negligible drift ($< 0.1\lambda_F$) of the orbital center.

In figure 4-7(a), we present a sample time trace of the local radius of curvature of the drifting wobbling orbit observed at $2\Omega\lambda_F/u_0 = 1.32$ and $\gamma/\gamma_F = 0.978$. In contrast to the stable wobbling observed at lower memory (figure 4-5(c)), clear fluctuations in the amplitude arise. A pronounced wobbling is apparent in the trajectory of the walker (figure 4-7(b)): the trajectory strongly deviates from a circle. Moreover, the orbit is no longer wobbling about a fixed point: the orbital center moves in a nearly circular orbit with radius approximately $0.2\lambda_F$. An extended trajectory of the orbital center (figure 4-7(c)) shows that it continues to move along a nearly circular trajectory, albeit with a slight linear drift. In figure 4-7(d), the coordinates of the orbital center are plotted with respect to time, indicating that the motion is nearly periodic with a frequency an order of magnitude less than that of the walker's $n = 1$ orbital frequency.

Wobble-and-leap dynamics

We now consider the effects of increasing the rotation rate to $2\Omega\lambda_F/u_0 = 1.35$ while keeping the forcing amplitude fixed, thus probing deeper into the region of unstable circular orbits. In figure 4-8(a), a sample time trace of the radius of curvature is presented. We now see alternating periods of increasing and decreasing wobbling amplitude. While this process is not precisely periodic, the distinct pattern of growth

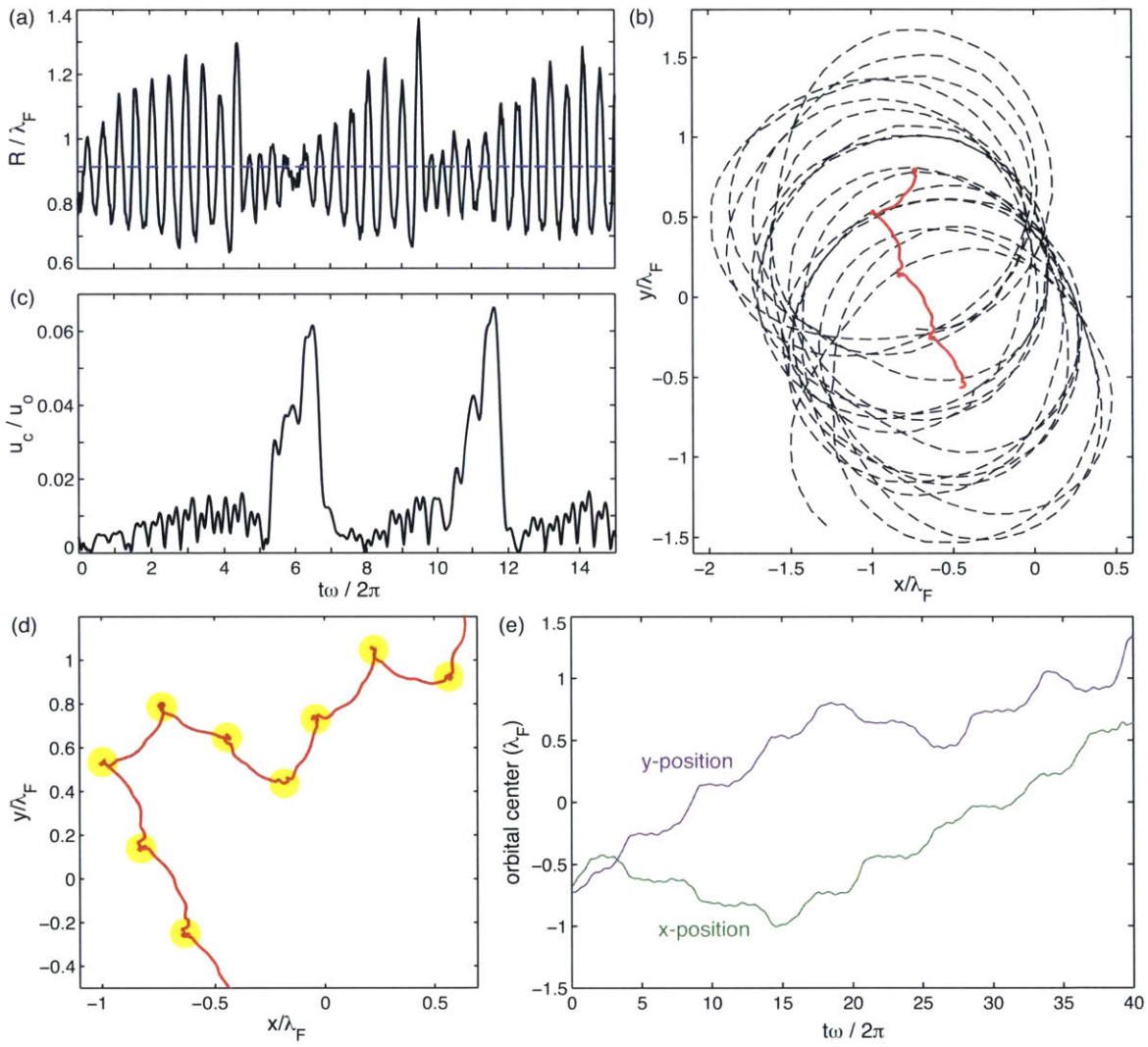

Figure 4-8: Wobble-and-leap dynamics. Results for $\gamma/\gamma_F = 0.978 \pm 0.003$ and $2\Omega\lambda_F/u_0 = 1.35$ with $u_0 = 12.4$ mm/s (point B in figure 4-6(a)). (a) Time trace of the instantaneous radius of curvature that oscillates about a mean radius $R/\lambda_F = 0.92$. (b) Sample droplet trajectory (dashed curve) of 37.5 seconds duration, shown with the trajectory of the orbital center (solid curve). (c) Drift speed of the orbital center (u_c) corresponding to the data in (a). (d) Extended trajectory of orbital center: a trace of 85 seconds is shown. Transiently stable orbital centers are highlighted via shading. (e) Time evolution of the (x,y) position of the orbital center, corresponding to the trajectory in (d). Data in (a)-(e) are from the same experiment.

and collapse is persistent. The walker's trajectory (figure 4-8(b)) suggests that there is also a net motion of the orbital center which follows a peculiar pattern. In particular, periods of negligible motion of the orbital center are punctuated by relatively rapid leaps to a new location. Comparing figure 4-8(c) to figure 4-8(a) indicates that the bursts of relatively rapid motion of the orbital center coincide with the periods of rapid decay in wobbling amplitude. We thus arrive at the following physical picture of 'wobble-and-leap' dynamics. A walker executes a nearly stationary orbit with a wobbling amplitude that grows progressively until it reaches a critical wobbling amplitude, approximately $A/\lambda_F = 0.35$. This wobbling of increasing amplitude is then interrupted by a relatively rapid leap phase, in which the wobbling amplitude is greatly reduced, and the orbital center shifts. The process then repeats itself.

An extended trajectory of the orbital center is presented in figure 4-8(d), which demonstrates that this wobble and leap process is robust and repeated continuously. The approximate locations of the transiently stable orbital centers are highlighted. Figure 4-8(e) indicates the time evolution of the orbital center. The plateau regions indicate that the orbital center is relatively stationary, corresponding to the wobbling phase; thereafter, brief periods of relatively large slope arise corresponding to the 'leaps'. While the time of a single wobble and leap cycle varies, the distance between successive centers is nearly constant. For this experiment, the average leap distance was $(0.36\pm0.05)\lambda_F$, very close to the first zero of $J_0(k_F r)$, $0.383\lambda_F$, which corresponds to the radius of the $n = 0$ orbit. No preferred leaping direction was apparent.

The trajectories corresponding to the data sets in figure 4-6(a) at the highest forcing amplitudes ($\gamma/\gamma_F = 0.978$ and 0.974) have a similar evolution as the rotation rate is increased beyond the onset of wobbling. Near the onset, the wobbling is of relatively small and constant amplitude, and the orbital center is effectively stationary for the duration of the experiment; here, we have simple wobbling orbits. As the rotation rate is increased further, the wobbling amplitude begins to fluctuate and the orbital center begins to drift slowly, often in small circular motions. Beyond this point, we observe the wobble and leap dynamics, characterized by periods of wobbling of increasing amplitude with a transiently stable orbital center, punctuated by a rapid

shift to a new location where the growth of the wobbling is reinitiated. Increasing the forcing amplitude even further leads to ever more complex trajectories.

4.1.4 Complex trajectories and multimodal statistics

Figures 4-9(a) and (b) show two sample trajectories obtained with identical experimental parameters, except for the forcing amplitude γ/γ_F. We see that the stable circular orbit (figure 4-9(a)) destabilizes into a complex trajectory (figure 4-9(b)) in response to the increased memory. In figure 4-9(c), we show a sample time trace of the local radius of curvature R of the trajectory presented in figure 4-9(b), which indicates that there are specific preferred radii of curvature. The histogram of R (figure 4-9(d)) indicates that even when its trajectory is complex and unpredictable, the walker still responds to the quantizing wave force imposed by its pilot wave field. Specifically, the peaks of the histogram correspond closely to the zeros of the Bessel function $J_0(k_F r)$, indicated by vertical dashed lines corresponding to the quantized orbital radii in the system (figure 4-3). Thus, while at any given moment it is practically impossible to predict the walker's trajectory, a coherent statistical pattern emerges: the droplet tends to move along curves with radius of curvature R corresponding to the unstable circular orbits, which occur roughly at integer multiples of $\lambda_F/2$. Despite the orbital solutions being unstable, they leave their mark on the walker's statistics.

In this high-memory limit, the walker is freed from its stable orbits to switch erratically between several orbital levels. But how does this transition come about and what determines which states are accessible? In figure 4-10(a)-(c) we present three different probability distributions for identical system parameters but increasing memory. In figure 4-10(a), the single peak reflects the quantized circular orbit at the n = 4 level arising at γ/γ_F = 0.975. As the memory is increased to γ/γ_F = 0.985 (figure 4-10(b)), the walker can access two orbital levels, namely n = 3 and n = 4. When the memory is increased to γ/γ_F = 0.990 (figure 4-10(c)), even more states become accessible, with each peak in the probability distribution corresponding to an unstable quantized orbit.

This progression is characterized comprehensively in figure 4-10(d), which includes

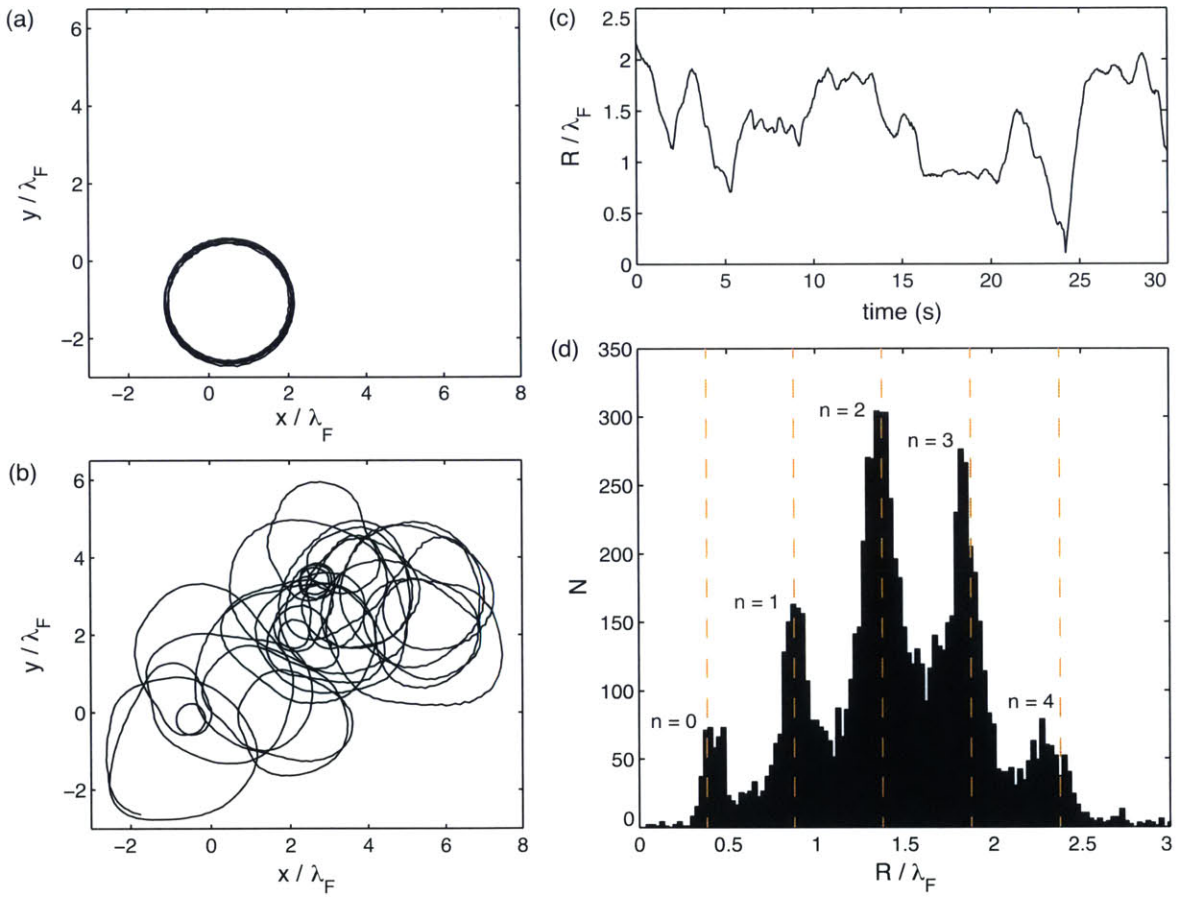

Figure 4-9: (a) Observed circular trajectory with $\gamma/\gamma_F = 0.922 \pm 0.004$, $u_0 = 9.5$ mm/s, and $\Omega = 0.98$ rad/s, in the rotating frame. (b) Complex observed trajectory at the same rotation rate Ω but increased forcing, $\gamma/\gamma_F = 0.988 \pm 0.002$, $u_0 = 11.3$ mm/s, in the rotating frame. (c) Sample time trace of the local radius of curvature. (d) Histogram of the local radius of curvature. 9130 measurements were taken over ≈ 8 minutes. Dashed vertical lines represent the zeros of the Bessel function $J_0(k_F r)$ corresponding to the radii of the unstable circular orbits. The bin size in part (d) is $0.025\lambda_F$. Data presented in (b), (c), and (d) are from the same experiment.

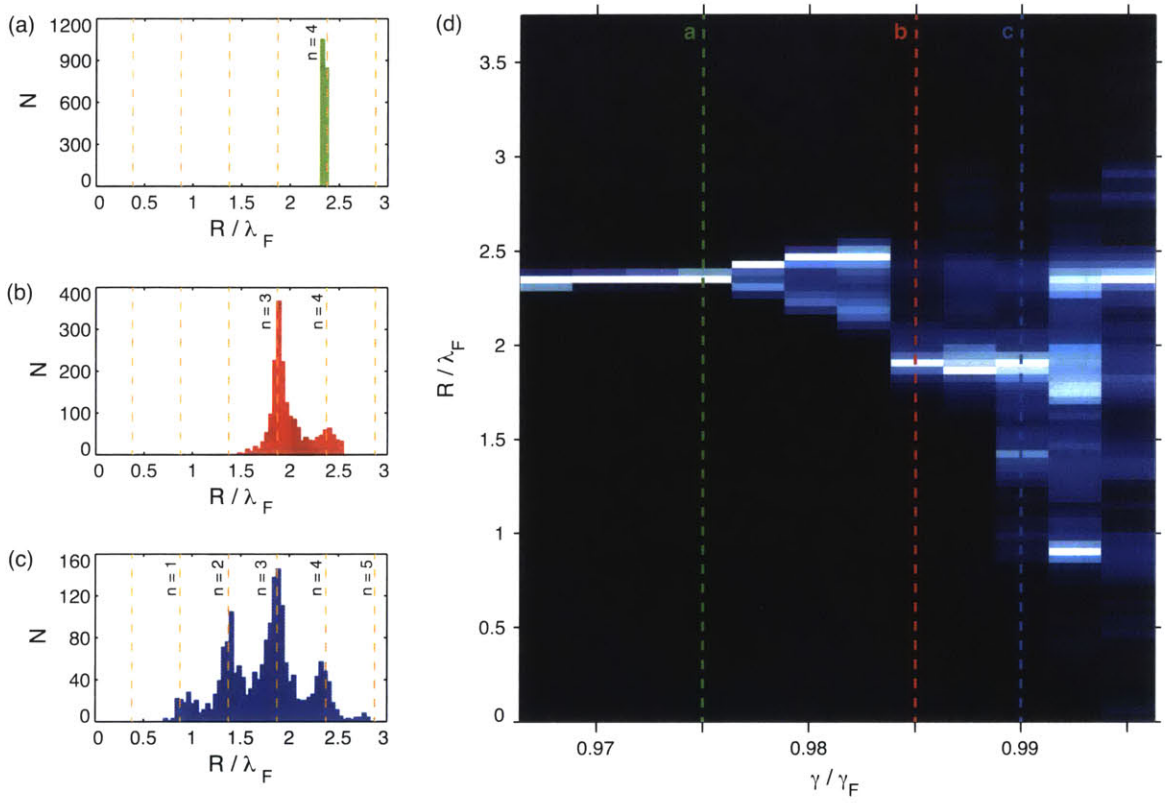

Figure 4-10: The dependence of the orbital statistics on the path memory. (a)-(c) Three sample probability distributions at the same rotation rate (Ω = 0.79 rad/s) for increasing forcing amplitudes (a) $\gamma/\gamma_F = 0.975 \pm 0.002$, (b) $\gamma/\gamma_F = 0.985 \pm 0.002$, and (c) $\gamma/\gamma_F = 0.990 \pm 0.002$. (d) Probability distribution of the radius of curvature R as a function of the forcing amplitude γ/γ_F at a fixed rotation rate (Ω = 0.79 rad/s). The brightest segment in each vertical column corresponds to the radius with the highest probability at that memory. The vertical dashed lines correspond to the three probability distributions shown in parts (a)-(c). The free walking speed is u_0 = 11.8 mm/s at $\gamma/\gamma_F = 0.968 \pm 0.002$. Each column represents 1900 measurements of the local radius of curvature taken over an experiment lasting 100 seconds. The bin size is fixed at $0.04\lambda_F$.

the three probability distributions presented in figures 4-10(a)-(c) at the positions denoted by the dashed vertical lines. Each vertical column represents a probability distribution for the radius of curvature of a single experiment at fixed parameters. Up to approximately $\gamma/\gamma_F = 0.975$, a stable circular orbit persists in the $n = 4$ orbital. Beyond this point, the single peak at $n = 4$ begins to spread, reflecting the onset of wobbling of increasing amplitude. At a critical point, when the wobbling amplitude becomes sufficiently large ($\gamma/\gamma_F = 0.985$), the walker escapes its confinement to the $n = 4$ orbital and drifts between multiple unstable orbital levels, as is permissible by virtue of the orbital degeneracy. As the memory is further increased, an increasing number of orbital states are accessible, each leaving their signature on the probability distribution in the form of a distinct peak. While the trajectory is disordered and complex, in each case the statistical behavior of the walker can be described in terms of a multimodal probability distribution with each peak centered at the radius of an unstable orbital level.

The influence of the rotation rate Ω on the form of the probability distribution for the radius of curvature R at fixed memory ($\gamma/\gamma_F = 0.988$) is illustrated in figure 4-11. Three sample probability distributions are provided in figures 4-11(a)-(c) for three different rotation rates. In each case, the walker accesses several orbital levels, with the mean R decreasing as the rotation rate is increased. Figure 4-11(d) provides a complete characterization of the dependence of the probability distribution on rotation rate Ω. As in figure 4-10(a), each vertical column corresponds to a probability distribution obtained for fixed experimental parameters. In general we see a shift from larger to smaller orbits as the rotation rate is increased, consistent with the trend evident in figure 4-3. Here, however, the walker may in general switch between several accessible orbitals during a single experiment. At the highest rotation rate considered, we see that the innermost circular orbit, $n = 0$, becomes stable.

The results presented in figures 4-10 and 4-11 indicate the manner in which the form of the probability distribution depends on the two control parameters, γ/γ_F and Ω. In general, γ/γ_F controls the number of accessible states, while Ω determines their mean radius. The distribution takes a multimodal form owing to the underlying

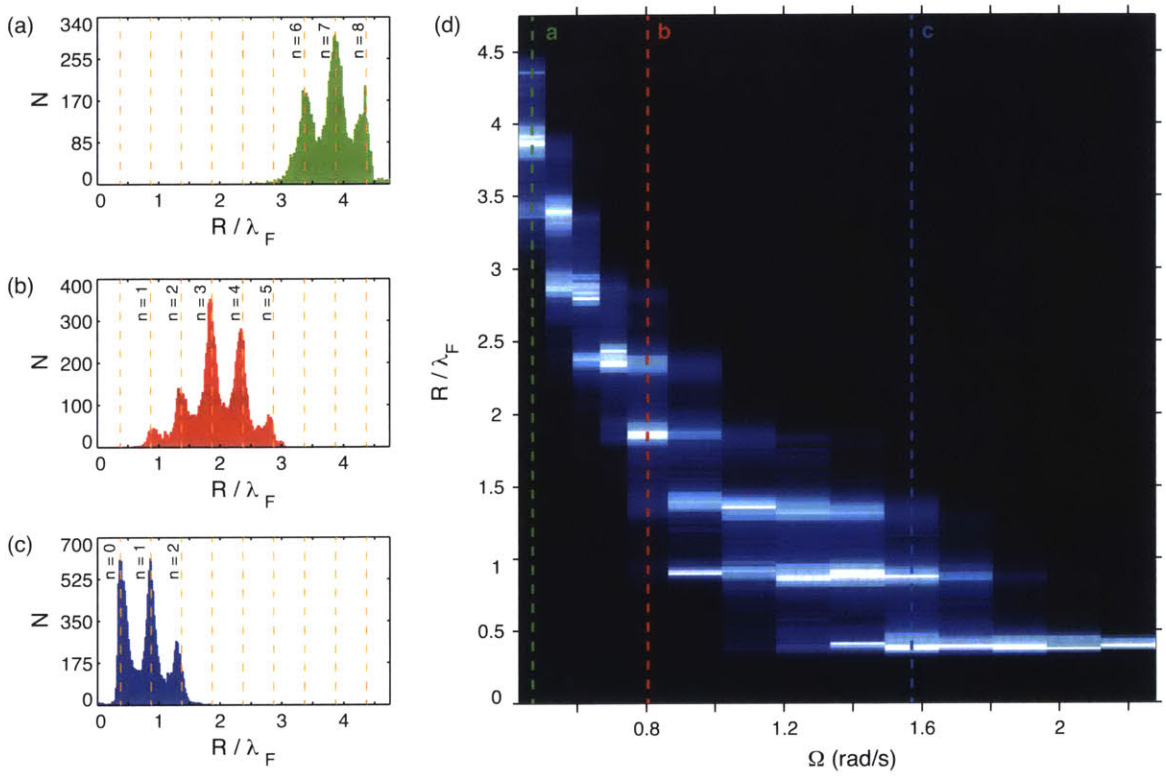

Figure 4-11: The dependence of the orbital statistics on the rotation rate Ω. (a)-(c) Three sample probability distributions at the same forcing amplitude (γ/γ_F = 0.988 ± 0.003) for increasing rotation rate (a) $\Omega = 0.47$ rad/s, (b) $\Omega = 0.79$ rad/s, and (c) $\Omega = 1.57$ rad/s. (d) Probability distribution of the radius of curvature R as a function of the rotation rate Ω at fixed forcing amplitude ($\gamma/\gamma_F = 0.988 \pm 0.003$) and free walking speed ($u_0 = 12.4 \pm 0.2$ mm/s). The brightest segment in each vertical column corresponds to the radius with the highest probability at that rotation rate. The vertical dashed lines correspond to the three probability distributions shown in parts (a)-(c). Each column represents a minimum of 4900 measurements of the local radius of curvature taken over an experiment lasting at least 250 seconds. The bin size is fixed at $0.02\lambda_F$.

pilot-wave dynamics, specifically to the dynamic imprint of the unstable orbits.

We note that, for the very high memories considered here, the wavefield is seen to extend to the edges of the fluid tray (figures 5-4(c) and (d)) which suggests the possible significance of boundary effects. Moreover, we have seen that in confinement to small geometries can also result in complex trajectories at high memory. However, in the current study, despite the similar forcing amplitudes considered, the region of confinement is significantly larger. In the absence of rotation, walkers in the current study follow simple periodic circular trajectories, moving along the boundary at a constant speed. In order for irregular trajectories to arise at high memory, the bulk system rotation must be applied. Finally, we note that at high memory, irregular trajectories with multimodal statistics are also observed in our numerical simulations of this rotating system, wherein boundaries are entirely absent [86]. Direct comparison with these numerical results suggests that boundary effects are not significant in our experiments.

4.1.5 Conclusions

We have characterized the influence of path memory on the dynamics of droplets walking in a rotating frame. At short path memory, the droplet executes a stable circular orbit whose radius decreases continuously and monotonically with increasing rotation rate. As the memory is increased, the orbiting droplet interacts with its own wake resulting in the quantization of both radius and frequency [52]. We have demonstrated that the orbital quantization does not represent the high memory limiting behavior of the system, but arises only within a finite range of memory. Moreover, the quantized orbits do not all appear at a single value of memory; rather, the number of quantized states increases with increasing memory, with each level being stable only within a finite range of memory. The smallest orbits have the shortest orbital period, and so are the first to be quantized by the wave field.

As the memory is increased progressively, the stable quantized circular orbits are superseded in turn by wobbling orbits with stationary, drifting, then leaping orbital centers, and ultimately by irregular trajectories. We have detailed this progression

for the $n = 1$ orbital level. As the memory is increased, the circular orbit gives way to a simple wobbling state, characterized by a periodic fluctuation in the local radius of curvature and a stationary orbital center. Thereafter, a smooth drift of the orbital center arises, accompanied by a fluctuating wobbling amplitude. Subsequently, wobble-and-leap dynamics arise in which orbital motion with a fixed orbital center and a growing wobbling amplitude is punctuated by brief periods of rapid motion of the orbital center. Finally, the wobbling is of sufficient amplitude to free the walker from its orbital confinement. An increasing number of orbital levels thus become accessible, and irregular trajectories emerge. In the high-memory limit, the radius of curvature at any instant is difficult to predict, as the walker switches erratically between arcs with curvatures corresponding to the unstable quantized levels. This particular feature of pilot-wave hydrodynamics leaves a distinct signature on the probability distribution of the radius of curvature; specifically, it is multimodal with peaks at the radii of the underlying unstable orbital states. The statistical pattern is thus a direct consequence of the underlying pilot-wave dynamics and the persistent influence of the unstable orbital states on the trajectory. The entire progression reported here will be rationalized through accompanying theoretical developments [84, 86].

It is interesting to consider our results in light of recent investigation of droplets walking in a central force field [90, 76]. By encapsulating a ferrofluidic droplet in silicone oil and applying a non-uniform external magnetic field, they were able to characterize the motion of a walker in a harmonic potential. At high memory, they observe circular orbits as well as more complex periodic trajectories (e.g. lemniscates) whose form is consistent with quantization in both energy (as prescribed by the orbital radius) and angular momentum. As in our study, switching between periodic states is prevalent at high memory. In their system, there is a fixed orbital center corresponding to the center of force. The absence of this constraint in our system allows for the observed drifting and leaping of the orbital center. While it is more difficult to define the energy of the orbital states in the rotating system, one can interpret the observed quantization in radius of curvature R as reflecting a quantization in angular

momentum, mu_0R, about the orbital center.

Finally, it is important to note that the entire progression from stable quantized orbits to wobbling orbits then irregular trajectories occurs within a few percent of the Faraday threshold, indicating that uniform, well-controlled vibration is essential for a reliable characterization of the statistical behavior of the walking droplets.

4.2 Numerical simulations

4.2.1 Trajectory equation

Moláček and Bush [82] derived a trajectory equation for the horizontal motion of the walking droplets:

$$m\ddot{\boldsymbol{x}}_d + D\dot{\boldsymbol{x}}_d = -mg\nabla h(\boldsymbol{x}_d, t). \tag{4.3}$$

The drop is slowed by a drag term proportional to its speed, and driven by the local slope of the wave field $h(\boldsymbol{x}, t)$ generated by its previous impacts with the free surface. Variables are defined in table 4.1. The height of the free surface can be written as a discrete sum of circularly symmetric standing waves centered at the location of each impact:

$$h(\boldsymbol{x}, t) = \sum_{n=-\infty}^{\lfloor t/T_F \rfloor} AJ_0\left(k_F \left|\boldsymbol{x}(t) - \boldsymbol{x}_d(nT_F)\right|\right) \mathrm{e}^{-(t-nT_F)/(T_F M_e)}. \tag{4.4}$$

This model assumes that the walker impacts the free surface once every Faraday period, as is the case for resonant walkers. Oza *et al.* [85] recast the trajectory equation in terms of an integro-differential equation for the horizontal trajectory of a walking droplet in the absence of boundaries or external forces by approximating the

Portions of this section appear as published in: A. U. Oza, and Ø. Wind-Willassen, D. M. Harris, R. R. Rosales, and J. W. M. Bush. Pilot-wave hydrodynamics in a rotating frame: exotic orbits. *Physics of Fluids*, 26(8):082101, 2014 [86].

sum as an integral:

$$m\ddot{\boldsymbol{x}}_d + D\dot{\boldsymbol{x}}_d = \frac{F}{T_F}\int_{-\infty}^{t} \frac{J_1\left(k_F\left|\boldsymbol{x}_d(t)-\boldsymbol{x}_d(s)\right|\right)}{\left|\boldsymbol{x}_d(t)-\boldsymbol{x}_d(s)\right|}\left(\boldsymbol{x}_d(t)-\boldsymbol{x}_d(s)\right)\mathrm{e}^{-(t-s)/(T_F M_e)}\,\mathrm{d}s. \tag{4.5}$$

This approximation is valid provided the timescale of horizontal motion $T_H = \lambda_F/|\dot{\boldsymbol{x}}_d|$ is much greater than the timescale of vertical motion T_F, as is the case in the experiments. An experimental depiction of this model is captured by strobing the walking droplet at the moment of impact, as shown in figure 4-12. The simulations in this study were performed using the fluid parameters corresponding to the silicone oil used in the experiments (ν = 20 cS), and with R_D = 0.4 mm and $\sin\Phi$ = 0.2. The impact phase, $\sin\Phi$, is chosen to best match the experimentally observed free speed of the walkers, and remains fixed in our simulations.

Equation (4.5) can be readily adapted for investigations of a walker in a rotating frame [84] through the inclusion of the Coriolis force, $-2m\boldsymbol{\Omega}\times\dot{\boldsymbol{x}}_d$, which depends on the walker's velocity $\dot{\boldsymbol{x}}_d$ and the rotation rate of the bath $\boldsymbol{\Omega}$. Note that we do not need to include a centrifugal force in the rotating frame, as the impact force provided by the parabolic surface deformation of the bath balances this force exactly. This is readily demonstrated experimentally, as a stable bouncing droplet remains stationary in the reference frame of the bath, even when the bath is rotating. We thus arrive at the following governing equation for the trajectory of the walker in the rotating frame:

$$\begin{aligned} &m\ddot{\boldsymbol{x}}_d + D\dot{\boldsymbol{x}}_d \\ &\quad = \frac{F}{T_F}\int_{-\infty}^{t} \frac{J_1\left(k_F\left|\boldsymbol{x}_d(t)-\boldsymbol{x}_d(s)\right|\right)}{\left|\boldsymbol{x}_d(t)-\boldsymbol{x}_d(s)\right|}\left(\boldsymbol{x}_d(t)-\boldsymbol{x}_d(s)\right)\mathrm{e}^{-(t-s)/(T_F M_e)}\,\mathrm{d}s - 2m\boldsymbol{\Omega}\times\dot{\boldsymbol{x}}_d. \end{aligned} \tag{4.6}$$

We non-dimensionalize equation (4.6), introducing the dimensionless variables $\hat{\boldsymbol{x}} = k_F\boldsymbol{x}_d$, $\hat{t} = t/T_F M_e$ and $\hat{\boldsymbol{\Omega}} = 2m\boldsymbol{\Omega}/D$. Using primes to denote differentiation with respect to the non-dimensional time $\hat{t}$, we recast the trajectory equation in dimen-

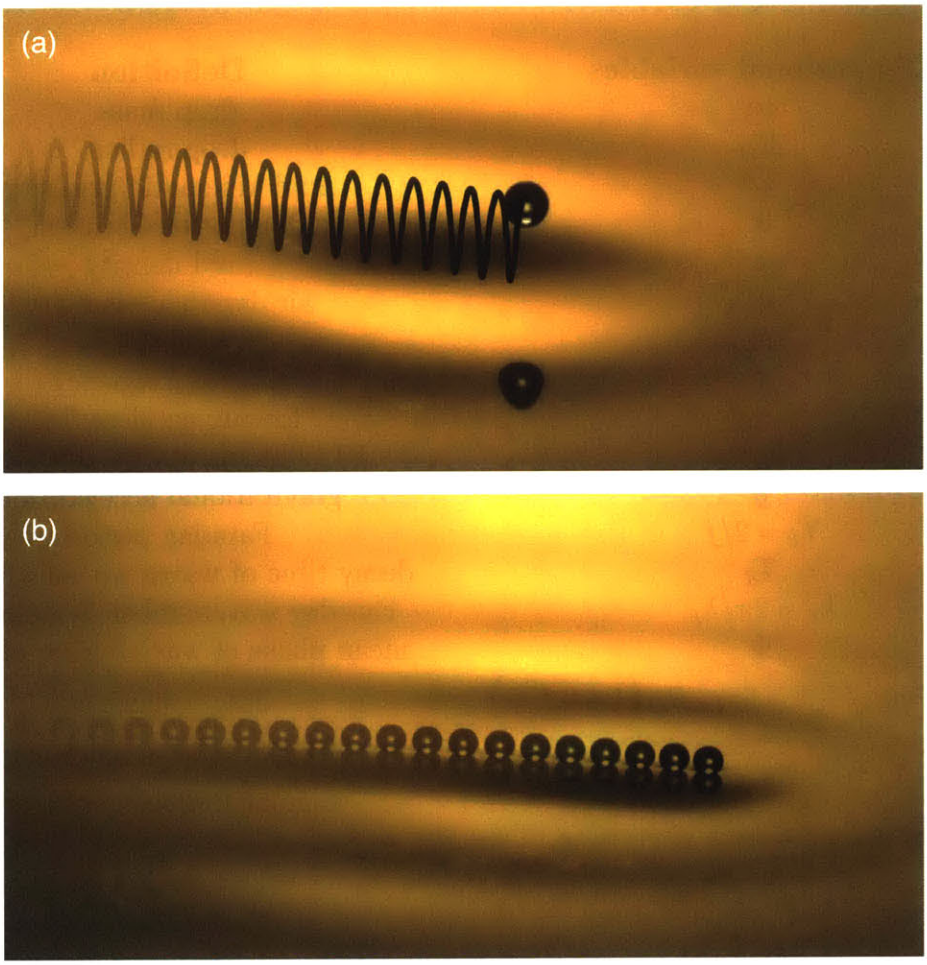

Figure 4-12: (a) A walking droplet bounces as it moves along the surface of a vibrated fluid bath. (b) Strobed motion of a walking droplet. Images of the droplet taken at the moment of impact are superposed. One image per two bouncing cycles is shown.

Dimensional variables	**Definition**
m	drop mass
R_D	drop radius
ν	fluid kinematic viscosity
σ	fluid surface tension
ρ	fluid density
μ_a	air dynamic viscosity
ρ_a	air density
f	forcing frequency
γ	forcing acceleration
γ_F	Faraday instability threshold
g	gravitational acceleration
$T_F = 2/f$	Faraday period
T_d	decay time of waves without forcing
$k_F = 2\pi/\lambda_F$	Faraday wavenumber, wavelength
Φ	mean phase of wave during contact
$D = 0.17mg\sqrt{\frac{\rho R_D}{\sigma}} + 6\pi\mu_a R_D\left(1 + \frac{\rho_a g R_D}{12\mu_a f}\right)$	drag coefficient
$F = \sqrt{\frac{1.5795\nu}{2\pi T_F}}\frac{mgk_F^4}{3k_F^2\sigma+\rho g}mgT_F\sin\Phi$	wave force coefficient
$\boldsymbol{\Omega} = \Omega\hat{\boldsymbol{z}}$	angular frequency of bath
Nondimensional variables	
$M_e = \frac{T_d}{T_F(1-\gamma/\gamma_F)}$	memory
$\kappa = \frac{m}{DT_F M_e}$	nondimensional mass
$\beta = \frac{Fk_F T_F M_e^2}{D}$	nondimensional wave force coefficient
$\hat{\boldsymbol{\Omega}} = \frac{2m\boldsymbol{\Omega}}{D}$	nondimensional angular frequency of bath

Table 4.1: The variables in the trajectory equations (4.3), (4.5), (4.6), and (4.7).

sionless form:

$$\kappa\hat{\boldsymbol{x}}'' + \hat{\boldsymbol{x}}' = \beta \int_{-\infty}^{\hat{t}} \frac{J_1\left(\left|\hat{\boldsymbol{x}}(\hat{t}) - \hat{\boldsymbol{x}}(\hat{s})\right|\right)}{\left|\hat{\boldsymbol{x}}(\hat{t}) - \hat{\boldsymbol{x}}(\hat{s})\right|} \left(\hat{\boldsymbol{x}}(\hat{t}) - \hat{\boldsymbol{x}}(\hat{s})\right) \mathrm{e}^{-(\hat{t}-\hat{s})}\, \mathrm{d}\hat{s} - \hat{\boldsymbol{\Omega}} \times \hat{\boldsymbol{x}}'. \tag{4.7}$$

In the following section, we review the circular orbital solutions to this equation and the stability of such solutions as a function of the memory.

4.2.2 Review of linear stability

If we assume the walker follows a circular trajectory, specifically, $\hat{\boldsymbol{x}}(\hat{t}) = \hat{\boldsymbol{x}}_O(\hat{t}) = (\hat{r}_0 \cos\hat{\omega}\hat{t}, \hat{r}_0 \sin\hat{\omega}\hat{t})$, $\hat{r}_0$ and $\hat{\omega}$ are defined in terms of M_e and $\hat{\Omega}$ through the following equations [84]:

$$\begin{aligned} -\kappa\hat{r}_0\hat{\omega}^2 &= \beta \int_0^\infty J_1\left(2\hat{r}_0 \sin\frac{\hat{\omega}z}{2}\right) \sin\frac{\hat{\omega}z}{2} \mathrm{e}^{-z}\, \mathrm{d}z + \hat{\Omega}\hat{r}_0\hat{\omega} \\ \hat{r}_0\hat{\omega} &= \beta \int_0^\infty J_1\left(2\hat{r}_0 \sin\frac{\hat{\omega}z}{2}\right) \cos\frac{\hat{\omega}z}{2} \mathrm{e}^{-z}\, \mathrm{d}z. \end{aligned} \tag{4.8}$$

This system of equations can be solved numerically. The theoretical predictions of the radius of the orbit as a function of the rotation rate of the bath is shown in figure 4-13, color-coded according to their stability [84]. For every value of the forcing amplitude γ/γ_F, circular solutions of all radii exist, however, not all such solutions are linearly stable. At low memory, all circular solutions are stable. As the memory is increased, bands of radii become inaccessible due to their loss of stability, which is the origin of the apparent quantization of orbital radius. We expect and observe wobbling orbits along the green portions of the curves, which are characterized by an oscillatory instability of the circular solution.

The complete results of the stability analysis of Oza *et al.* [84] are summarized in figure 4-14. The blue regions separated by the red tongues are labeled by their corresponding orbital level n. Note that as the memory is increased, virtually all circular solutions become unstable. To capture the nonlinear behavior in the unstable regions we explore numerical simulations of the trajectory equation.

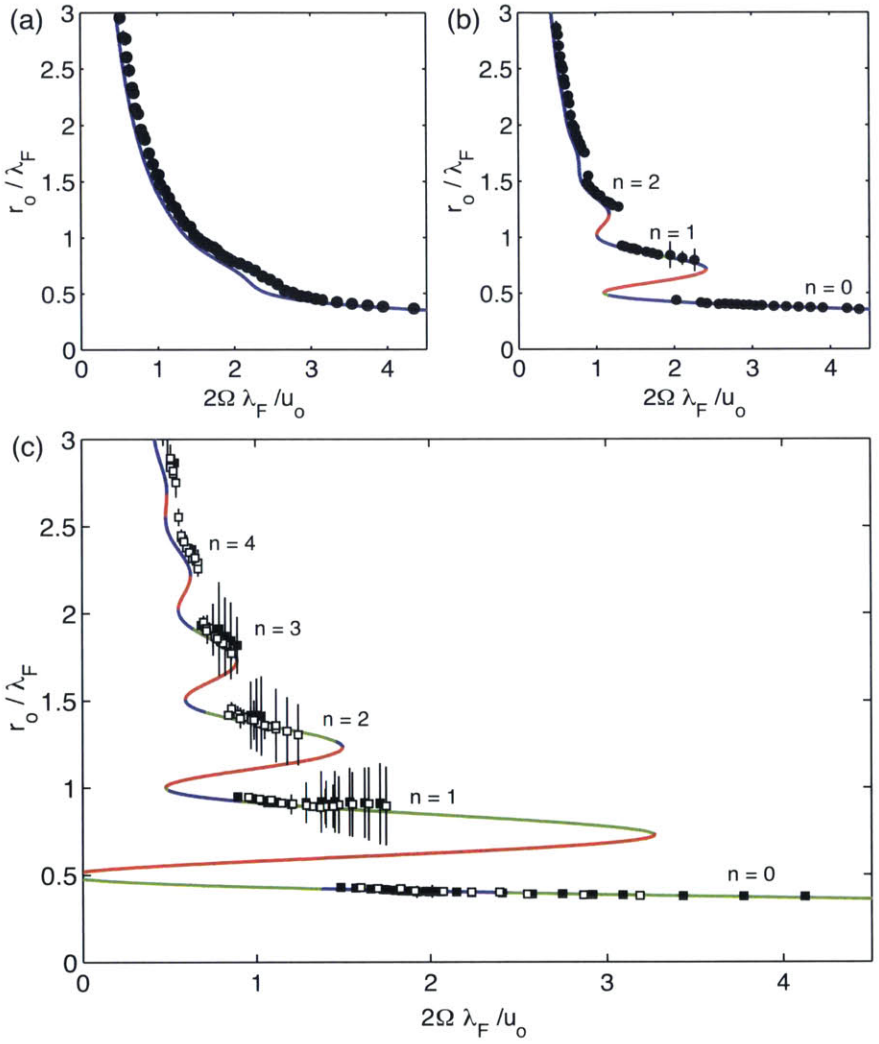

Figure 4-13: Measured orbital radius r_0 as a function of the bath's rotation rate Ω. (a) $\gamma/\gamma_F = 0.922 \pm 0.004$ with $u_0 = 9.5$ mm/s, (b) $\gamma/\gamma_F = 0.954 \pm 0.006$ with $u_0 = 12.0$ mm/s, (c) $\gamma/\gamma_F = 0.971 \pm 0.004$ with $u_0 = 10.9$ mm/s (■) and 11.7 mm/s (□). The curves in are theoretical predictions obtained by solving (4.8) using the experimental parameters. The blue segments are linearly stable, the red linearly unstable, and the green linearly unstable oscillatory solutions.

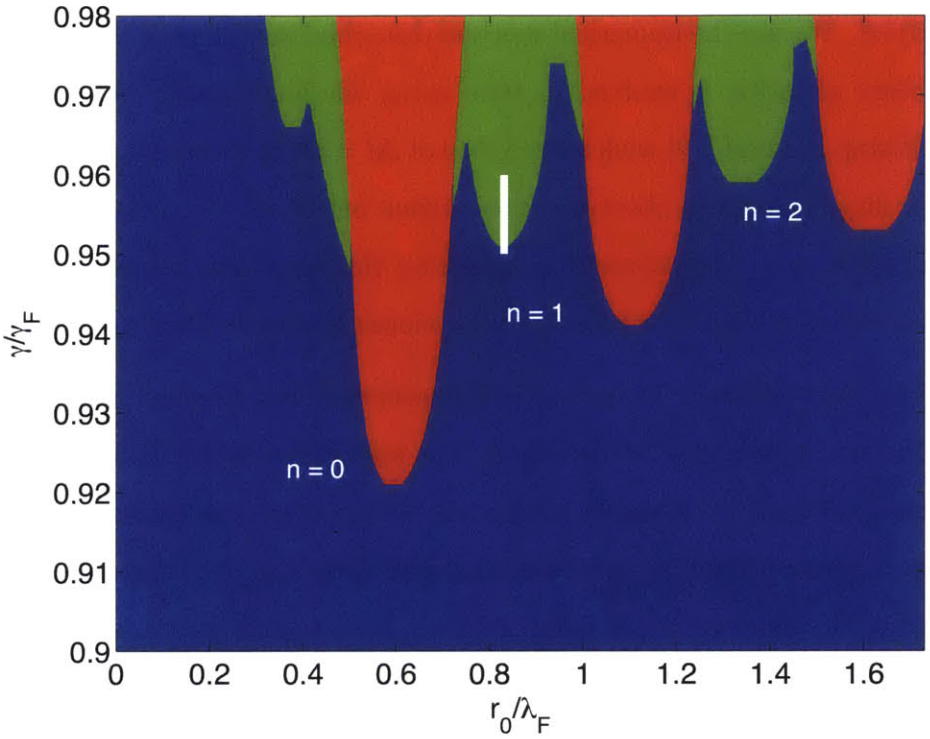

Figure 4-14: Theoretical linear stability diagram computed using typical values for experimental parameters (drop radius R_d = 0.4 mm, mean impact phase $\sin\Phi = 0.20$, and fluid viscosity ν = 20 cS). Blue regions correspond to stable orbital solutions, red to unstable solutions (largest eigenvalue is real), and green to unstable solutions with an oscillatory component (largest eigenvalue is complex). The white vertical line shows the range of parameters investigated in section 4.2.4. Figure adapted from [86].

4.2.3 Nonlinear behavior

Note that specifying both the memory γ/γ_F and the non-dimensional radius r_o/λ_F uniquely determines a circular orbital solution [84]. Thus we initialize our simulations with this circular orbit, specifically, $\hat{\boldsymbol{x}}(\hat{t}) = \hat{\boldsymbol{x}}_O(\hat{t})$ for time $\hat{t} < 0$. At time $\hat{t} = 0$, we apply a perturbation to the position of the walker equal to $\boldsymbol{\delta} = (0.02, 0)$, so that $\hat{\boldsymbol{x}}_0 = \hat{\boldsymbol{x}}_O(0) + \boldsymbol{\delta}$. We use the numerical method described in Oza *et al.* [86]. Specifically, the trajectory equation is evolved in time using the fourth-order Adams-Bashforth linear multistep method [19] with a time step of $\Delta\hat{t} = 2^{-6}$ to at least $\hat{t}_{max} = 1000$, which is typically large enough to observe the long-time behavior. The integral is computed using Simpson's rule. We proceed by exploring the long-time behavior of the orbits with initial radius $0 < r_0/\lambda_F < 1.73$ and vibrational forcing $0.900 < \gamma/\gamma_F < 0.980$.

The long-time behavior at each set of parameters investigated is summarized in figure 4-15 and color-coded according to the legend beneath the figure. The blue regions represent areas of stability where the perturbation decays and the trajectory transitions back to a circular orbit with its initial radius. These stable regions also correspond to the blue regions in figure 4-14, as predicted on the basis of linear theory. However, exotic behaviors are observed in the linearly unstable regions, specifically, within the red and green tongues of figure 4-14. We find that for many choices of parameters, the circular orbits simply find a larger or smaller orbital radius, given by the red and pink regions respectively. These orbits then evolve into stable circular orbits or into irregular orbits with a significantly different mean radius. The green and white regions correspond to wobbling orbits with stable radial oscillations of approximately twice and thrice the orbital frequency (ω), respectively. Drifting orbits (black) and wobble-and-leap (purple) orbits are also observed in the trajectory simulations. At large vibration amplitude, most orbits are chaotic, that is, characterized by a chaotic switching between orbital radii with no apparent periodicity. Embedded within these chaotic yellow regions, complex periodic or quasiperiodic trajectories arise, as indicated in cyan.

We also explored the behavior of the orbital radius as a function of memory for

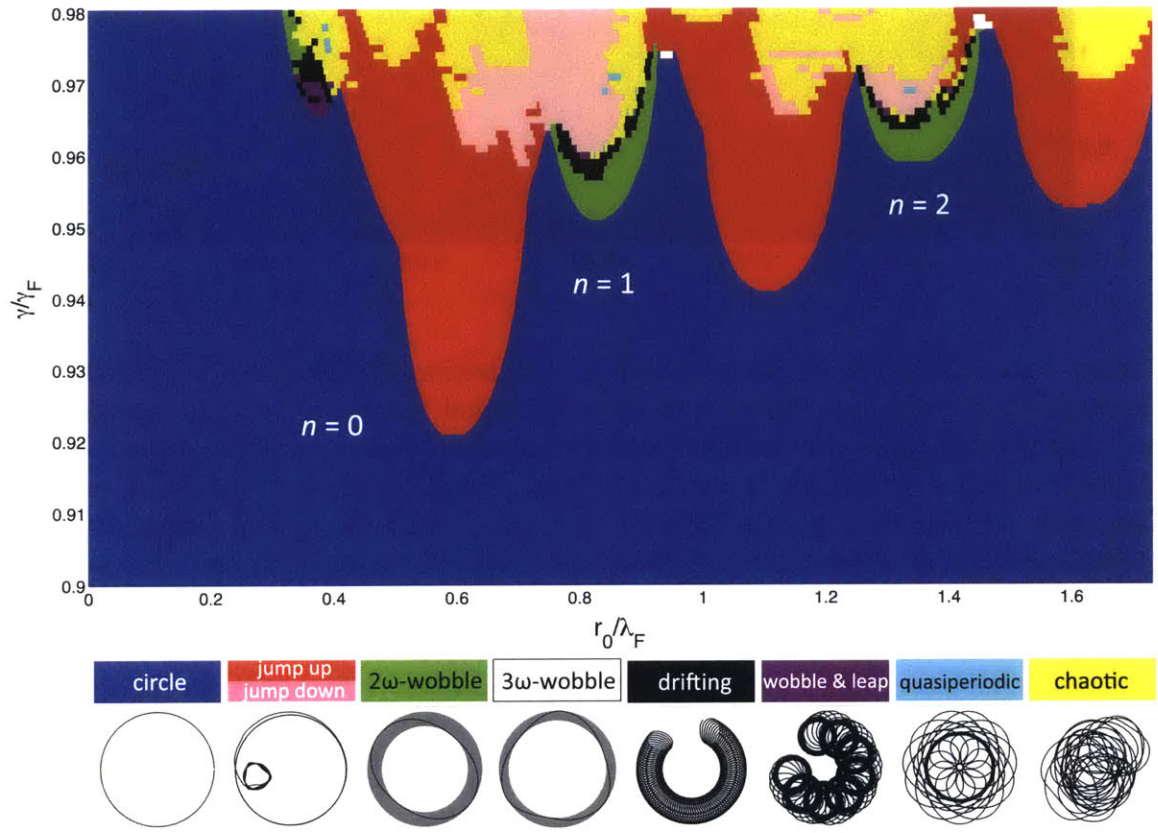

Figure 4-15: Regime diagram exploring the dependence of the walker's orbital behavior on the initial radius r_0/λ_F and vibrational forcing γ/γ_F. The qualitative form of the trajectory is color-coded according to the legend beneath the figure. Figure adapted from [86].

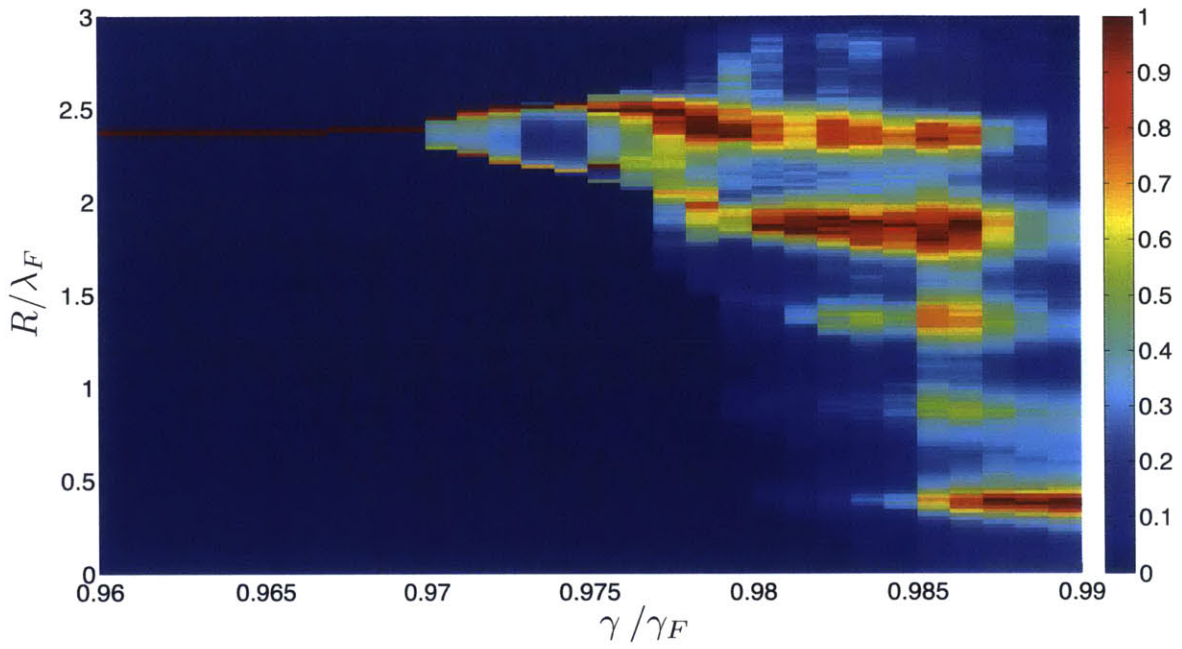

Figure 4-16: Evolution of the probability distribution of the trajectory's radius of curvature ($\alpha = \pi/2$) as a function of the vibrational forcing γ/γ_F. The simulations were initiated with the circular orbit at $n = 4$ corresponding to the fixed dimensionless rotation rate $\hat{\Omega} = 0.1784$ (or $\Omega = 0.70$ s^{-1}), with time step $\Delta\hat{t} = 2^{-8}$ and $\hat{t}_{max} = 1000$. The most red segment in each vertical column corresponds to the radius with the highest probability at that memory. Note that the red segments lie near the zeros of $J_0(k_F r)$. Figure adapted from [86].

a fixed rotation rate, as was characterized experimentally in figure 4-10. We fixed the rotation rate to $\Omega = 0.70$ s^{-1}, and initialize the orbit in the $n = 4$ orbital level. The forcing is then gradually increased. The statistical behavior of the radius of curvature ($\alpha = \pi/2$) is presented in figure 4-16. At low memory, the circular orbital solution is stable, and the radius of curvature is simply constant. However, as the forcing amplitude is increased, this single peak begins to spread due to the onset of wobbling. As the forcing amplitude is increased further, the distribution becomes multimodal with several peaks, spaced apart by approximately $\lambda_F/2$, as was observed in experiment. The statistical behavior can be understood as a chaotic switching between unstable orbits, with radii corresponding to the zeros of $J_0(k_F r)$.

4.2.4 Transition to chaos

Our interest in this section is to characterize the transition from stable circular orbits to chaotic orbits as the memory is gradually increased. In particular we focus on the circular solutions with $r_o/\lambda_F = 0.83$ in the $n = 1$ region, below and within the green tongue (figure 4-14). For these simulations we fix the initial radius to $r_o/\lambda_F = 0.83$ and increase the forcing γ/γ_F by 0.0001 for $0.9500 < \gamma/\gamma_F < 0.9600$. Note that the rotation rate Ω is chosen in each simulation such that the circular orbit with $r_o/\lambda_F = 0.83$ remains a solution, either stable or unstable, to equation (4.8). The same fluid and droplet parameters are used as before, with $\Delta\hat{t} = 2^{-6}$ and $\hat{t}_{max} = 1000$, unless stated otherwise. In this section, for each trajectory we compute the instantaneous radius of curvature R and a sequence of its local maxima, R_m. If the computed trajectory is $\boldsymbol{x}_d(t) = (x(t), y(t))$, R is calculated using a centered-difference method as

$$R = \frac{(\dot{x}^2 + \dot{y}^2)^{3/2}}{|\dot{x}\ddot{y} - \dot{y}\ddot{x}|}. \tag{4.9}$$

In figure 4-17 we plot sample traces of the radius of curvature for several values of γ/γ_F. These traces occur sufficiently far after the initial perturbation that the trajectory has transitioned to its asymptotic behavior. For $\gamma/\gamma_F < 0.9508$, the radius of curvature is constant, indicating a circular orbit (figure 4-17(a)). Above this value of forcing, the radius of curvature oscillates with different periodicities. For $\gamma/\gamma_F = 0.9540$ we see that the radius of curvature oscillates with approximately twice the orbital period T with a single value for the local maxima (figure 4-17(b)). This corresponds to what we have referred to previously as a simple or 2ω-wobbling orbit. T is defined here to be a typical orbital period, obtained by identifying the largest peak in the frequency spectrum of $x(t)$. At higher forcing, $\gamma/\gamma_F = 0.9580$, the peaks of R alternate in magnitude between two values, in a period-2 oscillation (figure 4-17(c)). This is similar to the alternating peak structure in the radius of curvature observed for the drifting orbit observed experimentally (figure 4-7(a)). At $\gamma/\gamma_F = 0.9586$, a period-4 oscillation is observed with four distinct values of R_m (figure 4-17(d)). Finally, at $\gamma/\gamma_F = 0.9590$, chaotic oscillations in the radius of curvature are present, with no

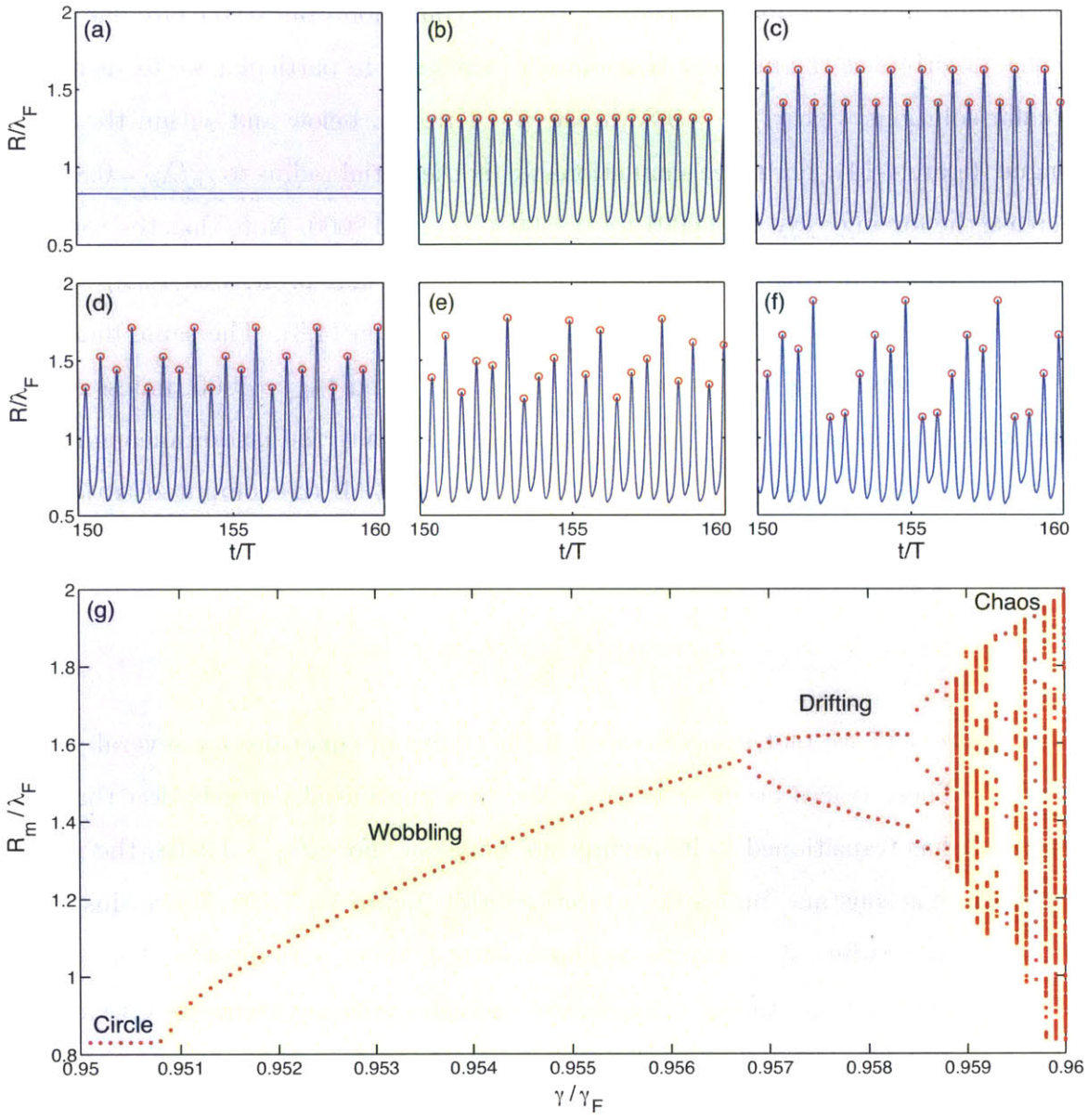

Figure 4-17: Evolution of the instantaneous radius of curvature R with forcing amplitude γ/γ_F for fixed initial radius $r_o/\lambda_F = 0.83$. Local maxima in the radius of curvature are identified by the red circles. (a) Circular orbit, $\gamma/\gamma_F = 0.9500$. (b) Simple wobbling orbit, $\gamma/\gamma_F = 0.9540$. (c) Period-2 wobbling, drifting orbit, $\gamma/\gamma_F = 0.9580$. (d) Period-4 wobbling, drifting orbit, $\gamma/\gamma_F = 0.9586$. (e) Chaotic wobbling orbit, $\gamma/\gamma_F = 0.9590$. (f) Period-6 wobbling orbit, $\gamma/\gamma_F = 0.9594$. (g) Bifurcation diagram showing local maxima of the radius of curvature as a function of forcing amplitude γ/γ_F. The color coding of the regions is identical to that of figure 4-15.

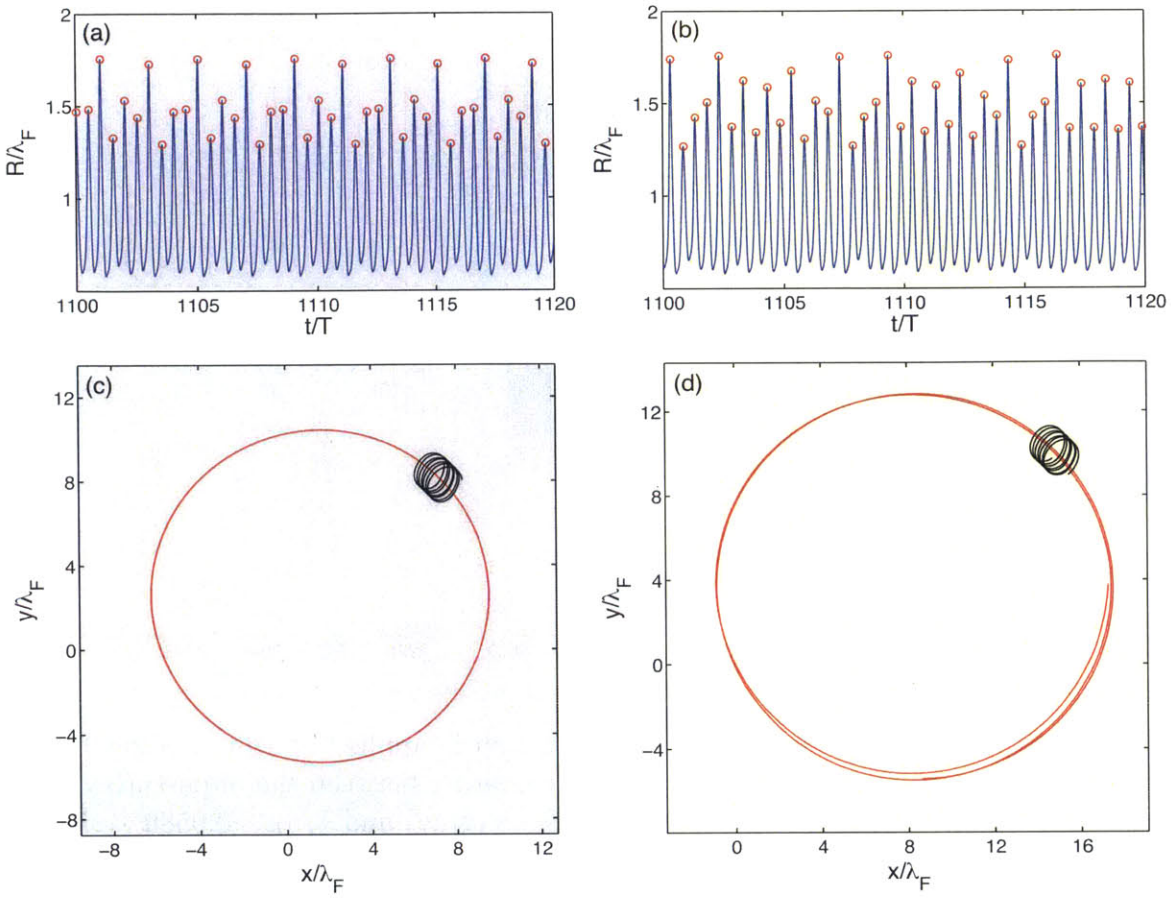

Figure 4-18: Time trace of the instantaneous radius of curvature for (a) a period-8 wobbling orbit and (b) a chaotic wobbling orbit. (c-d) A segment of the actual trajectory is shown in black, whereas the trajectory of the orbital center is shown in red. Forcing amplitude for panels (a,c) is $\gamma/\gamma_F = 0.9588$ and for panels (b,d) is $\gamma/\gamma_F = 0.9589$, each of duration $\hat{t}_{max} = 5000$.

apparent periodicity in the local maxima (figure 4-17(e)). Note that throughout the entire transition to chaos, the principal oscillations occur with approximately twice the orbital frequency. Within the chaotic regime, windows of periodicity are also observed, for example, at $\gamma/\gamma_F = 0.9594$, a period-6 oscillation is obtained (figure 4-17(f)). The transition to chaos can be summarized by the bifurcation diagram in figure 4-17(g) which clearly demonstrates that the transition from stable circular orbits to chaotic wobbling orbits occurs via a classic period-doubling bifurcation [98].

The simple wobbling orbits have a fixed orbital center. The wobbling orbits of period-2^n correspond to drifting wobbling orbits whose orbital centers move along

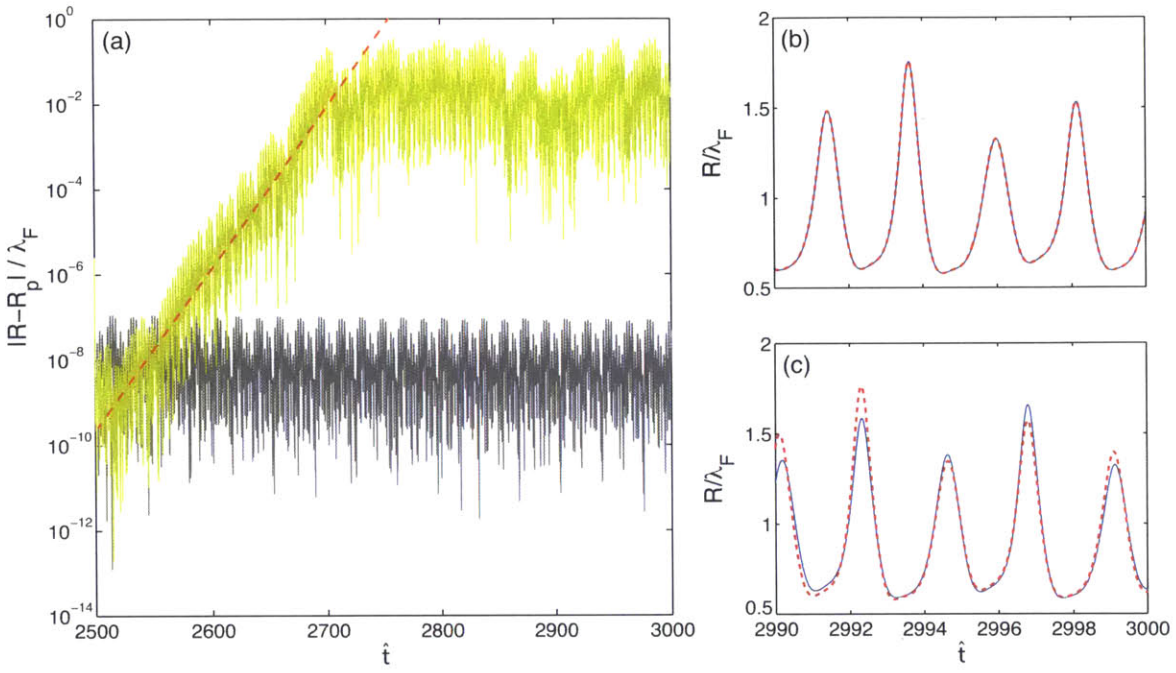

Figure 4-19: A small perturbation in the position is applied at time $\hat{t} = 2500$. (a) The difference in the instantaneous radius of curvature between the unperturbed and perturbed trajectories is shown for $\gamma/\gamma_F = 0.9588$ (gray) and $\gamma/\gamma_F = 0.9589$ (yellow). (b-c) Time trace of instantaneous radius of curvature for unperturbed (solid) and perturbed (dashed) trajectories for (b) $\gamma/\gamma_F = 0.9588$ and (c) $\gamma/\gamma_F = 0.9589$.

a closed circular path (figure 4-18(c)). In the chaotic wobbling regime investigated here, the orbital centers also drift, but their motion does not form a closed loop, as shown in figure 4-18(d). The transition to chaotic wobbling occurs in the range $0.9588 < \gamma/\gamma_F < 0.9589$, and the entire cascade occurs within a single percent of our control parameter, the forcing amplitude.

Although the trajectories in figure 4-18 appear similar, their sensitivity to perturbations is markedly different. At time $\hat{t} = 2500$ we apply a small perturbation to the position and continue to evolve the trajectory, obtaining a second trajectory $\hat{\boldsymbol{x}}_p(t)$ which we can then compare to the unperturbed trajectory $\hat{\boldsymbol{x}}(t)$. Specifically, we consider a perturbation of the form $\hat{\boldsymbol{x}}_p(2500) = \hat{\boldsymbol{x}}(2500) + (10^{-8}, 0)$ and plot the absolute difference between the instantaneous radius of curvature of the unperturbed and perturbed trajectory, $|R - R_p|$ in figure 4-19(a). Up until $\hat{t} = 2500$ the trajectories are identical thus $|R - R_p| = 0$ for $\hat{t} < 2500$. We see that for $\hat{t} > 2500$ and $\gamma/\gamma_F = 0.9588$

the difference oscillates, but slowly decays, whereas for $\gamma/\gamma_F = 0.9589$ the difference grows exponentially until saturating. We also plot sample time traces for the instantaneous radius of curvature in figures 4-19(b) and 4-19(c). For the non-chaotic, period-8 trajectory ($\gamma/\gamma_F = 0.9588$) the unperturbed and perturbed time traces are virtually indistinguishable. For the chaotic trajectory ($\gamma/\gamma_F = 0.9589$), there are visible differences in the oscillation amplitude between the two traces.

We increased the temporal resolution in the simulations to $\Delta\hat{t} = 2^{-8}$ and again found a transition to chaos between $0.9588 < \gamma/\gamma_F < 0.9589$, indicating the stability of our numerical scheme. Further numerical investigations revealed that the period-doubling cascade of wobbling orbits appears to be generic for all orbital levels $n \geq 1$.

Chapter 5

Diffraction by a single slit

The Oxford English Dictionary defines diffraction as "the process by which a beam of light or other system of waves is spread out as a result of passing through a narrow aperture or across an edge, typically accompanied by interference between the wave forms produced." In 1924, Louis de Broglie hypothesized the wave nature of matter [30], for which he received the Nobel prize after the experimental observation of electron diffraction by Davisson and Germer [28]. In this chapter, we revisit Couder and Fort's seminal experiment of a walker passing through a single slit [22, 23], for which single-particle diffraction was reported.

In their experiments, Couder & Fort [22] sent a single walker towards a submerged barrier with a small opening on the scale of the guiding wavelength (Fig. 5-2). The walker was guided towards the slit by a submerged V-shaped structure located in the corner of the experimental cell. As the walker passed through the aperture, its trajectory was deviated by an angle α, due to the distortion of its pilot wave. They point out that this deflection could be interpreted in terms of an effective position-momentum uncertainly relation for the walkers: when confined spatially, the momentum in the direction of confinement becomes uncertain. The impact parameter y_i was defined as the location of the walker's incident trajectory relative to the centerline of the slit. They varied the impact parameter, uniformly spanning the slit in order to approximate an incident plane wave. They observed no correlation between y_i and α, from which one might infer that the walker dynamics was chaotic. When this experiment

was performed many times, preferred angles emerged, and the amplitude of the resultant statistical pattern corresponded roughly to the amplitude (rather than the intensity, proportional to the amplitude squared, as is observed in quantum mechanics) of a diffracted plane wave impinging on the slit. A number of key experimental parameters (e.g. drop size, forcing amplitude, and fluid depth above the barriers) were not reported and the system was not isolated from ambient air currents. Their results have yet to be reproduced, despite attempts by various groups (e.g. that of Anders Andersen and Tomas Bohr at DTU [1]).

5.1 Methods

The bath and droplet are composed of pure 20 cSt silicone oil with density ρ = 950 kg/m^3 and surface tension σ = 20.6 dynes/cm. The circular bath of depth h_o = 7.4 mm and diameter 16 cm is surrounded by a shallow border of width 9 mm and depth 1.5 mm. This shallow region serves to damp the waves generated by the oscillating meniscus at the edge of the container [44, 61]. The bath is driven sinusoidally with frequency f = 80 Hz and peak acceleration γ by an electromagnetic shaker guided by a linear air bearing which provides vertical vibration that is spatially uniform to within 0.1% [62]. The forcing is maintained at a constant acceleration amplitude to within $\pm 0.002g$ using closed-loop feedback control. Above the Faraday threshold, γ_F, subharmonic standing waves form spontaneously on the free surface of the vibrating bath [50] with a typical wavelength determined by the standard water-wave dispersion relation [5], here λ_F = 4.75 mm. The Faraday threshold is measured every 20 minutes and is always in the range $\gamma_F = 4.18 - 4.23g$, with the variation resulting from the sensitivity of the fluid viscosity to temperature [4, 61]. The uncertainty in the Faraday threshold measurement is $\pm 0.005g$.

Unless otherwise stated, silicone oil droplets of diameter $D = 0.67 \pm 0.01$ mm are used, and generated by a piezoelectric droplet generator [107, 101, 63] with repeatability in diameter to within 1%. The droplets are deposited gently onto the bath by bouncing and sliding them down a curved surface wetted with the same silicone

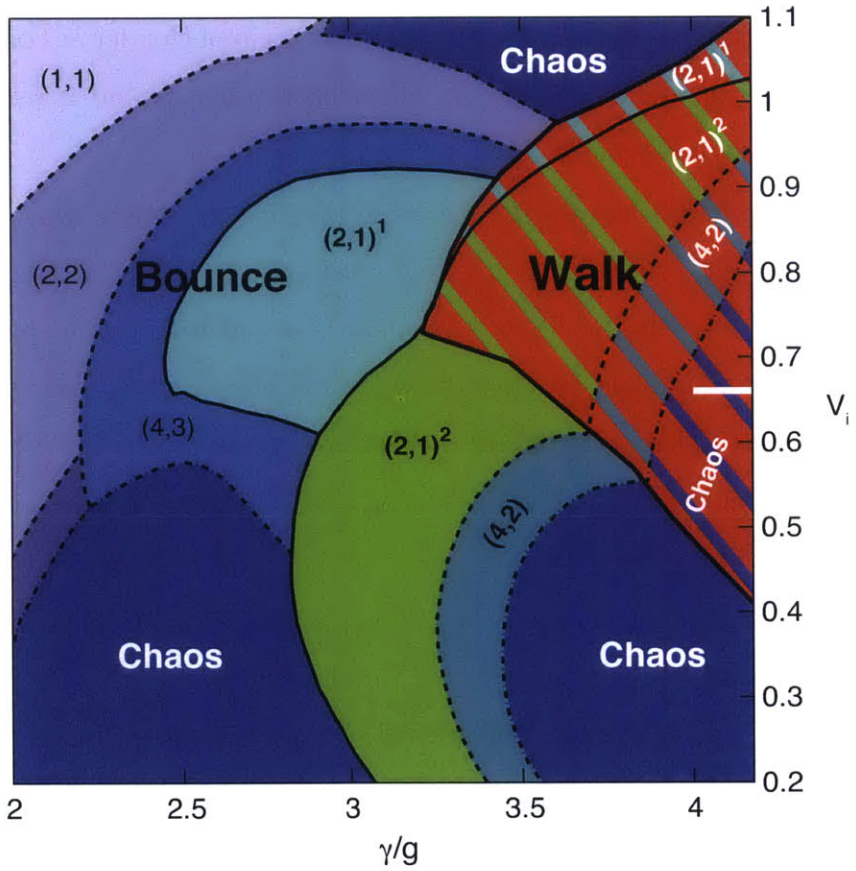

Figure 5-1: Vertical dynamics as a function of the forcing amplitude γ/g and the vibration number $V_i = 2\pi f\sqrt{\rho D^3/8\sigma}$ for the parameters considered in our study [105]. Regions are labeled by (m,n), as indicates the different predicted bouncing dynamics. In the (m,n) mode, the drop bounces n times in m driving periods. The range of walkers considered in this work is indicated by the white line, as arises entirely within the chaotic walking regime.

oil [55]. For the parameters considered in the present work, walking droplets of this size are predicted and observed to have chaotic vertical dynamics (Fig. 5-1) [105], meaning that their natural vertical motion is aperiodic even in the absence of perturbations such as boundaries. Walkers of this particular size were selected as they exhibited an independence of the deflection angle α on the impact parameter y_i in certain parameter regimes, consistent with the observation of Couder & Fort [22]. Not all sizes of walking droplets displayed such an independence: y_i and α were strongly correlated for most parameters explored.

Away from boundaries, the walker executes rectilinear motion with a constant speed u_o that depends on the forcing and droplet size [91, 82]. After the droplet is deposited on the vibrating bath, the container is sealed with a transparent lid to isolate the system from ambient air currents while still allowing for clear visualization from above. Care was taken to avoid vibrational excitation of the lid. The walker is filmed at 10 frames per second, and tracked using a custom particle-tracking algorithm implemented in MATLAB.

Curved trajectories in the absence of barriers are an indication of air currents, non-uniform vibration, operating above the Faraday threshold, or interactions with the cell boundaries. Thus, a simple but critical test for reliable results is to send the walker across the cell in the absence of barriers (i.e. with any barriers removed) and check that it executes rectilinear motion. We have verified this to be the case in our system for all values of forcing considered.

Two barriers of breadth b = 6 mm are bolted to an aluminum base plate, the opening between them constituting the slit of width L = 14.7 mm = $3.1\lambda_F$ (Fig. 5-2). The slit geometry is thus as close as possible to that used by Couder & Fort [22], who used slits widths of 2.1 and $3.1\lambda_F$. We were obliged to estimate the depth of fluid above the barriers, which we set to $h_1 = 0.42 \pm 0.02$ mm, comparable to that used in previous experiments of walking droplets confined to a circular corral [64].

To demonstrate the potential importance of air currents in the diffraction experiments, we performed an experiment with a relatively large walker with and without the lid (Fig. 5-3). Enhanced divergence of pathlines is clearly present when the sys-

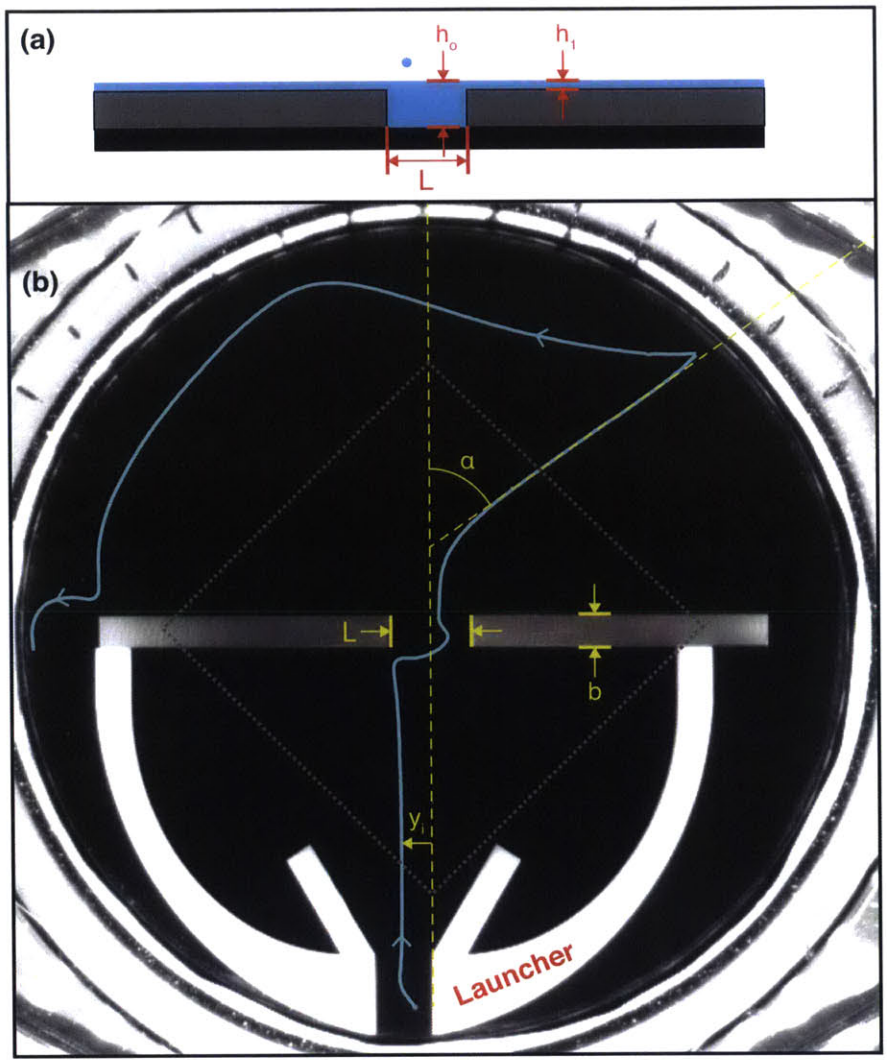

Figure 5-2: The experimental setup. (a) Side view of the submerged slit geometry. The depth in the bulk is h_o while that above the barriers is h_1. (b) View from above. The droplet launcher (white) directs the walker towards the slit of width L and breadth b with an impact parameter y_i, and is deflected by an angle α. The solid line is a sample trajectory. The dotted boundary indicates the size of the cell used in the single-slit experiments of Couder & Fort [22].

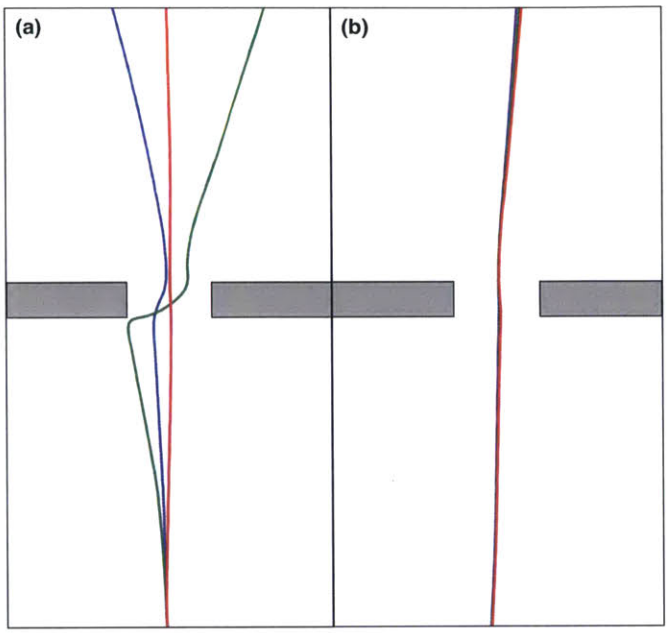

Figure 5-3: Trajectories of a walking droplet of diameter D = 0.80 mm passing through the slit. For both panels, the impact parameter and experimental parameters are the same, the forcing amplitude is γ/γ_F = 0.95, and the walker's free speed u_o = 12 mm/s. (a) Three trajectories with the same impact parameter without isolation from ambient air currents. (b) Eight trajectories after isolating the cell from air currents with a lid.

tem is not isolated. For smaller droplets, the walker is deviated more strongly, so that it rarely passes through the aperture. The sensitivity to ambient air currents is consistent with the fact that walking droplets are neutrally stable to lateral perturbations [85], so their direction of motion can be readily altered. It is now evident that isolation from air currents is a necessary requirement for repeatable experiments.

If the container is to be sealed, the walker must be autonomously and continuously guided towards the slit. For this purpose, we designed a droplet launcher, lying 1.2 mm beneath the free surface (Fig. 5-2b). It consists of a straight channel to first center the droplet in the launcher, and a diverging channel which gradually reduces the confinement so that the walker is not deflected as it exits the launcher. The impact parameter y_i, which we define as the position of the center of the droplet relative to the centerline of the slit as it exits the launcher, can be varied by shifting the launcher. A sample trajectory is shown in Fig. 5-2b. After passing through the slit, the walker's trajectory is deviated by an angle α, defined as the angle of the straightest consecutive

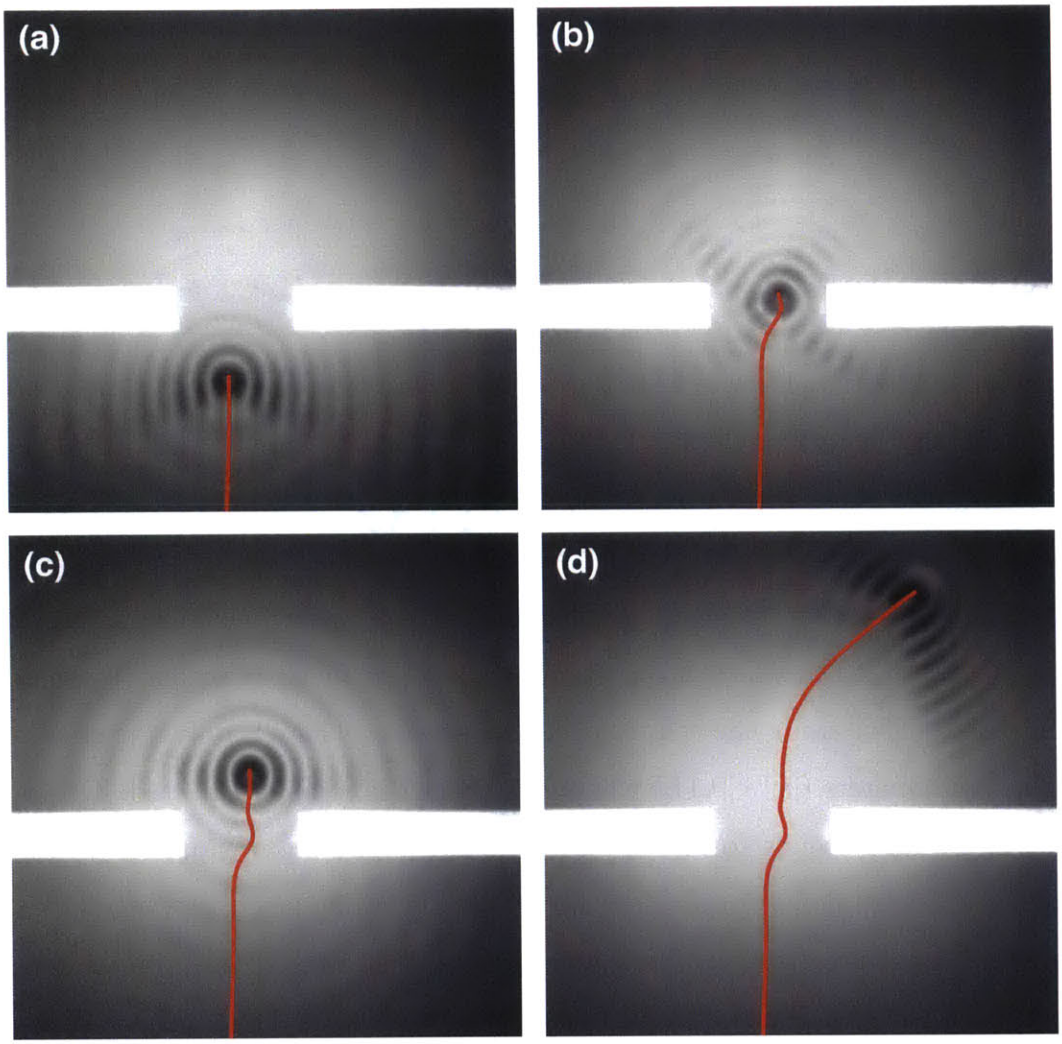

Figure 5-4: Visualization of the wave field as a walker passes through the single slit.

30 points (3 seconds) along the trajectory after the slit (identified as the segment with the maximum r^2 value of a fitted line). The measured angle is only weakly sensitive to the choice of number of points, with a maximum estimated measurement error of $\pm 1°$. After passing through the slit, the walker typically follows the outer boundary, reenters the launcher, and the process is repeated. The wave field generated by a walker in a typical passage of the slit is shown in Fig. 5-4. We proceed by assessing whether the pilot-wave dynamics can produce chaotic trajectories in the single-slit diffraction experiment.

5.2 Results

We first span the possible range of impact parameters for $\gamma/\gamma_F = 0.985$ and obtain the pattern shown in Fig. 5-5a. The incident "beam" is spread due to the spatial confinement. As the droplet approaches the slit, it drifts slightly towards the nearest barrier before receiving a lateral kick as it closes in. This pushes the droplet over the center line where it receives another kick, albeit weaker, as it approaches the opposing barrier. This mechanism acts to focus the incident walker towards the center of the slit, crossing the centerline in the process. There is only a narrow range of impact parameters ($|y_i| < 0.1L$) where the droplet is weakly deflected. Otherwise, the deflection angle tends to one of two preferred angles, approximately $\pm 55°$. The maximum observed deflection angle is $60°$. Note also that the entire range of impact parameters is not accessible in this experiment: for $|y_i| > 0.35L$, the walker does not pass through the slit, but is instead reflected back towards the launcher. When the walker does pass through the slit, the deflection angle depends continuously on the impact parameter, as evidenced in Fig. 5-5b. By fitting a continuous curve to this data, we can estimate the corresponding probability density function by assuming a uniform density of impact parameters (Fig. 5-6).

We proceed by fixing the impact parameter in order to isolate the dependence of the trajectories on the forcing amplitude (Fig. 5-7). Up to approximately $\gamma/\gamma_F = 0.990$ the behavior is as previously described: the impact parameter uniquely determines

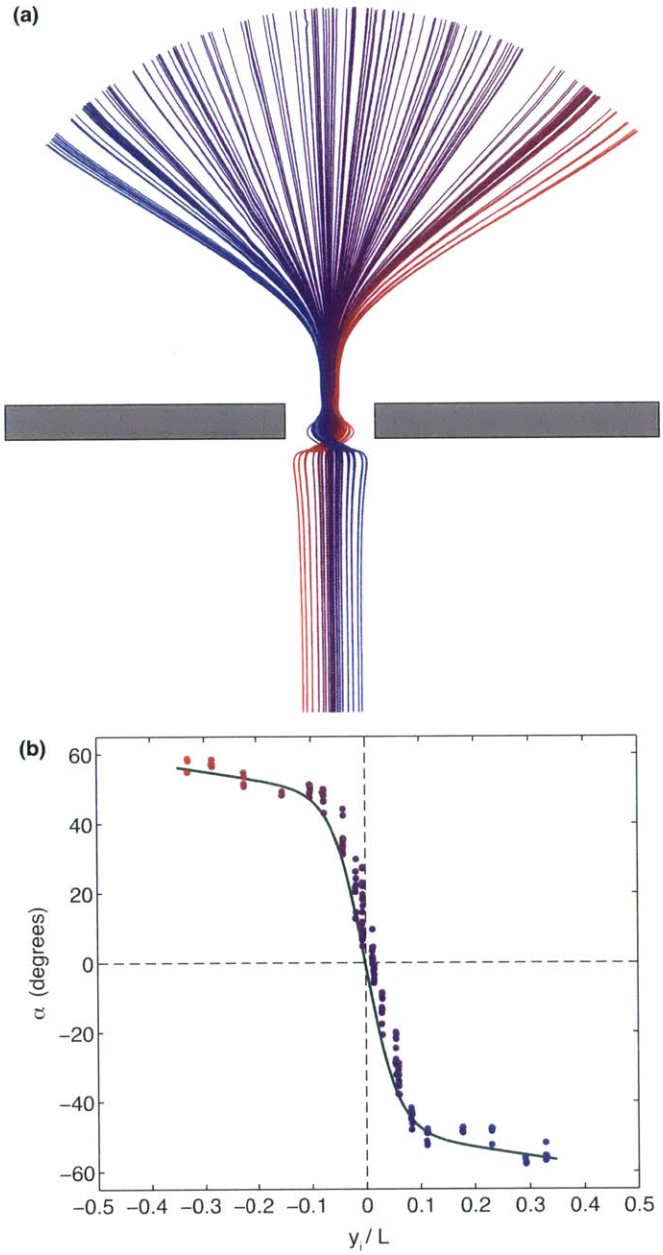

Figure 5-5: Non-chaotic trajectories. (a) Trajectories of a walking droplet passing through the slit with forcing $\gamma/\gamma_F = 0.985 \pm 0.002$ and free speed $u_o = 6.7 \pm 0.1$ mm/s. (b) Dependence of deflection angle α on the impact parameter y_i. The curve is a continuous approximation to the data.

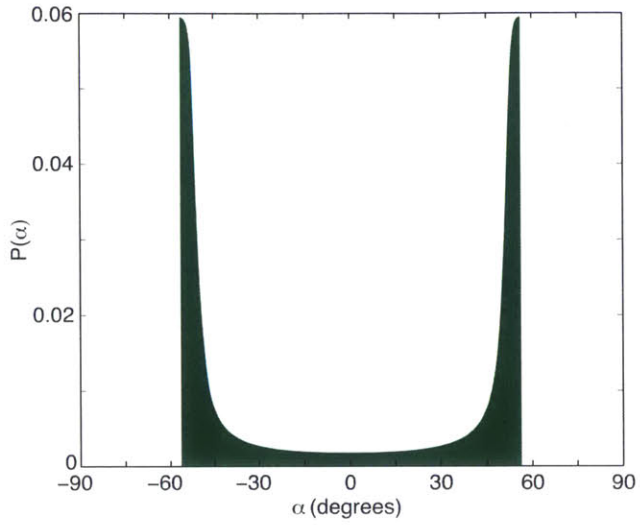

Figure 5-6: Probability density function corresponding to the fitted curve in Fig. 5-5b, based on the assumption of uniform density of impact parameters over the accessible range $|y_i| < 0.35$.

the deflection angle (Fig. 5-7a,b) which tends to increase with memory (Fig. 5-7e). As the Faraday threshold is approached, the behavior changes dramatically. At $\gamma/\gamma_F = 0.995$ (Fig. 5-7c), the walker is still deflected across the slit, but the deflection angle is no longer uniquely prescribed by the impact parameter. When $\gamma/\gamma_F = 0.998$ (Fig. 5-7d), deflection angles in the range $-60° < \alpha < 60°$ are obtained. The splaying of the pathlines after the slit is preceded by a damped lateral oscillation in the trajectory and visible disturbances to the vertical motion of the droplet. While the form of the incident trajectories is insensitive to the forcing amplitude, the outgoing trajectories evidently change dramatically as the Faraday threshold is approached.

At very high memory ($\gamma/\gamma_F = 0.998$) we vary the impact parameter uniformly over the accessible range in order to simulate a plane wave incident on the slit. Again, we see that the incident "beam" is spread as a result of the spatial confinement of the walker's guiding wave (Fig. 5-8a). A limiting deflection angle still exists: deflection angles greater than 65° were never observed. Once again, not all impact parameters were accessible: for $|y_i| > 0.35L$ the walker did not pass through the slit. However, there is no longer a simple relationship between the impact parameter and the deflection angle (Fig. 5-8b).

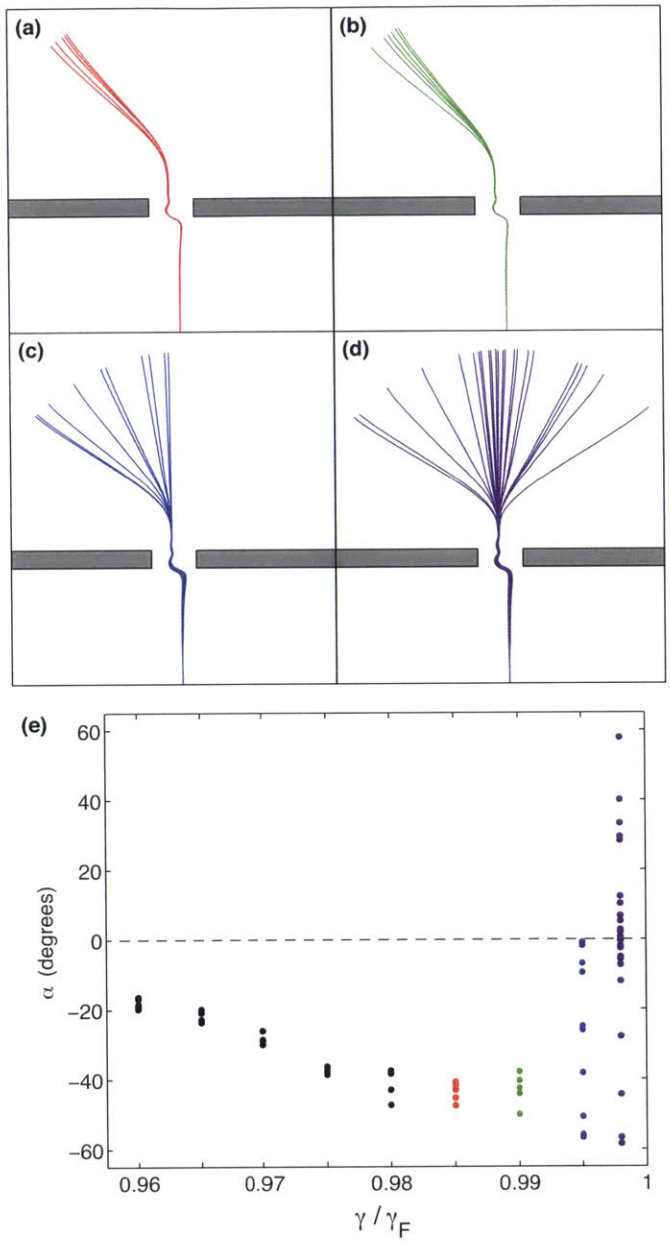

Figure 5-7: Trajectories of a walking droplet passing through the slit with fixed impact parameter $y_i = +0.17L$. (a) $\gamma/\gamma_F = 0.985$ and $u_o = 6.4$ mm/s, (b) $\gamma/\gamma_F = 0.990$ and $u_o = 6.6$ mm/s, (c) $\gamma/\gamma_F = 0.995$ and $u_o = 6.8$ mm/s, and (d) $\gamma/\gamma_F = 0.998$ and $u_o = 6.9$ mm/s. (e) Dependence of deflection angle α on γ/γ_F.

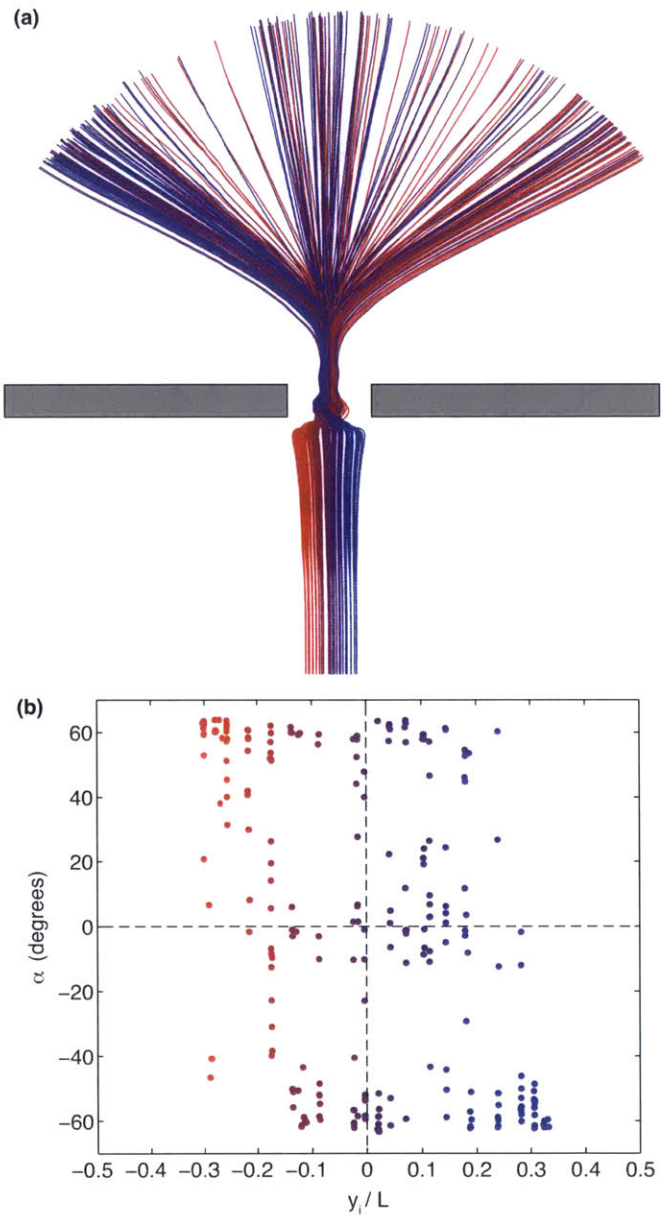

Figure 5-8: The chaotic regime. (a) Trajectories of a walking droplet passing through the slit with forcing $\gamma/\gamma_F = 0.998 \pm 0.002$ and free speed $u_o = 6.8 \pm 0.2$ mm/s. (b) Dependence of deflection angle α on the impact parameter y_i.

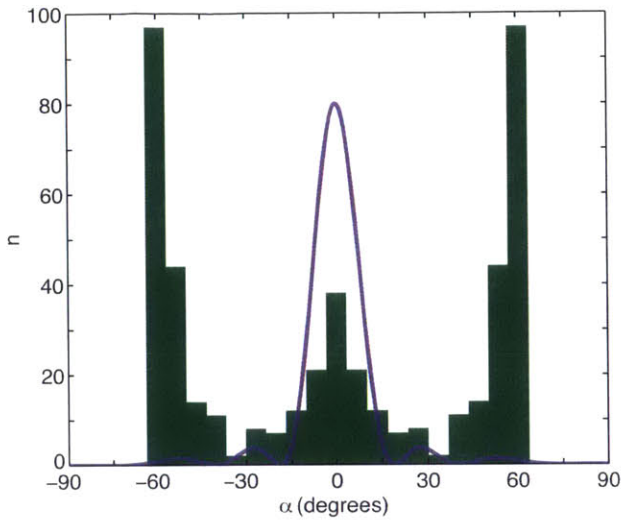

Figure 5-9: Symmetrized histogram of deflection angles of a droplet passing through the slit with forcing $\gamma/\gamma_F = 0.998 \pm 0.002$ and free speed $u_o = 6.8 \pm 0.2$ mm/s. Total number of independent trajectories $N_T = 235$. The curve is the far-field intensity pattern of a deflected plane wave with wavelength λ_F impinging on a slit of width L.

The statistical behavior of the walkers in this presumably chaotic regime is shown in Fig. 5-9. While some preferred angles do emerge, including a weak central peak, there is a dominance of large deflection angles, $\alpha \sim \pm 60°$. Thus, in both the chaotic and non-chaotic regimes, we observe a preference for large deflection angles near $50 - 60°$. We repeated the experiments with a reduced slit breadth ($b = 2$ mm) and observed very similar behavior; in particular, the same favored angle dominates the statistical distribution, and a limiting deflection angle exists.

To gain further insight, we considered the case of diffraction from a single edge (Fig. 5-10). For a range of impact parameters, walkers passing a single barrier also tend to be deflected by this same preferred angle. If released sufficiently far from the barrier's edge, the walkers continue along a straight path. It has also been noted that when a walker reflects from a submerged planar barrier it tends to be reflected at a fixed angle, approximately 55° [91, 44]. A comparable preferred angle emerges in each of these situations where a walker is moving away from a planar barrier. Understanding the origins of this preferred angle is the subject of ongoing work, as it appears to be a generic feature of walker-barrier interactions.

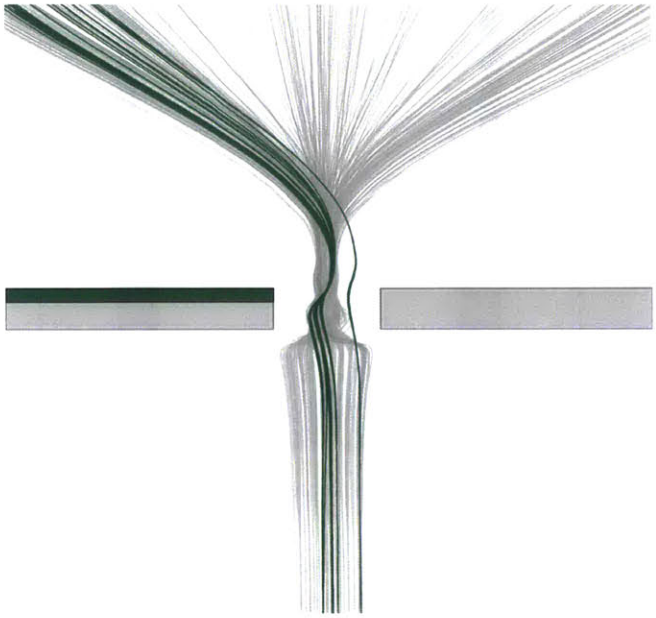

Figure 5-10: Dark lines show trajectories past a single barrier (green) of breadth $b = 2$ mm for $\gamma/\gamma_F = 0.990 \pm 0.002$ and $u_o = 6.8 \pm 0.2$ mm/s. The grey background represents the results from Fig. 5-8a.

5.3 Discussion

A walking droplet can be diverted owing to the spatial confinement of its guiding wave. We have explored the role of memory on the deflection of walking droplets and discovered a transition from regular to chaotic trajectories as the Faraday threshold is approached. In the non-chaotic regime, the deflection angle is uniquely prescribed by the impact parameter. In the chaotic regime, the deflection angle becomes unpredictable, with significant divergence of trajectories after passage through the slit. In both cases, a multimodal statistical pattern emerges as a result of the pilot-wave dynamics. However, neither of these statistical patterns corresponds to that expected for the diffraction of an incident plane wave. In each of the configurations investigated, including diffraction by a single edge, a preferred angle dominates the behavior, a poorly understood feature of walker-planar boundary interactions.

It is noteworthy that one system parameter is not controlled in our experiments, namely the phase of bouncing of the droplet as it enters the slit, or alternatively the locations of its impact points along its path. These locations will vary between

realizations, particularly for the vertically-chaotic walkers considered here, and we suspect that this hidden variable plays a critical role in the divergence of pathlines.

The statistical distribution obtained in our experiments (figure 5-9) is markedly different from that observed by Couder & Fort [22], who reported a pattern consistent with the diffraction of an incident plane wave. The reason for the discrepancy is not entirely clear, but we suspect it could be a result of the significantly smaller cell size used in the original experiments. In Fig. 5-2b, we show an outline of the geometry of the container used in the original experiments of Couder & Fort [22]. The sample trajectory demonstrates that the walker only settles into its rectilinear free motion outside this domain. This suggests that the measurements may have been influenced by interactions with the container boundaries. Furthermore, Couder & Fort [22] did not isolate their system from the environment, which suggests that some of the randomness apparent in their system, specifically, the independence of α and y_i, might be attributable to perturbations by air currents.

The presumably chaotic trajectories in our experiments are qualitatively different from those reported by Couder & Fort [22]. Most notably, we observed no significant divergence of trajectories before the slit, except when the walker was exposed to ambient air currents or if operating slightly above the Faraday threshold. Thus the uncertainty in the deflection angle is entirely due to the interaction with the complex wave field *after* the slit. The non-chaotic regime was not reported in the original experiments of Couder & Fort [22]; in each of their experiments, the deflection angle was independent of the impact parameter. Due to the lack of experimental parameters reported in Couder & Fort's experiments, it is impossible for us to assess whether or not they were operating in the chaotic regime.

The present study highlights the importance of experimental precision for reliable studies of walker diffraction. It also raises many questions. In particular, under what conditions might a quantum-like statistical pattern be possible in the walker system? Does the vertical phase of motion play a role in the observed divergence of pathlines and uncertainty in momentum? What is the physical origin of the preferred deflection angle?

Chapter 6

Conclusions

"A very small cause, which escapes us, determines a considerable effect which we cannot help seeing, and then we say that the effect is due to chance."

— *Henri Poincaré*

We have investigated three different configurations where a walker's trajectory is confined, either by boundaries or an external force. In each scenario considered, a similar progression of behaviors is observed as the memory increased. At low memory, regular trajectories are realized: given the system parameters and initial conditions, the outcome of each experiment is predictable. However, as the memory is increased progressively, these regular trajectories become unstable, and chaotic trajectories emerge. The position of a walker in the corral, the orbital radius of a walker in a rotating frame, or the deflection angle of a walker passing through an aperture is then best described in terms of a multimodal statistical distribution that is underlaid by a chaotic pilot-wave dynamics.

The detailed characterization of the dynamics in each of these configurations was made possible by our experimental advances. In particular, we have designed and implemented a precision vibration system, which greatly improves the spatial uniformity of the vertical vibration amplitude, as is critical to investigations at high memory. The experimental advances may also find application in other fields where shakers

are used and uniaxial vibration is required. The behavior of the droplets is extremely sensitive to their size; consequently, reproducible results require a method for generating uniform droplets on demand. To that end, we have designed a simple, low-cost piezoelectric droplet generator. Furthermore, we have demonstrated the sensitivity of the walker dynamics to external perturbations and established the importance of isolating the system from ambient air currents with a lid. This necessitated the design of a series of launchers, used to direct the walker towards obstacles continuously.

One remaining uncontrolled experimental variable is the temperature of the bath. The bath tends to heat up during use owing to viscous dissipation and heating from the light source. The result is a gradual lowering of the Faraday threshold. Currently, we opt to measure the threshold regularly, and adjust the forcing amplitude γ such that the relative forcing amplitude γ/γ_F remains constant. However, the vertical dynamics of the walker are sensitive to γ/g as well as γ/γ_F, so this method may not be adequate in certain circumstances. The experiments could be further refined by maintaining a constant bath temperature.

We have characterized the transition from stable to chaotic trajectories most extensively in the rotating system, which provides a framework for understanding the generic emergence of multimodal statistics in this pilot-wave system. At low memory, we demonstrated that all orbital radii were accessible, while at intermediate memories only a range of orbital radii could be accessed, owing to the dynamic constraint imposed on the droplet by its structured wave field. As the memory was increased further, the previously stable orbits give way to oscillating orbits of increasing complexity through a period-doubling bifurcation. As the Faraday threshold is approached, a chaotic switching between the unstable orbital levels is observed, the result being a multimodal statistical pattern describing the orbital radius.

A similar chaotic switching between unstable orbits at high memory was also observed in the circular corral experiments, and for a walker confined to a harmonic potential [89], in each case giving rise to multimodal statistics. These results are interesting to consider in light of a recent simplified model of walkers in confinement [53]. Gilet reduces the motion of the walker in a confined geometry to a 2D iterative

map, tracking both the position of the walker along a line and the amplitude of a single cavity wave mode. The equations for the position and wave are coupled in order to capture a critical feature of the experiment: the droplet moves through the influence of the slope of the wave field, and the wave field is generated by the droplet's impacts with the surface. The bifurcation parameter considered in his study is the system memory. He finds that at low memory, stable fixed points exist, which correspond to stable orbital solutions. As the memory is increased, the walker begins to oscillate about the previously stable fixed points, which can be viewed as the equivalent of wobbling orbits. Eventually, as the memory is further increased, the walker transitions to a chaotic regime in which it explores the entire cavity, spending most of its time near the anti-nodes of the cavity mode, as was observed in the circular corral experiments. The probability distribution of walker position obtained in the chaotic regime is thus related to the cavity wave mode. The emergence of multimodal statistics from the instability of quantized solutions seems to be a generic feature of this hydrodynamic pilot-wave system.

6.1 Future directions

Many of the experiments in the walker system, including tunneling, confinement to corrals, and single-particle diffraction, involve the interaction of walkers with submerged barriers. Presently, very little is understood about the fundamentals of such interactions, even in the simplest geometries. Before embarking on explorations of more complex geometries, it would be valuable to investigate the simple reflection of a walker from a planar barrier. As discussed in chapter 5, preliminary evidence suggests that a preferred reflection angle exists, that is largely independent of the approach to the barrier. The mechanism by which this particular angle is selected, and how it depends on the system parameters remain open questions and could provide critical insight into the next generation of theoretical models of walker-barrier interactions.

We have demonstrated that the single-slit experiments are dominated by a wall effect, whereby the majority of the droplets are deflected at a fixed angle to the planar

boundary. This angle does not seem to be a result of the diffraction of the incident pilot-wave, but is rather related to the interaction of the walker with its wave field as it leaves a planar barrier. In order to obtain a more wave-like diffraction pattern of walkers, the influence of this peculiar effect needs to be minimized in some manner. An alternative experiment would involve replacing the slit geometry with a pair of submerged pillars, through which the walker passes. In this case, the incident waves will be diffracted by the confinement, but the dominance of the planar wall effect will be eliminated. Some curious preliminary results on the interaction of a walker with a single submerged cylinder are presented in Appendix A.

The corral experiments should also be revisited given our new intuition on the transition to chaos and emergence of multimodal statistics in this system. In particular, a more careful characterization of the effect of memory should be conducted for the circular corral. We suspect that *stable* quantized orbits can be found at intermediate memories, which then become unstable prior to the transition to chaos. This system could then be compared more closely to the model of Gilet [53]. A circular corral with a non-axisymmetric cavity mode or other simple corrals geometries such as squares or ellipses could also be considered, along with more exotic corral geometries. For example, scarring has been observed in the Faraday wave pattern of stadium shaped cavities [72]. It would be interesting to see if scars also exist in the probability distribution of walkers confined to such cavities.

The tunneling experiments of Eddi *et al.* [44] should also be revisited, with particular attention given to the influence of memory on the tunneling probability. As was demonstrated in this thesis, the behavior of the walkers is remarkably sensitive to the forcing amplitude, a parameter not considered in the original experiments [44]. We suspect that at low memory, the walker will cross the barrier with either probability one or zero, with the behavior becoming chaotic only at very high memories.

We hope this work will serve as a useful guide to those interested in careful experimental investigations of hydrodynamic quantum analogues. The system, while conceptually simple, is extremely sensitive to the system parameters and thus careful control is necessary for repeatable results. Undoubtedly, further analogies with

quantum mechanics will be developed with the bouncing droplet system. Our hope is that this system will inspire further explorations into the possibility of a chaotic pilot-wave dynamics underlying quantum statistics.

"If you want to find the secrets of the universe, think in terms of energy, frequency and vibration."

— *Nikola Tesla*

Appendix A

Scattering and the logarithmic spiral

A.1 Scattering experiment

With a view to gaining insight into walker-barrier interactions, we here consider the trajectory of a walker directed towards a submerged cylindrical barrier. This was originally investigated by a summer intern in our lab, Alexis Page, who found that for most parameters, the walker was scattered as it approached the pillar, as show in figure A-1. However, recent experiments conducted at the higher memory values attainable with our refined experimental setup have revealed spiral trajectories with two key features, constant radial velocity and constant overall speed, as demonstrated in figure A-2. We first derive the parametric equations of these spiral trajectories.

A.1.1 Derivation of parametric equations

Guided by our experimental observations, we make the two assumptions that the radial velocity (v_r) and the speed ($|v|$) are constant when in the spiral. The velocity vector can be written in polar coordinates as

$$\mathbf{v} = v_r\widehat{e}_r + v_\theta\widehat{e}_\theta = v_r\widehat{e}_r + r\dot{\theta}\widehat{e}_\theta. \tag{A.1}$$

So v_θ must be constant, since $|v|$ and v_r are constant and

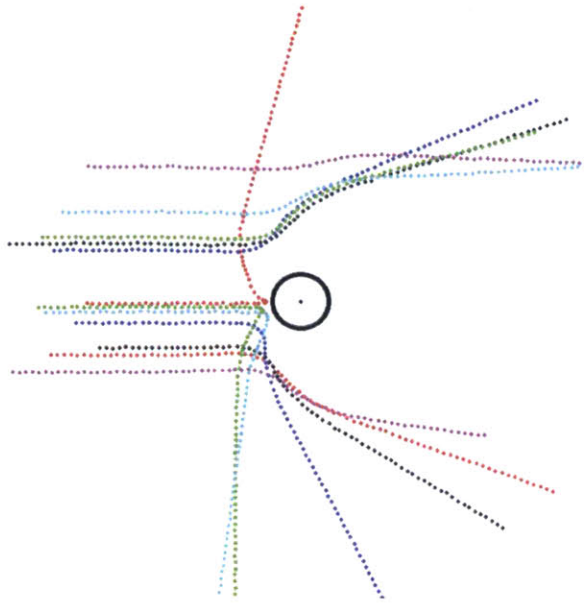

Figure A-1: Scattering past a submerged cylinder for various impact parameters. Experimental parameters were γ/γ_F = 0.97, depth above impactor h_1 = 1.30 mm, radius of impactor R = 2.5 mm, and free speed of the walker u_o = 10.1 mm/s. Figure from report by Alexis Page.

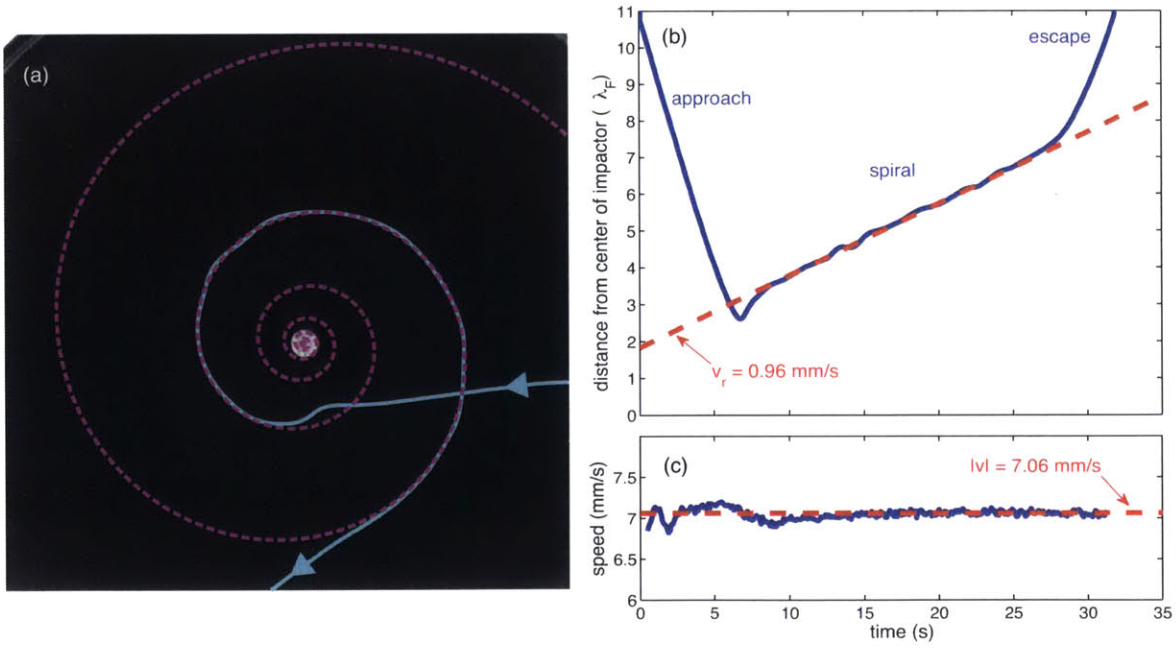

Figure A-2: A logarithmic spiral observed for experimental parameters γ/γ_F = 0.995, depth above impactor h_1 = 0.46 mm, and radius of impactor R = 2.5 mm. (a) Trajectory (solid) with best fit logarithmic spiral (dashed). (b) Distance from center of impactor with time indicates a linear increase during the spiral region, a radial velocity of v_r = 0.96 mm/s. (c) The dependence of droplet speed on time, indicating near constant speed, $|\mathbf{v}|$ = 7.06 mm/s, during and beyond the spiral region.

$$v_\theta = \pm\sqrt{|\mathbf{v}|^2 - v_r^2}. \tag{A.2}$$

We can write $r(t)$ as

$$r(t) = v_r t + r_o. \tag{A.3}$$

Combining the above yields

$$\dot{\theta}(t) = \frac{v_\theta}{r} = \frac{v_\theta}{v_r t + r_o}. \tag{A.4}$$

Integrating for $v_r \neq 0$ yields

$$\theta(t) = \frac{v_\theta \ln(v_r t + r_o)}{v_r} + \theta_o. \tag{A.5}$$

Rearranging and taking the exponential of both sides we find that

$$v_r t + r_o = e^{\frac{v_r}{v_\theta}(\theta - \theta_o)}. \tag{A.6}$$

Substituting this into equation (A.3) we find

$$r(\theta) = e^{\frac{v_r}{v_\theta}(\theta - \theta_o)} = e^{\pm\frac{v_r}{\sqrt{|\mathbf{v}|^2 - v_r^2}}(\theta - \theta_o)} \tag{A.7}$$

which is the parametric equation for a logarithmic spiral. Here we have demonstrated that if both the radial velocity and droplet speed are constant, then the resulting trajectory is a logarithmic spiral. We thus fit a spiral to our trajectory by the single unknown parameter, the phase shift θ_o, which simply rotates the spiral. The sign of the exponent determines the handedness of the spiral. A logarithmic spiral can be characterized by a constant pitch angle ϕ, which can also be computed directly from the known quantities:

$$\tan\phi = \frac{v_r}{\sqrt{|\mathbf{v}|^2 - v_r^2}}. \tag{A.8}$$

Note that as $v_r \to 0$, $\phi \to 0$ (corresponding to circular motion), and when $|\mathbf{v}| = v_r$, $\phi = \pi/2$ (corresponding to purely radial motion). For the experimental conditions in Figure 1, the spiral has an outward pitch angle of 7.8°.

A.2 Effective force of pillar

What is the effective force generated by the pillar that would give rise to a logarithmic spiral? We begin with boost equation for walking droplets valid in the weak-acceleration limit [18]:

$$\frac{\mathrm{d}}{\mathrm{d}t}\left(m\gamma_B\dot{\mathbf{x}}\right) + D_w\dot{\mathbf{x}} = \mathbf{F}, \tag{A.9}$$

where $\gamma_B = 1 + \frac{gAk_F^2T_M^3}{2T_F(1+(k_FT_M|\mathbf{v}|)^2)^{3/2}}$ and $D_w = D\left[1 - \frac{mgA}{DT_F|\mathbf{v}|^2}\left(1 - \frac{1}{\sqrt{1+(k_FT_M|\mathbf{v}|)^2}}\right)\right]$ which depend only on the experimental parameters and $|\mathbf{v}| = |\dot{\mathbf{x}}|$. Use of the boost equation is justified for the case of orbital dynamics if the characteristic orbital time scale is much less than the memory time, $T_{orb} \gg T_M$. Thus the orbiting walker does not interact with its own wake. A typical orbital time scale T_{orb} for the current system can be defined as:

$$T_{orb} = \frac{2\pi r}{u_0} = 2\pi\frac{15-35\text{ mm}}{7\text{ mm/s}} = 13.5 - 31.4\text{ s}. \tag{A.10}$$

In the experimental parameter regime, the typical memory time is T_M:

$$T_M = \frac{T_d}{1-\gamma/\gamma_F} = \frac{0.0174\text{ s}}{1-0.995} = 3.5\text{ s}. \tag{A.11}$$

So $T_{orb} \gg T_M$, and the boost equation should provide an adequate description of the observed logarithmic spiral. If the walker is moving at a constant speed equal to its free walking speed, $|\mathbf{v}| = u_o$, as in the case of the observed logarithmic spiral, the boost equation simplifies to:

$$m\gamma_B\ddot{\mathbf{x}} = \mathbf{F}, \tag{A.12}$$

This can be written in polar coordinates as:

$$\widehat{e}_r: \quad m\gamma_B(\ddot{r} - r\dot{\theta}^2) = F_r \tag{A.13}$$

$$\widehat{e}_\theta: \quad m\gamma_B(r\ddot{\theta} + 2\dot{r}\dot{\theta}) = F_\theta \tag{A.14}$$

We propose a solution of the form of the logarithmic spiral found in section A.1.1:

$$r(t) = v_r t + r_o, \quad \dot{r}(t) = v_r, \quad \ddot{r}(t) = 0. \tag{A.15}$$

$$\theta(t) = \frac{v_\theta \ln(v_r t + r_o)}{v_r} + \theta_o, \quad \dot{\theta}(t) = \frac{v_\theta}{v_r t + r_o}, \quad \ddot{\theta}(t) = -\frac{v_\theta v_r}{(v_r t + r_o)^2}. \tag{A.16}$$

Substituting these into the radial and azimuthal equations gives:

$$F_r = -\frac{m\gamma_B v_\theta^2}{r} \tag{A.17}$$

$$F_\theta = \frac{m\gamma_B v_r v_\theta}{r} \tag{A.18}$$

So the effective force field from the pillar decays in magnitude like $1/r$ and has both radial and azimuthal components:

$$\mathbf{F} = \frac{m\gamma_B}{r}\left(-v_\theta^2\widehat{e}_r + v_\theta v_r \widehat{e}_\theta\right) = \frac{m\gamma_B v_\theta}{r}\left(\widehat{e}_z \times \mathbf{v}\right). \tag{A.19}$$

We note that $\mathbf{F} \cdot \mathbf{v} = 0$; thus, the effective force always acts normal to the direction of motion of the walker. The radial component is always attractive, while the direction of the azimuthal component depends on the relative signs of v_θ and v_r. The relative magnitudes of the azimuthal to radial components evidently scales like v_r/v_θ, which is small for the observed spiral; thus, the dominant effect of the pillar-induced wave field is an attractive radial force. Our continuing investigation of scattering from a pillar will provide valuable insight and so guide the development of theoretical models of walker-boundary interactions.

Bibliography

[1] A. Andersen, J. Madsen, C. Reichelt, S. R. Ahl, B. E. Lautrup, C. S. Ellegaard, M. Levinsen, and T. Bohr. Comment on Y. Couder and E. Fort: Single-particle diffraction and interference at a macroscopic scale; Phys. Rev. Lett. 97, 154101 (2006). *arXiv.org: Physics*, 1405.0466v1, 2014.

[2] I. A. Anderson. Avoiding stinger rod resonance effects on small structures. In *Proceedings of the 8th International Modal Analysis Conference*, pages 673–678, 1990.

[3] I. S. Aranson, D. Volfson, and L. S. Tsimring. Swirling motion in a system of vibrated elongated particles. *Phys. Rev. E*, 75(5):051301, 2007.

[4] J. Bechhoefer, B. Ego, S. Manneville, and B. Johnson. An experimental study of the onset of parametrically pumped surface waves in viscous fluids. *J. Fluid Mech.*, 288:325–350, 1995.

[5] T. B. Benjamin and F. Ursell. The stability of the plane free surface of a liquid in vertical periodic motion. *Proc. Roy. Soc. A*, 225:505–515, 1954.

[6] L. M. Berliner. Statistics, probability and chaos. *Statistical Science*, pages 69–90, 1992.

[7] T. Besson, W. S. Edwards, and L. S. Tuckerman. Two-frequency parametric excitation of surface waves. *Phys. Rev. E*, 54(1):507, 1996.

[8] R. E. D. Bishop and D. C. Johnson. *The mechanics of vibration.* 1960.

[9] R. D. Blevins. *Formulas for Natural Frequency and Mode Shape.* Van Nostrand Reinhold, 1979.

[10] D. Bohm. A suggested interpretation of the quantum theory in terms of hidden variables. *Phys. Rev.*, 85:166–179, 1952.

[11] N. Bohr. Can quantum-mechanical description of physical reality be considered complete? *Phys. Review*, 48:696–702, 1935.

[12] A. Bokaian. Natural frequencies of beams under compressive axial loads. *Journal of Sound and Vibration*, 126(1):49–65, 1988.

[13] R. W. Bono and E. J. Seller. The effect of high transverse inputs on accelerometer calibration. *Cal Lab-International Journal of Metrology*, 18(1):31, 2011.

[14] C. Borghesi, J. Moukhtar, M. Labousse, A. Eddi, E. Fort, and Y. Couder. Interaction of two walkers: Wave-mediated energy and force. *Phys. Rev. E*, 90(6):063017, 2014.

[15] A. Boudaoud, E. Hamm, and F. Melo. Developable modes in vibrated thin plates. *Phys. Rev. Lett.*, 99(25):254301, 2007.

[16] J. W. M. Bush. Quantum mechanics writ large. *PNAS*, 107(41):17455–17456, 2010.

[17] J. W. M. Bush. Pilot-wave hydrodynamics. *Ann. Rev. of Fluid Mech.*, 47:269–292, 2015.

[18] J. W. M. Bush, A. U. Oza, and J. Moláček. The wave-induced added mass of walking droplets. *Journal of Fluid Mechanics*, 755:R7, 2014.

[19] J. C. Butcher. *Numerical methods for ordinary differential equations.* John Wiley & Sons, second edition.

[20] R. Carmigniani, S. Lapointe, S. Symon, and B. J. McKeon. Influence of a local change of depth on the behavior of walking oil drops. *Exp. Thermal Fluid Sci.*, 54:237–246, 2014.

[21] D. Cloutier, P. Avitabile, R. Bono, and M. Peres. Shaker/stinger effects on measured frequency response functions. In *Proceedings of the 27th International Modal Analysis Conference*, pages 9–12, 2009.

[22] Y. Couder and E. Fort. Single particle diffraction and interference at a macroscopic scale. *Phys. Rev. Lett.*, 97:154101, 2006.

[23] Y. Couder and E. Fort. Probabilities and trajectories in a classical wave-particle duality. In *J. Phys.: Conf. Series*, volume 361, page 012001. IOP Publishing, 2012.

[24] Y. Couder, E. Fort, C.H. Gautier, and A. Boudaoud. From bouncing to floating: non-coalescence of drops on a fluid bath. *Phys. Rev. Lett.*, 94:177801, 2005.

[25] Y. Couder, S. Protière, E. Fort, and A. Boudaoud. Walking and orbiting droplets. *Nature*, 437:208, 2005.

[26] M. F. Crommie, C. P. Lutz, and D. M. Eigler. Confinement of electrons to quantum corrals on a metal surface. *Science*, 262:218–220, 1993.

[27] M. F. Crommie, C. P. Lutz, and D. M. Eigler. Imaging standing waves in a two-dimensional electron gas. *Nature*, 363:524–527, 1993.

[28] C. Davisson and L. H. Germer. The scattering of electrons by a single crystal of nickel. *Nature*, 119(2998):558–560, 1927.

[29] Z. A. Daya, E. Ben-Naim, and R. E. Ecke. Experimental characterization of vibrated granular rings. *The European Physical Journal E*, 21(1):1–10, 2006.

[30] L. de Broglie. *Recherches sur la théorie des Quanta.* PhD thesis, Paris, France, 1924.

[31] L. de Broglie. *Ondes et mouvements.* Gautier Villars, Paris, 1926.

[32] L. de Broglie. Interpretation of quantum mechanics by the double solution theory. *Annales de la Fondation Louis de Broglie*, 12:1–23, 1987.

[33] J. R. de Bruyn, B. C. Lewis, M. D. Shattuck, and H. L. Swinney. Spiral patterns in oscillated granular layers. *Phys. Rev. E*, 63:041305, 2001.

[34] J. Deseigne, O. Dauchot, and H. Chaté. Collective motion of vibrated polar disks. *Phys. Rev. Lett.*, 105(9):098001, 2010.

[35] J. Deseigne, S. Léonard, O. Dauchot, and H. Chaté. Vibrated polar disks: spontaneous motion, binary collisions, and collective dynamics. *Soft Matter*, 8(20):5629–5639, 2012.

[36] J. A. Dijksman and M. van Hecke. The role of tap duration for the steady-state density of vibrated granular media. *Europhys. Lett.*, 88(4):44001, 2009.

[37] J. A. Dijksman, G. H. Wortel, L. T. H. van Dellen, O. Dauchot, and M. van Hecke. Jamming, yielding, and rheology of weakly vibrated granular media. *Phys. Rev. Lett.*, 107(10):108303, 2011.

[38] T. Dimoff and B. F. Payne. Application of air bearings to an electrodynamic vibration standard. *Journal of Research of the National Bureau of Standards*, 67(4):327–333, 1963.

[39] Y. Ding and P. Umbanhowar. Enhanced faraday pattern stability with three-frequency driving. *Phys. Rev. E*, 73(4):046305, 2006.

[40] J. Dosch. Air bearing shaker for precision calibration of accelerometers. In *Proceedings of the 24th International Modal Analysis Conference*, 2006.

[41] S. Douady. Experimental study of the Faraday instability. *J. Fluid Mech.*, 221:383–409, 1990.

[42] A. Eddi, A. Boudaoud, and Y. Couder. Oscillating instability in bouncing droplet crystals. *Europhysics Letters*, 94(2):20004, 2011.

[43] A. Eddi, A. Decelle, E. Fort, and Y. Couder. Archimedean lattices in the bound states of wave interacting particles. *Europhysics Letters*, 87(5):56002, 2009.

[44] A. Eddi, E. Fort, F. Moisy, and Y. Couder. Unpredictable tunneling of a classical wave-particle association. *Phys. Rev. Lett.*, 102:240401, 2009.

[45] A. Eddi, J. Moukhtar, S. Perrard, E. Fort, and Y. Couder. Level splitting at macroscopic scale. *Phys. Rev. Lett.*, 108:264503, 2012.

[46] A. Eddi, E. Sultan, J. Moukhtar, E. Fort, M. Rossi, and Y. Couder. Information stored in Faraday waves: the origin of path memory. *J. Fluid Mech.*, 675:433–463, 2011.

[47] A. Eddi, D. Terwagne, E. Fort, and Y. Couder. Wave propelled ratchets and drifting rafts. *Europhysics Letters*, 82(4):44001, 2008.

[48] A. Einstein, B. Podolsky, and N. Rosen. Can quantum-mechanical description of physical reality be considered complete? *Phys. Review*, 47:777–780, 1935.

[49] D. J. Ewins. *Modal testing: theory, practice and application.* Research Studies Press, Baldock, Hertforshire, England, 2000.

[50] M. Faraday. On the forms and states of fluids on vibrating elastic surfaces. *Philos. Trans. R. Soc. London*, 121:319–340, 1831.

[51] G. A. Fiete and E. J. Heller. Theory of quantum corrals and quantum mirages. *Rev. Mod. Phys.*, 75:933–948, 2003.

[52] E. Fort, A. Eddi, A. Boudaoud, J. Moukhtar, and Y. Couder. Path-memory induced quantization of classical orbits. *Proc. Nat. Acad. Sci.*, 107(41):17515–17520, 2010.

[53] T. Gilet. Dynamics and statistics of wave-particle interactions in a confined geometry. *Physical Review E*, 90(5):052917, 2014.

[54] T. Gilet and J. W. M. Bush. The fluid trampoline: droplets bouncing on a soap film. *J. Fluid Mech.*, 625:167–203, 2009.

[55] T. Gilet and J. W. M. Bush. Droplets bouncing on a wet, inclined surface. *Physics of Fluids*, 24(12):122103, 2012.

[56] T. Gilet and J.W.M. Bush. Chaotic bouncing of a drop on a soap film. *Phys. Rev. Lett*, 102:014501:1–4, 2009.

[57] T. Gilet, D. Terwagne, N. Vandewalle, and S. Dorbolo. Dynamics of a bouncing droplet onto a vertically vibrated interface. *Phys. Rev. Lett.*, 100(16):167802, 2008.

[58] D. I. Goldman. *Pattern formation and fluidization of vibrated granular layers, and grain dynamics and jamming in a water fluidized bed.* PhD thesis, University of Texas at Austin, Austin, TX, August 2002.

[59] C. L. Goodridge, W. T. Shi, and D. P. Lathrop. Threshold dynamics of singular gravity-capillary waves. *Phys. Rev. Lett.*, 76(11):1824, 1996.

[60] N. Gravish, S. V. Franklin, D. L. Hu, and D. I. Goldman. Entangled granular media. *Phys. Rev. Lett.*, 108(20):208001, 2012.

[61] D. M. Harris and J. W. M. Bush. Droplets walking in a rotating frame: from quantized orbits to multimodal statistics. *J. Fluid Mech.*, 739:444–464, 2014.

[62] D. M. Harris and J. W. M. Bush. Generating uniaxial vibration with an electrodynamic shaker and external air bearing. *Journal of Sound and Vibration*, 334:255–269, 2015.

[63] D. M. Harris, T. Liu, and J. W. M. Bush. A low-cost, precise piezoelectric droplet-on-demand generator. *Experiments in Fluids*, 56:83, 2015.

[64] D. M. Harris, J. Moukhtar, E. Fort, Y. Couder, and J. W. M. Bush. Wavelike statistics from pilot-wave dynamics in a circular corral. *Phys. Rev. E*, 88:011001, 2013.

[65] D. M. Henderson and J. W. Miles. Single-mode faraday waves in small cylinders. *Journal of Fluid Mechanics*, 213:95–109, 1990.

[66] G. M. Hieber. Non-toxic stingers. In *Proceedings of the 6th International Modal Analysis Conference*, pages 1371–1379, 1988.

[67] P.R. Holland. *The quantum theory of motion: An account of the de Broglie-Bohm causal interpretation of quantum mechanics.* Cambridge University Press, Cambridge, UK, 1993.

[68] P. J. Holmes. The dynamics of repeated impacts with a sinusoidally vibrating table. *Journal of Sound and Vibration*, 84(2):173–189, 1982.

[69] C. Huepe, Y. Ding, P. Umbanhowar, and M. Silber. Forcing function control of faraday wave instabilities in viscous shallow fluids. *Phys. Rev. E*, 73(1):016310, 2006.

[70] ISO. Methods for the calibration of vibration and shock transducers – Part 21: Vibration calibration by comparison to a reference transducer. ISO 16063-21:2003, International Organization for Standardization, Geneva, Switzerland, 2003.

[71] H. P. Kavehpour. Coalescence of drops. *Annu. Rev. Fluid Mech.*, 47:245, 2015.

[72] A. Kudrolli, M. C. Abraham, and J. P. Gollub. Scarred patterns in surface waves. *Phys. Rev. E*, 63(2):026208, 2001.

[73] A. Kudrolli and J. P. Gollub. Patterns and spatiotemporal chaos in parametrically forced surface waves: a systematic survey at large aspect ratio. *Physica D: Nonlinear Phenomena*, 97(1):133–154, 1996.

[74] K. Kumar. Linear theory of Faraday instability in viscous fluids. *Proceedings of the Royal Society A*, 452:1113–1126, 1996.

[75] M. Labousse and S. Perrard. Non-hamiltonian features of a classical pilot-wave dynamics. *Physical Review E*, 90(2):022913, 2014.

[76] M. Labousse, S. Perrard, Y. Couder, and E. Fort. Build-up of macroscopic eigenstates in a memory-based constrained system. *New Journal of Physics*, 16(11):113027, 2014.

[77] G. F. Lang. Electrodynamic shaker fundamentals. *Sound and Vibration*, 31(4):14–23, 1997.

[78] G. F. Lang and D. Snyder. Understanding the physics of electrodynamic shaker performance. *Sound and Vibration*, 35(10):24–33, 2001.

[79] J. Miles and D. Henderson. Parametrically forced surface waves. *Ann. Rev. of Fluid Mech.*, 22:143–165, 1990.

[80] S. T. Milner. Square patterns and secondary instabilities in driven capillary waves. *Journal of Fluid Mechanics*, 225:81–100, 1991.

[81] J. Moláček and J. W. M. Bush. Drops bouncing on a vibrating bath. *J. Fluid Mech.*, 727:582–611, 2013.

[82] J. Moláček and J. W. M. Bush. Drops walking on a vibrating bath: Towards a hydrodynamic pilot-wave theory. *J. Fluid Mech.*, 727:612–647, 2013.

[83] V. Narayan, S. Ramaswamy, and N. Menon. Long-lived giant number fluctuations in a swarming granular nematic. *Science*, 317(5834):105–108, 2007.

[84] A. U. Oza, D. M. Harris, R. R. Rosales, and J. W. M. Bush. Pilot-wave dynamics in a rotating frame: on the emergence of orbital quantization. *J. Fluid Mech.*, 744:404–429, 2014.

[85] A. U. Oza, R. R. Rosales, and J. W. M. Bush. A trajectory equation for walking droplets: hydrodynamic pilot-wave theory. *J. Fluid Mech.*, 737:552–570, 2013.

[86] A. U. Oza, Ø. Wind-Willassen, D. M. Harris, R. R. Rosales, and J. W. M. Bush. Pilot-wave hydrodynamics in a rotating frame: exotic orbits. *Physics of Fluids*, 26(8):082101, 2014.

[87] H. K. Pak, E. Van Doorn, and R. P. Behringer. Effects of ambient gases on granular materials under vertical vibration. *Phys. Rev. Lett.*, 74:4643–4646, Jun 1995.

[88] M. A. Peres, R. W. Bono, and D. L. Brown. Practical aspects of shaker measurements for modal testing. In *Proceedings of ISMA 2010*, pages 2539–2551, 2010.

[89] S. Perrard, M. Labousse, E. Fort, and Y. Couder. Chaos driven by interfering memory. *Physical Review Letters*, 113(10):104101, 2014.

[90] S. Perrard, M. Labousse, M. Miskin, E. Fort, and Y. Couder. Self-organization into quantized eigenstates of a classical wave-driven particle. *Nature Comm.*, 5, 2014.

[91] S. Protière, A. Boudaoud, and Y. Couder. Particle-wave association on a fluid interface. *J. Fluid Mech.*, 554:85–108, 2006.

[92] S. Protière, Y. Couder, E. Fort, and A. Boudaoud. The self-organization of capillary wave sources. *Journal of Physics: Condensed Matter*, 17(45):S3529, 2005.

[93] P. M. Reis, R. A. Ingale, and M. D. Shattuck. Forcing independent velocity distributions in an experimental granular fluid. *Phys. Rev. E*, 75:051311, 2007.

[94] G. P. Ripper, R. S. Dias, and G. A. Garcia. Primary accelerometer calibration problems due to vibration exciters. *Measurement*, 42(9):1363–1369, 2009.

[95] W. T. Shi, C. L. Goodridge, and D. P. Lathrop. Breaking waves: bifurcations leading to a singular wave state. *Phys. Rev. E*, 56(4):4157, 1997.

[96] A. H. Slocum. *Precision Machine Design.* Prentice-Hall, 1992.

[97] R. I. Stephens and H. O. Fuchs. *Metal fatigue in engineering.* J. Wiley, New York.

[98] S. H. Strogatz. *Nonlinear dynamics and chaos.* Perseus Books, Cambridge, MA, 1994.

[99] G. I. Taylor. Statistical theory of turbulence. In *Proceedings of the Royal Society of London A: Mathematical, Physical and Engineering Sciences*, volume 151, pages 421–444. The Royal Society, 1935.

[100] D. Terwagne. *Bouncing droplets, the role of deformations.* PhD thesis, Université de Liège., 2011.

[101] D. Terwagne, F. Ludewig, N. Vandewalle, and S. Dorbolo. The role of the droplet deformations in the bouncing droplet dynamics. *Physics of Fluids*, 25(12):122101, 2013.

[102] P. B. Umbanhowar. *Wave patterns in vibrated granular layers.* PhD thesis, University of Texas at Austin, Austin, TX, 1996.

[103] E. Villermaux. Fragmentation. *Annu. Rev. Fluid Mech.*, 39:419–446, 2007.

[104] J. Walker. Drops of liquid can be made to float on the liquid. What enables them to do so? *Scientific American*, 238-6:151–158, 1978.

[105] Ø. Wind-Willassen, J. Moláček, D. M. Harris, and J. W. M. Bush. Bouncing and walking drops: exotic and mixed modes. *Phys. Fluids*, 25:082002, 2013.

[106] G. H. Wortel, J. A. Dijksman, and M. van Hecke. Rheology of weakly vibrated granular media. *Phys. Rev. E*, 89(1):012202, 2014.

[107] J. C. Yang, W. Chien, M. King, and W. L. Grosshandler. A simple piezoelectric droplet generator. *Experiments in Fluids*, 23(5):445–447, 1997.

[108] P. Zeeman. On the influence of magnetism on the nature of the light emitted by a substance. *Philos. Mag.*, 43(262):226–239, 1897.